**NTNU – Trondheim**
Norwegian University of
Science and Technology

# Solar Simulation for the NTNU Test Satellite Solar Cells

## Martin Alexander Nygren

Master of Science in Cybernetics and Robotics
Submission date: March 2014
Supervisor: Jan Tommy Gravdahl, ITK

Norwegian University of Science and Technology
Department of Engineering Cybernetics

# Solar Simulation for the NTNU Test Satellite Solar Cells

Martin Nygren

11 March 2014

MASTER THESIS

Department of Engineering Cybernetics

Norwegian University of Science and Technology

Supervisor 1: Professor Jan Tommy Gravdahl

Supervisor 2: Roger Birkeland, NUTS Project Manager

# Preface

This Master's thesis has been written at NTNU as the final work of the study program of Engineering Cybernetics. The work was done over the course of autumn and winter 2013/14, as part of the NTNU Test Satellite (NUTS) group.

Trondheim, 2014-03-11

(signature)

Martin Nygren

# Acknowledgment

I would like to thank my supervisors, Jan Tommy Gravdahl and Roger Birkeland, for their contribution to my work and the opportunity to work with the NTNU Test Satellite, and a big thank you goes to Turid Worren Reenaas and Xiaodong Yang at the Department of Physics for providing their invaluable help with the solar simulator and the optical calibration lab.

Finally, I would like to express my gratitude towards my family, friends, and especially my girlfriend Inna, who all have given me wonderful support.

M.N.

# Abstract

The relevant energy theory behind intensity and spectral irradiance from the sun is discussed with regard to how it changes due to factors like Earth-Sun distance, solid angle of the sun disk and circumsolar region, angle of incidence and atmospheric mass. This translates to how the experienced conditions for solar cells vary, how and why solar simulation is done the way it is with such stringent requirements, as well as what can be expected in terms of difference between controlled, fixed conditions and operation in environments where we are not free to modify the variables as easily. The most essential theory of solar cell structure and performance is reviewed, with emphasis on the theory needed to understand the design principles, characteristics and behavior of the high-efficiency multijunction solar cells available for the NUTS project. The most commonly encountered components of a solar simulator is discussed to the point where the information provided should allow for a well-informed evaluation and selection of design for most applications, and be of guidance if one were to wish to attempt to create a device able to simulate aspects of the solar irradiation.

Solar cell characteristics are developed by the use of a solar simulator under controlled testing conditions to ensure reproducible results. The effect of controlled sunlight from a range of different angles onto a solar cell is investigated in terms of current-voltage characteristics, and in particular the effect on short circuit current as compared to what is expected of theory. It is found that the angle of incidence of light can be calculated from the measured current with a general accuracy of about $1°$, when compensating for reflectivity in the solar cell cover glass.

# Sammendrag

Denne rapporten tar for seg den relevante teorien bak intensitet og spektrum av sollys, med tanke på hvordan disse endrer seg i forhold til faktorer som avstanden mellom solen og Jorden, kjeglevinkel til solskiven med område rundt, innfallsvinkel og atmosfærisk masse. Dette kan oversettes til hvordan de erfarte forhold for solceller varierer, hvordan og hvorfor solsimulering blir gjort slik det gjøres, med slike strenge krav, så vel som hva som kan forventes i form av forskjeller mellom kontrollerte, faste omstendigheter, og operasjonell drift i omgivelser hvor man ikke står like fritt til å forandre på vilkårene. Den mest essensielle teorien bak solcellestruktur og -ytelse blir fremlagt, med fokus på teorien som trengs for å forstå designet, karakteristikkene og oppførselen til høyeffektivitetssolcellene som er tilgjengelige for NTNU Test Satellite (NUTS)-prosjektet. De oftest påmøtte komponentene i forbindelse med solsimulering blir diskutert til den grad hvor den oppgitte informasjonen tilretter for en velinformert evaluering og designvalg for de fleste bruksområder, og kan være til hjelp om en skulle ønske å lage et apparat som kan simulere gitte aspekt av sollyset.

Solcellekarakteristikker blir målt ved bruk av en solsimulator under kontrollerte testomgivelser for å forsikre reproduserbare resultater. Effekten av kontrollert sollys fra en rekke forskjellige vinkler mot en solcelle blir undersøkt i form av strøm-spenningskarakteristikker, med særlig fokus på effekten det har på kortslutningsstrøm i forhold til det som er forventet av teori. Det blir funnet at vinkelen av lysinnstråling kan beregnes med en generell nøyaktighet på rundt 1°, når man tar høyde for reflektivitet i solcellens dekselsglass.

# Contents

# List of Figures

# List of Tables

# Chapter 1

# Introduction

## 1.1   Background

### Problem Formulation

The work done throughout this thesis will be done with the author's previous work [1] in mind, parts of which were published and presented at the *2nd IAA Conference On University Satellite Missions And Cubesat Workshop* in Rome, 2013 [2]. The work is mainly concerned with determining a sun vector by combining hypothetical current measurements from mutually orthagonal, axially translated solar panels. The main concern of what still needs to be done is the physical testing of the solar cells, and comparison of results to that expected of theory. Due to the fact that the NUTS project have no access to the means needed for PV testing at the time of writing, a sufficient test setup have to be made, or access to proper testing facilities needs to be acquired.

### Assignment

1) Review the literature on solar cell technology and solar simulators.
2) By finding an adequate way to simulate controlled sunlight, establish and test how well the NTNU Test Satellite (NUTS) solar cells can be used to determine the angle of the sun for utilization as crude sun sensors in the satellite attitude determination and control subsystem (ADCS).

## 1.2 Limitations

Sunlight at space conditions is no trivial effect to recreate, it is to be expected that compromises will have to be made one way or the other. Testing of components in vacuum simultaneously is out of the question at this point. The cells that will be tested are slightly different cells than those that will be used in final version of the satellite, and are to be considered as "cells for testing". Any results are to be expected to be slightly different than for the future cells. The ADCS system will make use of simultaneous measurements from several solar cells, while the testing performed in this thesis will focus on the behavior of a single cell.

## 1.3 Approach

A thorough study will be performed of how actual sunlight can best be simulated, meaning a review of all factors involved; actual sunlight, solar cells and the components needed to recreate the conditions, as well as which critera must be met for results to be credible, and what differences one can expect by simulation compared to reality.

Depending on the resources at hand, a sufficient testing setup will be acquired or created, where the solar cell(s) will be exposed to artifical light under controlled circumstances to determine behavioral characteristics. The results from testing will be documented and compared to that which is dictated by theory, to further support or suggest reconsideration of the use of the solar cells as sun sensors.

## 1.4 Structure of the Report

- Chapter 2: Gives a brief contextual introduction to the NUTS project and the ADCS system.

- Chapter 3: Provides the necessary theory for energy calculations of light, and covers how intensity and spectral irradiance changes with respect to a number of factors.

- Chapter 4: Presents the relevant theory behind solar cell operation and performance.

- Chapter 5: Breaks down the structure of solar simulators to a component level, and gives the necessary conditions to classify and characterize the concept of solar simulation.

- Chapter 6: Documents the experiments performed on the solar cells by use of solar simulator under standard testing conditions.

- Chapter 7: Concludes the work done in this report, and gives advice for further work.

# Chapter 2

# Context

The content of this chapter is to be considered partly taken from the author's previous work during the specialization project [1].

## 2.1 NTNU Test Satellite (NUTS)

ANSAT is a student satellite project initiated by the Norwegian Centre for Space-related Education (NAROM), Norwegian Space Centre (NSC), and Andøya Rocket Range (ARR), following the previous Norwegian student satellite project nCube. ANSAT has entailed the construction and deployment of 3 CubeSat satellites over the period from 2007 to 2014. These projects are HiN-Cube, CUBEStar, and our project NUTS. Work on NUTS started in September 2010 and thus it is the most recent satellite to join ANSAT, however the work is a continuation of two previous installments of satellite design by NTNU. Despite the solid work performed, previous success have been limited; the first project disintegrated due to a second stage rocket failure at launch, and the status of the second satellite is formally unknown as no signals have been received post launch. The hope is to have NUTS ready for launch in 2015. The main design functionality of NUTS was originally to capture infrared images of gravity waves [3], process them and transmit the images back to ground station. However, due to cost and resources, it has been decided that the infrared camera payload could not be implemented for this satellite, and it will be attempted to carry a visual range camera as replacement.

NUTS adheres to CubeSat specifications [4], and will be built as a 2U CubeSat, or "two unit/-
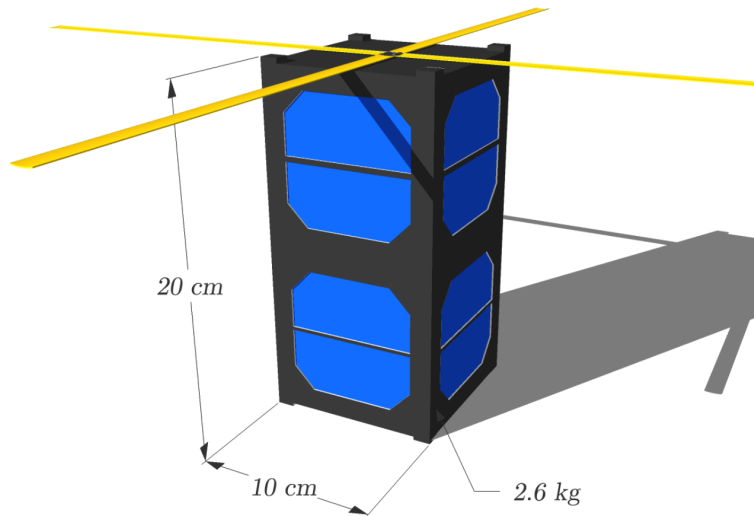
Figure 2.1: CAD model of the NUTS 2U CubeSat (illustration from [6]).

double CubeSat", where 1U is defined by the size 10 × 10 × 10 cm and a weight limit of 1.33 kg. A CAD model of the satellite can be seen in Figure 2.1. One thing that currently makes NUTS stand out from other CubeSats is the active research done towards utilizing a carbon fibre mesh for the structure [5], which if successfully done, will yield a lower structural weight while still providing the demanded structural rigidity and robustness.

### 2.1.1 NUTS ADCS and Previous Work

An attitude determination and control system (ADCS) is an integral component of any satellite which requires orientation control while in orbit. In order to be able to meaningfully alter the attitude towards a desired reference setpoint, knowledge about the current state is required. By use of estimation methods the experienced attitude can be *determined* within a degree of relative certainty, and any deviations from desired attitude can be compensated and *controlled* by the chosen response of the attitude control system with 3 degrees of freedom (DOF). The problem of attitude control in the case of satellites like NUTS is twofold, where a *detumbling* controller is needed to cancel the angular rate after orbital insertion, and *stabilization* control is needed to stabilize the attitude such that adequate pointing accuracy is achieved. Prior to the decision to forfeit the infrared camera payload, the attitude pointing accuracy requirements were established to be within 10 degrees of all axes, and is for the moment considered to be unchanged even though several different numbers are found throughout the literature attached to

the NUTS project.

**Sensors** : Gyroscopes and magnetometers are used to measure the angular velocity and the local magnetic field, respectively, while the solar panels will be used for crude sun sensing by calculating angles from the perceived solar intensity at mutually orthogonal solar panels to create a sun vector.

**Actuators** : NUTS will use magnetorquers; magnetic coils wrapped along the entirety of the 2-unit frame along all three axes. By applying controlled current through these magnetic coil actuators, interaction is done with the local magnetic field, resulting in a small but sufficient change in the rotation of the satellite around its center of gravity. As the magnetic field from the actuators will introduce disturbance bias in the magnetometer measurements, the thesis of Bråthen [7] demonstrates a design which switches between measurements and actuator drive.

The ADC systems for NUTS have been worked on since the first instances of satellite design at NTNU, and the design has undergone several iterations of changes and gradual improvements. Many of the physical properties associated with the magnetically actuated design of NUTS comes from the early thesis of Soglo (1994) [8], and Wisniewski (1996) [9] from Aalborg University which the NUTS project have an ongoing cooperation with. The work of Øverby (2004) [10, 11] show a review between the early approaches of angular velocity feedback control ("the Wisniewski controller"), attitude control based on magnetometer feedback and a proposed linear quadratic controller. The work of Svartveit (2003) [12, 13] and Ose (2004) [14] show detailed work on a discrete Kalman filter for use in the nCube project, which was subsequently modified into an extended Kalman filter in the work of Rohde (2007) [15]. For detumbling control, a dissipative controller has been explored and implemented previously, and more recently the concept of B-dot control has been investigated, which in the thesis of Tudor (2011) [16] show great results during the detumbling phase, also when exposed to measurement noise in the thesis of Bråthen (2013) [7].

The current estimation method selected for use in the NUTS CubeSat is based on the quaternion estimator (QUEST) [17] method, which was extended (EQUEST) in the thesis of Jenssen and Yabar (2011) [18, 19] to include non-vectorized gyroscope measurements and linear prediction terms for the attitude estimation, based on the work of Psiaki and Markley (2000) [20, 21]. The EQUEST have been found accurate and reliable when compared with the extended Kalman filter (EKF) and an Xsens reference motion tracking system. The thesis of Rinnan (2012) [22, 23] further developes the EQUEST to include attitude predictions and gyroscope information, and describes how the EQUEST algorithm can be used in conjunction with a nonlinear Grip observer to provide fast initial estimates, however there are some doubt as to how the increased complexity can efficiently be handled by a microcontroller. Evaluation of the attitude estimation techniques implemented on an Arduino microcontroller has been performed in the work of Holberg, (2012) [24, 25], which further improved the ADCS prototype by accomodating for three actuators and analog solar cell input. The thesis of Alvenes (2013) [6] shows the development of an extensive nonlinear Simulink model which was ported to microcontroller C-code, inspired by the simulator designs described in the thesises of Øverby (2004) [10, 11] and Tudor (2011) [16].

The relevant theory for integration of solar cell readings into the NUTS ADC subsystem is present in a large number of the works referred to in this section, including, but not limited to, the definitions of representative satellite coordinate frames and their transformations [16], construction of sun vector in the satellite body/orbit frame [1, 12], collection of analog solar cell data [24] and integration of sensor data into prototype ADCS microcontroller systems [6].

# Chapter 3

# Light Theory

## 3.1 Photometric Characteristics

When evaluating the characteristics of light, one should be aware that there in fact exists two parallel different systems of units for expressing the parameters related to radiance and spectral output [26].

- The *physical* photometric or *radiometric* system, which considers light as electromagnetic radiation, pure and simple, in terms of radiance (brightness) measured in watts, used in conjunction with units of distance and angle. This system encompasses the measurements of the entire electromagnetic spectrum.

- The *physiological* photometric system, which describes the properties of light as they are evaluated by a standardized human eye. The standardization is based upon the average human eye's sensitivity to different colors of light, with a maximal response to a wavelength of 550 nm. The system is based upon units of lumen, rather than watts. This system however fails to express radiation ranges outside the visible spectrum, such as UV and IR, and can as such not be properly used for evaluating many aspects that ties in with e.g. photovoltaics.

This work will primarily use radiometric quantities to describe radiation. It should be pointed out that *irradiance*; the amount of electromagnetic energy incident on a surface per unit time

10
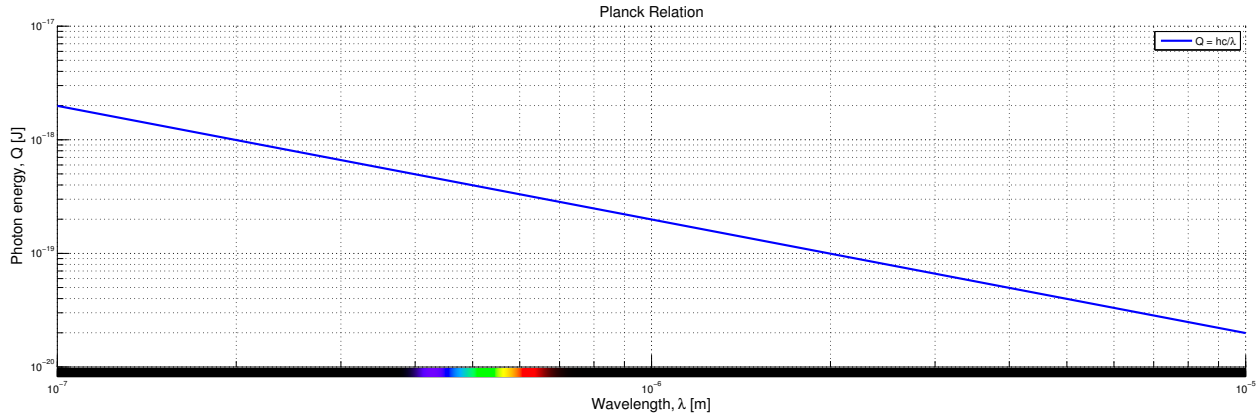
Figure 3.1: Planck relation illustrating energy of photons by wavelength.

per unit area, earlier referred to as *radiant flux density*, is used interchangeably with the term *intensity*.

## 3.2 Energy of Light

### 3.2.1 Photons

Optical power is a function of both the amount of photons as well as the wavelength, and each photon contains energy of which is described by the Planck relation

$$E_\lambda = h\nu = \frac{hc}{\lambda} \tag{3.1}$$

where $h$ is Planck's constant, $c$ is the speed of light, $\nu$ and $\lambda$ are the radiation frequency and wavelength, respectively, and the resulting $E_\lambda$ is the individual photon energy. As can be seen in Figure 3.1, shortwave ultraviolet (UV) light contains much more energy per photon compared to light with longer wavelengths such as visible or infrared (IR) radiation. The definitions of wavelength categories can be found in ISO 21348 [27], of which a subset is included in Table 3.1.

### 3.2.2 Blackbody Radiation

Spectral blackbody emissive power describes the amount of energy emitted by a blackbody radiatior with surface temperature $T$, per unit time, surface area and wavelength, and is described

Table 3.1: Definitions of solar radiation spectral categories [27]

| Spectral category | Spectral sub-category | Wavelength range [nm] | Referred to as |
|---|---|---|---|
| Ultraviolet | UV | $100 \leq \lambda < 400$ | Ultraviolet |
| | EUV | $10 \leq \lambda < 121$ | Exteme Ultraviolet |
| | FUV | $122 \leq \lambda < 200$ | Far Ultraviolet |
| | MUV | $200 \leq \lambda < 300$ | Middle Ultraviolet |
| | NUV | $300 \leq \lambda < 400$ | Near Ultraviolet |
| Visible | VIS | $380 \leq \lambda < 760$ | Optical |
| | | $360 \leq \lambda < 450$ | purple |
| | | $450 \leq \lambda < 500$ | blue |
| | | $500 \leq \lambda < 570$ | green |
| | | $570 \leq \lambda < 591$ | yellow |
| | | $591 \leq \lambda < 610$ | orange |
| | | $610 \leq \lambda < 760$ | red |
| Infrared | IR | $760 \leq \lambda < 1000000$ | Infrared |
| | NIR (IR-A) | $760 \leq \lambda < 1400$ | Near Infrared |
| | MIR (IR-B) | $1400 \leq \lambda < 3000$ | Middle Infrared |
| | FIR (IR-C) | $3000 \leq \lambda < 1000000$ | Far Infrared |

by Planck's distribution law for a surface in a vacuum or gas

$$E_{b\lambda}(T) = \frac{C_1}{\lambda^5 (e^{\frac{C_2}{\lambda T}} - 1)} \qquad [\text{W/m}^2 \cdot \text{nm}] \tag{3.2}$$

where

$$C_1 = 2\pi h c^2 = 3.74177 \times 10^{20} \text{ W} \cdot \text{nm}^4/\text{m}^2$$

$$C_2 = \frac{hc}{k_B} = 1.43878 \times 10^7 \text{ nm} \cdot \text{K}$$

The term *spectral* indicates wavelength dependency, and an illustration of the spectral black-body radiation for a range of temperatures can be seen in Figure 3.2, where also Wien's displacement law

$$\frac{\text{d}}{\text{d}\lambda}(E_{b\lambda}(T)) = 0 \qquad \Rightarrow \qquad (\lambda T)_{\text{max}} = 2.8978 \times 10^6 \text{ nm} \cdot \text{K} \tag{3.3}$$

is indicated, showing the relation between the blackbody temperature and the radiation
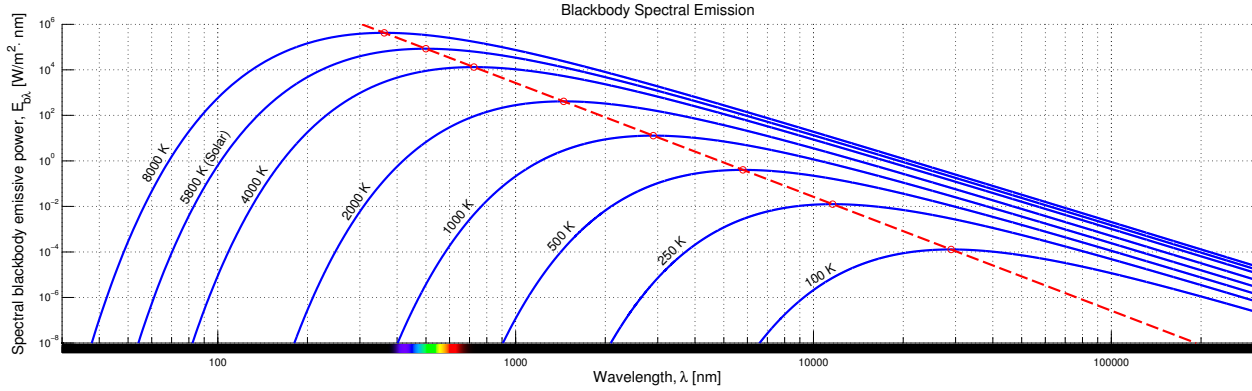
Figure 3.2: Spectral blackbody radiation visualized logarithmically for a range of surface temperatures, with Wien's displacement law indicated.

wavelength which contribute the most power in the spectrum. It can easily be seen that as the blackbody temperature gets higher, more of the energy distribution is shifted towards high-frequency radiation.

The total amount of radiation energy which is emitted by a blackbody radiator over all wavelengths per unit time and surface area is described by the Stefan-Boltzmann law, which is equivalent to integrating the spectral blackbody emissive power over the entire wavelength spectrum;

$$E_b(T) = \int_0^\infty E_{b\lambda}(T)\,\mathrm{d}\lambda = \sigma\,T^4 \qquad [\text{W/m}^2] \tag{3.4}$$

where $\sigma$ is Stefan-Boltzmann's constant, $T$ is the surface absolute temperature in kelvin, and the resulting $E_b$ is the (total) blackbody emissive power.

It should be noted that no known radiator has the exact same emissive power as a true blackbody/full radiator; the ratio between the output of a radiator and that of a blackbody at the same temperature and wavelength is known as the *spectral emissivity $\eta(\lambda)$* of what we refer to as a *selective radiator* when the emissivity is wavelength dependent.

## 3.3   Solar Radiation

### 3.3.1   The Solar Constant

The solar constant is the rate at which the solar energy density (irradiance) is received at the top of the Earth's atmosphere on a plane perpendicular to the angle of incidence, when Earth is at its mean distance away from the sun. The sun can for most purposes be considered a blackbody radiator with a surface temperature of $T_{\mathrm{sun}} = 5778$ K [28, 29] and radius $r_{\mathrm{sun}} = 6.963 \times 10^8$ m [30], which by use of Equation 3.4 means that the approximate emitted power density at the surface of the sun is

$$E_{\mathrm{sun}}(T) = \sigma T_{\mathrm{sun}}^4 = (5.67 \times 10^{-8})5778^4 = 6.32 \times 10^7 \text{ W/m}^2 \tag{3.5}$$

This approximation entails that the emission of radiation from the sun, as for all black body radiators, is considered isotropic. In addition, the fact that the Earth is a considerably long distance away from the sun means that only the photons which are emitted directly towards the Earth will contribute to the solar spectrum as observed from Earth. Thus, for most practical purposes, the solar irradiance upon the Earth can be considered as parallel streams of photons [31]. As the radiation travels through space, the intensity diminishes by the law of inverse squares as the emitted radiation is distributed over an ever increasing area. To approximate the solar constant, we see that by the time the solar radiation reaches Earth, it has spread out over a sphere of radius $d_{\mathrm{E}} = 1$ AU, or about the distance of the mean radius of Earth's orbit around the sun as can be seen in Figure 3.6, and have diminished to an approximate value of

$$E_{\mathrm{sc}} = \frac{4\pi r_{\mathrm{sun}}^2}{4\pi d_{\mathrm{E}}^2} E_{\mathrm{sun}} = \frac{4\pi (6.963 \times 10^8)^2}{4\pi (1.496 \times 10^{11})^2} (6.32 \times 10^7) = 1369 \text{ W/m}^2 \tag{3.6}$$

Mathematical calculation of the solar intensity at the top of Earth's atmosphere can give a good approximation, however the answer will not be perfect due to factors such as the sun not being a 100% perfect blackbody radiator, change in luminosity, variation in orbit radius, occurence of sun spots and cycles. The scientific community operates with a couple standardized values for the solar constant, gathered from satellite data. ASTM [32, 33] states a value of $1353 \pm 21$ W/m$^2$ with a reference value of 1366.1 W/m$^2$, while The World Metrological Organi-
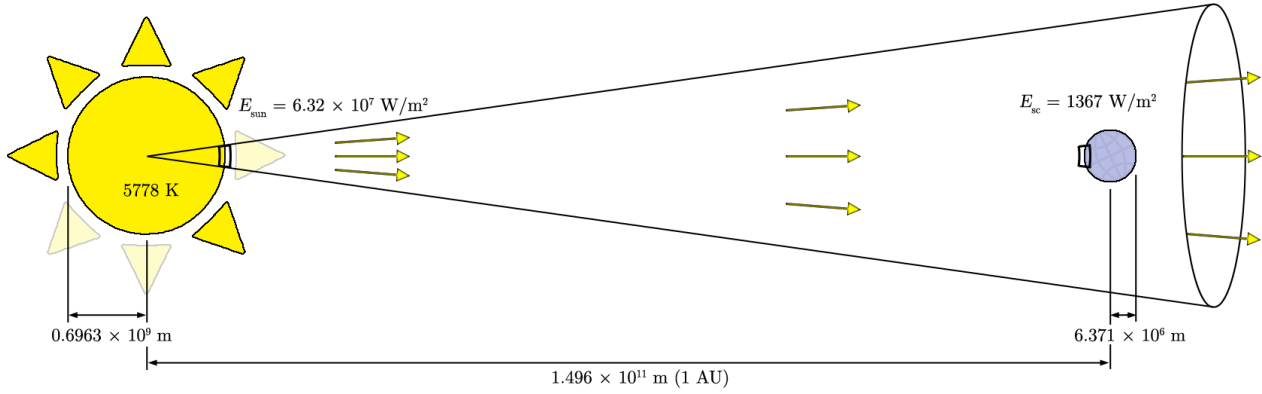
Figure 3.3: The solar radiation intensity at a distance of 1 AU is known as the solar constant and has an accepted value of 1367 W/m$^2$.

zation (WMO) adheres to a value of 1367 W/m$^2$. These values are however subject to change as new research is performed, such as the work of Kopp and Lean (2011) [34] which suggests that the value is closer to 1361 W/m$^2$.

### 3.3.2 Earth-Sun Relationship

The intensity of solar radiation energy that arrives at the outermost layers of the Earth atmosphere is termed the total solar irradiance (TSI) [27]. The Earth orbits around the sun in an elliptical fashion with the sun located in one of the ellipse focal points, meaning that the Earth-sun distance $d_E$ varies throughout the course of the year, as can be seen illustrated in Figure 3.4. And as the distance varies, the extraterrestrial TSI $E_E$ does as well, which can be expressed in terms of the solar constant

$$E_E(d_E) = \frac{4\pi r_{sun}^2}{4\pi d_E(t)^2} E_{sun} = \frac{a^2}{d_E(t)^2} E_{sc} \qquad (3.7)$$

where $d_E(t)$ is the Earth-sun distance as a function of time of year, and is suggested evaluated [35] in relation with the received solar radiation at the top of Earth's atmosphere as

$$E_E(t) = \left(1 + 0.033 \cos\left(\frac{2\pi(n-4)}{365}\right)\right) E_{sc} \qquad (3.8)$$

where n is the day of the calender year, with $n = 1$ being January 1$^{\text{st}}$. The relationship can be seen visualized in Figure 3.5. The Earth orbit eccentricity $e$ is not large however, and has a
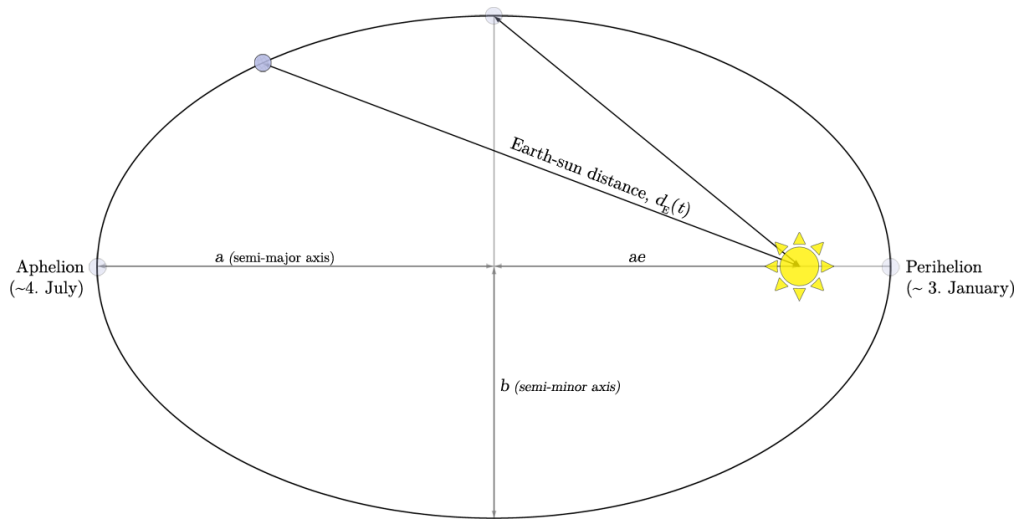
Figure 3.4: Solar intensity varies over the course of a year due to Earth's elliptical orbit. Note that the orbit eccentricity is greatly exaggerated for illustrative purposes.
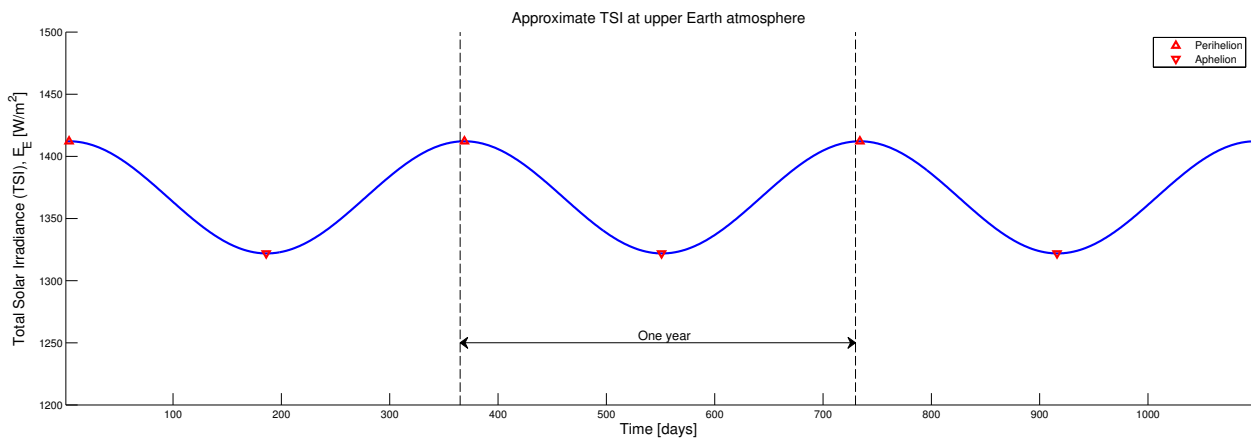


Figure 3.5: Total solar irradiance at top of Earth atmosphere as a function of time of year.

reported value of 0.0167 [36] which means that the orbit is in fact quite close to circular. Using Equation 3.7, we can investigate the approximate difference in solar intensity at the closest and furthest points from the sun during Earth's orbit, *perihelion/periapsis* and *aphelion/apoapsis* respectively.

$$E_E(\text{aphelion}) = E_E(a(1+e)) = \left(\frac{a}{a(1+e)}\right)^2 E_{sc} = \frac{E_{sc}}{(1+e)^2} \tag{3.9}$$

$$= \frac{1367}{(1+0.0167)^2} = 1322 \text{ W/m}^2$$

$$E_E(\text{perihelion}) = E_E(a(1-e)) = \left(\frac{a}{a(1-e)}\right)^2 E_{sc} = \frac{E_{sc}}{(1-e)^2} \tag{3.10}$$

$$= \frac{1367}{(1-0.0167)^2} = 1414 \text{ W/m}^2$$

Meaning that the difference between maximum and minimum intensity received throughout the year is roughly 7% with the current astronomical and orbital parameters. Note that this value is for the Earth's atmosphere in general, and not to be confused with total *insolation* which is the actual amount of solar radiation incident upon unit horizontal surface at a given, fixed locality over a specified time period. This value is dependent on the solar zenith angle, and thus will vary with latitude and time of day in addition to the time of year.

### 3.3.3 Air Mass

The air mass (AM) coefficient is a measure of the length of the optical path which sunlight have to traverse in order to reach the surface of the Earth, expressed relative to the path length of vertical inclination normal to the surface as can be seen in Figure 3.6. The coefficient is used to compensate for how absorption and scattering in the atmosphere influences the solar radiation spectral content and intensity before the radiation makes its way down to the Earth's surface, and the AM number is described accurately for angles of incidence up to around 75° by [37]

$$\text{AM} = \frac{1}{\cos\theta} \tag{3.11}$$

where $\theta$ is the solar angle of incidence, measured in offset from normal to the Earth's surface
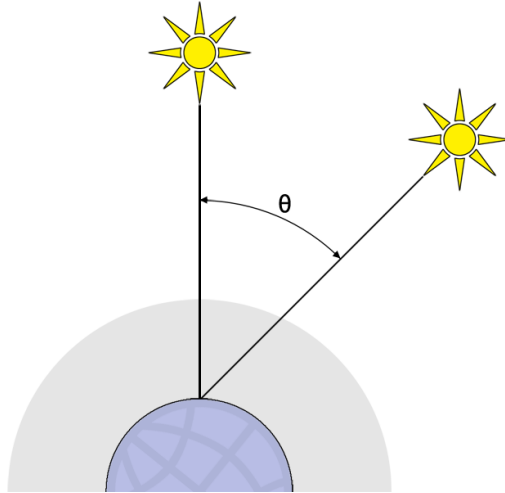
Figure 3.6: The amount of air mass (atmosphere) that the solar radiation has to pass through to reach the Earth's surface depends on incidence.

such that $\theta = 0$ gives AM1 .

AM0 represents the solar spectrum outside the Earth's atmosphere, as the radiation does not have to pass through any air mass at all. This is the irradiation conditions utilized for space applications, and the current standard spectrum is given by ASTM E-490 [32].

AM1.5, or an incidence angle of $\theta = 48.2°$ has become the testing and comparison standard for terrestrial photovoltaic applications. Furthermore, the spectral content of solar radiation at the Earth's surface has a diffuse component in addition to the direct, due to reflection and scattering in the atmosphere. AM1.5G represents the Global spectrum, which is designed for flat plate modules, and is made from both diffuse (scattered) and direct sunlight. AM1.5D stands for the Direct spectrum, and is defined for solar concentrator work. It includes the the direct beam from the sun plus the circumsolar component in a disk 2.5 degrees around the sun. The latest AM1.5 standards pertaining to photovoltaic applications are the ASTM G-173 [33] and IEC 60904-3 [38], derived from simulations utilizing the atmospheric modeling software SMARTS [39, 40] to generate the standard spectra, assuming a set of representative atmospheric parameters.

An overview of the standard solar radiation spectra used for photovoltaic applications can be seen in Table 3.2.

Table 3.2: Standard reporting conditions (SRC)

| Application field | Air mass | Spectral irradiance reference | Total irradiance [W/m$^2$] | Temperature [°C] |
|---|---|---|---|---|
| Low Earth orbit (LEO) | AM0 | ASTM E-490 [32] | 1366.1 | 28 |
| Terrestrial global | AM1.5G | ASTM G-173 [33] | 1000.4 | 25 |
| Terrestrial direct+circumsolar | AM1.5D | ASTM G-173 [33] | 900.1 | 25 |
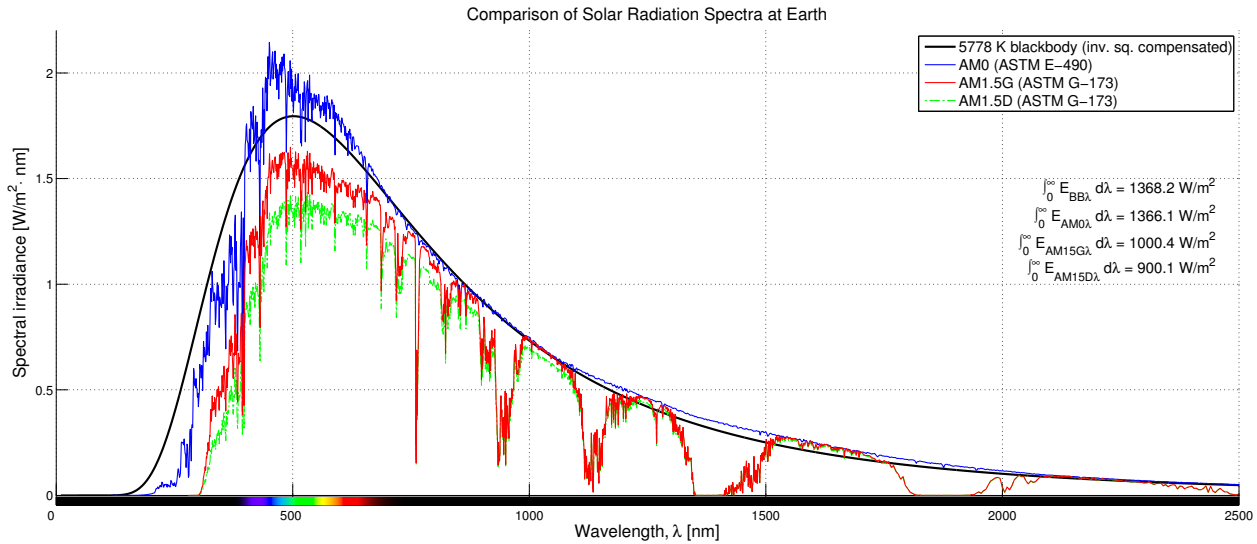


Figure 3.7: The different standardized solar radiation spectra for Earth.

### 3.3.4  Solar Spectrum

The solar spectrum is the distribution of solar radiation as a function of wavelength, and it is made up of a continuous emission with a range of emission line structures superimposed onto it. The different solar spectrum standards as received at Earth can be seen in Figure 3.7 compared to that of a blackbody radiation source with the surface temperature of 5778 K. As demonstrated earlier in Figure 3.2 and by Equation 3.3, the peak of the solar radiation occurs around $\frac{2.8978 \times 10^6}{5780} \approx 500$ nm, which is located approximately in the middle of the visible band. In the infrared and visible region, the solar radiation matches closely to that of a blackbody with a surface temperature of 5778 K. However, the solar radiation deviates quite a bit from that of a equivalent blackbody temperature of the sun in the ultraviolet spectrum, and actually appears closer to a temperature of 4500 K. The mismatch is a consequence of the emission from the nonisothermal solar atmosphere [41].

Solar radiation entering the Earth's atmosphere is scattered and absorbed by clouds, atmo-

spheric gases, aerosols and the Earth's surface. Some of the absorbed radiation is re-emitted in the far infrared as heat, while part of the scattered radiation continues on its path through the atmospheric system where it is subject to further scattering and absorption, yet some still make it all the way down to the surface. As can be seen by studying the solar radiation spectra, the atmosphere attenuates certain bands of the spectral distribution more heavily than others. Rayleigh scattering hinders much of the radiation in the UV and visible bands. The ultraviolet radiation from 300 to 450 nm is mainly absorbed by $O_3$, and with further increasing wavelength there can be found a narrow-band absorption at around 760 nm due to $O_2$, and relatively broader $H_2O$ absorption bands at 900-1000 nm, 1100-1150 nm, 1300-1450nm and 1800-1950 nm, respectively [42]. For detailed studies of the absorption spectra of the Earth atmosphere, one can utilize the Spectral Calculator of GATS, Inc. [43], which implements the LINEPAK [44] system of calculating absorption spectra from the HITRAN2008 [45] spectroscopic database and allows for online graph generation and downloading of structured data sets.

At Earth, the radiation coming directly from the sun without being subject to significant absorption and scattering is called *direct* solar radiation, while the amount of scattered radiation inbound from all other directions is referred to as *diffuse* solar radiation. This effectively distinguishes the difference between the AM1.5G/D spectrums mentioned in the previous section about air mass, where AM1.5G (*global*) is the sum of the direct and diffuse components of solar radiation received on a horizontal plane. It is also referred to as *hemispherical* due to the fact that it accounts for all the scattered radiation, in contrast to the direct which only takes into account a the small solid angle of the sky which the sun spans.

### 3.3.5 Sunshape

The sun, as perceived from an observer at Earth spans an angular diameter of

$$\delta_{\text{sun}} = 2\tan^{-1}\left(\frac{r_{\text{sun}}}{d_{\text{E}}}\right) = 9.31 \times 10^{-3} \text{ rad} \tag{3.12}$$

or about 0.533° in the sky at the mean Earth orbit distance from the sun. This translates to a solid angle of

$$\Omega_{\text{sun}} = 2\pi(1 - \cos\left(\frac{\delta_{\text{sun}}}{2}\right)) = 6.81 \times 10^{-5} \text{ sr} \tag{3.13}$$

from the equation of the area of a spherical cap on a unit sphere. This method may well be a good approximation for the *solar disk* as perceived from space, however it does not take into account the scattering that takes place due to the Earth atmosphere which results in the formation of radiation which appears to originate from the region around the sun, known as the *circumsolar region*, or *aureole*. Together, the brightness distribution of the solar disk and the circumsolar region is known as the *sunshape* [46].

The circumsolar ratio (CSR) is defined as the ratio of the irradiance within the circumsolar region $E_{\text{cs}}$, over the irradiance from both the solar disk $E_{\text{disk}}$ and circumsolar region [47], meaning

$$\text{CSR} = \frac{E_{\text{cs}}}{E_{\text{disk}} + E_{\text{cs}}} \tag{3.14}$$

where the irradiance can be obtained by integrating the radial distribution of solar and circumsolar radiation $B(r)$ under the assumption that the disk and its circumsolar region are symmetrically circular

$$E_{\text{disk}} = \int_{sun} B(r) r \, dr \qquad [\text{W/m}^2] \tag{3.15}$$

$$E_{\text{cs}} = \int_{cs} B(r) r \, dr \qquad [\text{W/m}^2] \tag{3.16}$$

where $r$ is the angular distance from the center of the solar disk. Note that $r$ can also be replaced by $\theta$, where $\theta$ is the subtended angle measured from the center of the sun. The intensity distribution for a range of CSR can can be seen in Figure 3.8 from the works of Buie (2004) [47], where the size of the solar disc region can be seen in form of the intensity graphs which drop significantly in magnitude when the angular displacement from the perceived center of the disc exceeds that of the sun radius as seen from Earth, at around 4.65 mrad.

A detailed review of the history and methods used regarding sunshape and circumsolar brightness can be seen in the thesis of Kalapatapu (2012) [49], and a recent state of the art review
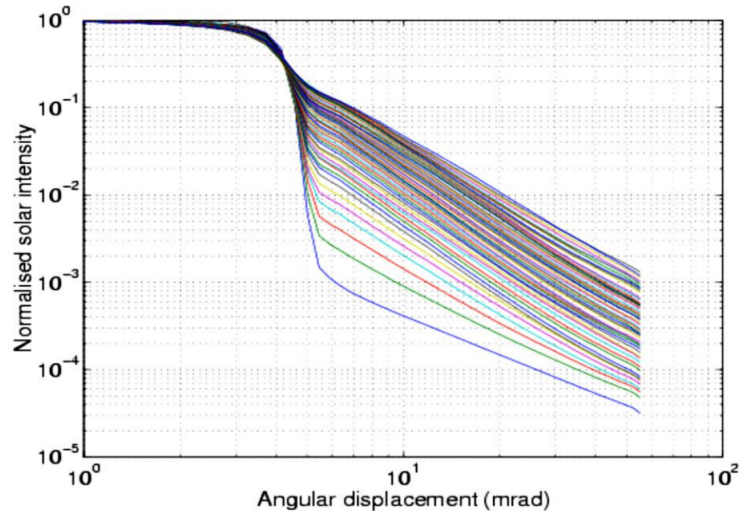
Figure 3.8: Filtered solar profiles from the Lawrence Berkeley Laboratories RDB [48], showing CSR from 0.01 to 0.8 (from [47]).

can be found in the work of Wilbert et al. (2012) [50].

### 3.3.6 Lambert's Cosine Law

To illustrate the concept, consider the flat surface $A_1$ parallel to the Earth's surface, outside the atmosphere of the Earth as pictured in Figure 3.9. When this surface is normal to the sun, the experienced solar irradiance will be that of $E_E$, defined previously. However, when the surface normal forms an angle $\theta$ greater than zero with the direction of the incoming sunlight, the solar irradiance upon the surface drops with that of

$$E_{\text{surface}} = E_E \cos\theta \tag{3.17}$$

From the illustration we can see that the rate of solar radiation falling on both surface $A_1$ and its projected surface normal to the solar radiation $A_2$ is identical, assuming parallel sun-rays. Surface $A_1$ does however span a greater area than its projected counterpart, meaning that the solar irradiance striking surface $A_1$ is less than that of surface $A_2$. The greater the angle of incidence, the more the unit area of beam is spread out over the surface, effectively reducing the intensity [51].
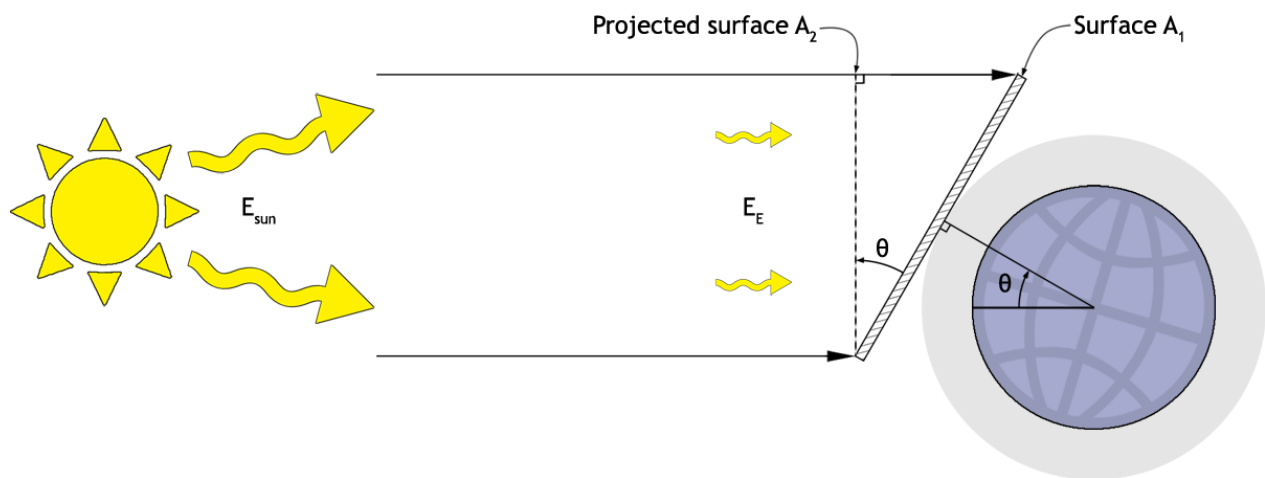
Figure 3.9: Loss of intensity by the cosine effect upon a surface parallel to the ground, at an angle of incidence $\theta$ of incoming solar irradiation.

# Chapter 4

# Solar Cell Theory

This chapter features relevant theory from a few main books which provide excellent in-depth coverage to the subject, and should be considered as the sources unless otherwise expressed: *Practical Handbook of Photovoltaics* (2012) [52], *Handbook of Photovoltaic Science and Engineering* (2011) [31], *Third Generation Photovoltaics* (2003) [53].

## 4.1 Photovoltaics

Photovoltaics is the technology that generates DC electrical power from semiconductors when they are exposed to light. The fuel source is free and virtually infinite, there is no emissions or by-product from use, and the design is modular and has no moving parts. Solar cells have been the main source of energy on space crafts ever since the first solar powered satellites were launched in 1958; Sputnik 3 and Vanguard 1.

### 4.1.1 Semiconductors

Semiconductors typically possess electrical resistance characteristics that are somewhere between what is seen in true conductor and insulator materials. Their behavior is described by means of the electronic band structure theory for solids, where electrons in a crystalline solid occupy energy levels in nearly continuous energy bands which are determined by the properties of the material. An important material property is the *band gap*, which is determined by the energy levels of two specific high-level energy bands; the *valence band* and the *conduction band*.

Table 4.1: Periodic table subsection with elements frequently used for PV semiconductors [31]

| I | II | III | IV | V | VI |
|---|----|-----|----|---|-----|
|   |    | B   | C  | N | O   |
|   |    | Al  | Si | P | S   |
| Cu | Zn | Ga | Ge | As | Se |
| Ag | Cd | In | Sn | Sb | Te |

Conductor materials have valence and conduction bands that overlap eachother, which facilitates the transition of electrons from the valence band to the conduction band, leaving *holes* of a net positive charge in the valence band. Electrons from adjacent atoms have no trouble passing through the crystal structure into the holes, propagating the local net positive charge in the opposite direction. On the other hand, insulator materials have no net positive charges in the valence band, and very large bandgaps which means that it requires a large energy input for valence electrons to be able to enter the conduction band.

In semiconductors, the band gaps are relatively small, but still finite and generally very different from one material to the other. Most practical electronic applications for semiconductors are designed such that a certain voltage potential is required in order to create current flow between the bands, like the behavior commonly found in diodes and transistors. The conduction characteristics of semiconductors can be altered by means of *doping,* which is the process of introducing small amounts of impurities to the material, which alters the crystalline structure in the form of populating it with additional holes or electrons to upset the levels of bonding. A *p-type* semiconductor is created by introducing an element which creates holes due to insufficient valence electrons, like when adding a Group III element (see Table 4.1) into pure silicon which is Group IV and by default has a complete valence band with it's four valence electrons shared between adjacent atoms. Similarly, *n-type* semiconductors can be created by doping with a material which will leave a net result of excess electrons in the material.

### 4.1.2 Photovoltaic Cell

Solar cells, the individual PV units, are typically made from semiconductors where the bandgap energy is a unique parameter for each semiconductor material. The energy required to raise the electron from the valence band to the conduction band can be supplied by the photons

which make up sunlight, which are dependent on wavelength as given by the Planck relation in Equation 3.1. In order to be a good absorber of solar energy, the bandgap should cover energy levels produced by the majority of the solar radiation as given by the spectrum shown in Figure 3.7. On Earth, this translates to a bandgap of about 1-2 eV. When the cell is exposed to sunlight of energy higher than the band gap, or photons of short enough wavelength in other words, the photons are absorbed and electrons in the valence band is transferred to the conductance band. The conduction-band electrons are collected by a specially made selective contact, and made available as current to drive an external circuit. The potential created by exciting an electron is directly tied to the bandgap of the semiconductor and independent of the energy of the absorbed photon as long as it's higher than the bandgap energy, meaning that the excess energy from a high-energy photon is lost, at least in a simple single-junction solar cell. Upon traversing the external circuit and making it back to the solar cell, the electrons are returned to the valence band through a second contact, ready to be excited by another photon.

So a basic solar cell is for the most part a semiconductor diode which have been designed to absorb and convert sunlight to electricity in a (somewhat) efficient manner. The diode is created by bringing together a n-type and a p-type semiconductor to form a metallurgical pn-junction, consisting of two quasi-neutral regions on either side of a depletion region. Typically, the more heavily doped quasi-neutral region is called the emitter and the more lightly doped region is called the base, or the absorption region. The front contact of the diode is formed by a metallic grid which allows the sunlight to fall onto the surface of an antireflective layer between the gridlines, while the back contact is formed by a metallic layer on the backside of the solar cell.

## 4.2 Variations of Solar Cells

### 4.2.1 Conventional

As we've established, solar cells can be constructed from a range of semiconductor materials, but the far most commonly used material is silicon (Si), in versions of mono/singlecrystalline, poly/multicrystalline and amorphous (non-crystalline). Solar cells are however also made from

other materials, such as GaAs, GaInP, and Cu(InGa)Se$_2$. Most of the modules on the market to-day consist of crystalline silicon, and the choice of silicon has been common due to its fairly well matched characteristics toward the solar spectrum, as well as the well-developed silicon fabrication technology from the large electronics industry. Additionally, the material is abundant, nontoxic and stable even without encapsulation.

However, silicon has certain limitations in form of being mechanically brittle, and relatively weak absorbation of sunlight which means that relatively thick cells are needed. When the cell thickness is increased, it means that some of the excited electrons have to traverse a lot of the material before being extracted by the cell contact, which increases the risk of the electron returning to the valence band in what is known as *recombination loss*. This loss can be reduced by the use of materials with extremely good purity and structure. These can be made from hyperpure silicon, also referred to as *polysilicon* or *semiconductor grade* (SG) silicon, consisting of many random grains of crystalline silicon. Polysilicon is melted and recrystallized, to be used either for growing monocrystalline silicon ingots by the use of the Czochralski (Cz) technique [54], or by casting multicrystalline silicon blocks in a less expensive process. Regardless of the method used, the resulting blocks are cut into wafers with a thickness of typically 150–250 μm. Monocrystalline silicon wafers produce cell efficiencies of about 16–17%, while the multicrystalline silicon wafers produce cells of about 13–15% efficiency. Wafering does however result in material loss due to the cutting, and up to 40% of the material can end up as dust. To combat this expensive loss, silicon sheets are sometimes grown as *ribbons*, however with less cell efficiency and longer growth time.

### 4.2.2 Thin film

Thin film solar cells (TFSC) are sometimes referred to as "second generation" cells, and the modules are mainly categorized into amorphous silicon, CdTe and CI(G)S modules, depending on the photovoltaic material used. They were originally developed mainly in order to achieve lower cost and improved large scale production conditions than could be envisioned for modules based on silicon wafers.

Thin film cells are based on materials which strongly absorb sunlight, such that they can be designed with an extremely thin thickness, in the scale of several micrometers, making the

cells so fragile that they must be deposited onto a substrate for mechanical support. However, the thin material reduces the risk of recombination losses greatly, and eases up the stringent requirements for material purity and crystallinity of the material, which is one of the main expenses associated with production of high quality silicon wafers. One of the other advantages of thin films over silicon cells is the manufacturability; whereas silicon modules are created by assembling cells made from wafers into modules, thin film cells can be formed into a module at the same time as the cells are being made. The process is designed in such a way that it facilitates automation, and a process known as monolithic integration to separate and interconnect the cells on a large substrate. The efficiency of thin film modules is however usually 25–50% lower than for silicon modules, which counters the low production cost per area with a higher cost per energy produced.

### 4.2.3   Third Generation Solar Cells

The Shockley-Queisser limit [55] sets the thermodynamic efficiency limit of a single-junction solar cell to about 31% under certain hypotheses that were thought to be fundamental and absolute, by examining the amount of electrical energy that is extracted per photon of incoming sunlight. It should be noted that the limit applies to each of the individual cells in a multijunction stack configuration, but it does not apply to the stack as a whole. In fact, the theoretical limit of an infinite-layered junction stack exposed to concentrated sunlight has been shown to be 86% [56].

Solar cells which are based on principles that break with some of the Shockley-Queisser hypotheses are referred to as *third-generation* [53] or *next-generation* [57] solar cells. The most studied third-generation solar cells are [31]:

- The intermediate band solar cell [58], which refutes the Shockley-Queisser hypothesis that photons below the bandgap are not absorbed.

- The multi exciton generation solar cell [59], which refutes the Shockley-Queisser hypothesis that the absorption of a photon can excite only one electron from the valence band.

- The hot carrier solar cell [60], which refutes the Shockley-Queisser thermalization hypothesis that the electrons are at the lattice temperature.

Other technologies are also sometimes referred to as being third-generation, such as new thin-film technologies like the solid–liquid junction dye-sensitized solar cells (DSSC) [61] and polymer-based organic solar cells [62] that are based upon completely different principles than that of regular solid-state solar cells.

### 4.2.4 Multijunction Cells

For both CSP and space applications there are needs for solar cells with efficiencies as high as possible, and the efficiency limitations of conventional single-junction cells is a nontrivial obstacle. The idea behind multijunction cells is to overcome these limitations by allowing several solar cells with different bandgaps to convert photons of different energies, reducing the loss of energy due to photon energies which are either too high or too low to be efficiently converted by a single-junction cell. The simplest configuration which allows this achievement is to simply stack the cells on top of eachother such that the topmost cell has the highest bandgap, and lets photons with less energy than the bandgap pass through to cells with progressively lower bandgaps, as illustrated in Figure 4.1 The more spectral regions allowed, the higher overall effiency can be achieved, and a study of the conversion efficiency limits with respect to the number of bandgaps was performed by Henry [63]. Low-energy pass filters should be located between cell, such that the reflection threshold of each filter is the bandgap of the cell directly above. It has been shown [64] that a setup without backside reflectors will lead to lower efficiencies when the number of cells is finite. In a configuration like this, every cell will have an individual load circuit, and thus a different voltage bias. The most favorable designs feature all the junctions fabricated monolithically on a single substrate, such as the multijunction solar cell schematic depicted in Figure 4.2.

Group III-V semiconductors possess several characteristics which make them particularly suitable for solar cells; many of these materials are available with high absorption coefficients due to direct bandgaps in the range of interest for converting solar radiation. Especially important examples are GaAs which features a bandgap of 1.42 eV, and Ga0.5In0.5P which has a bandgap of about 1.85 eV. The high efficiencies and radiation tolerance, as well as the lower temperature gradients of Group III-V solar cells have underlined their usefulness as replacements for traditional silicon solar cells in many space applications.
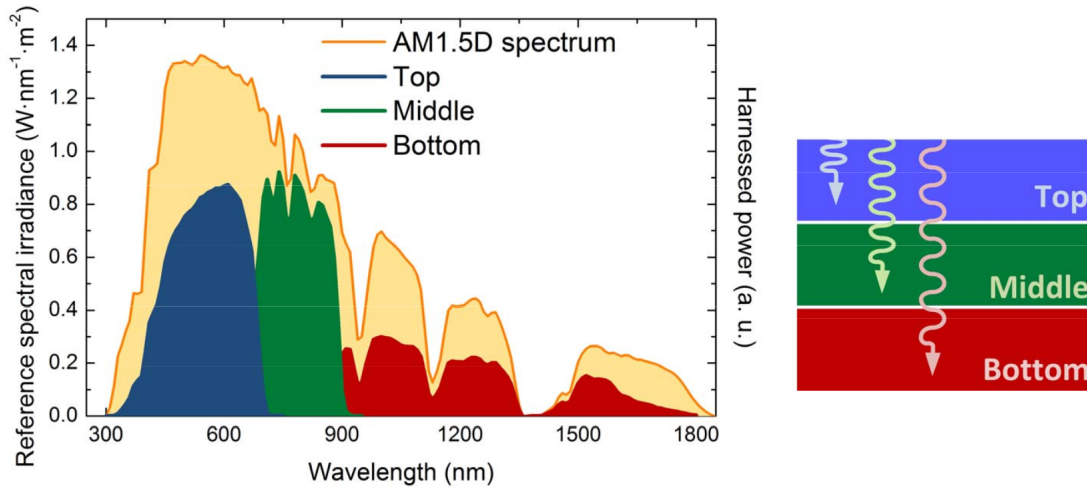
Figure 4.1: Subcells with different bandgaps in a monolithic triple junction solar cell (Illustration from [65]).
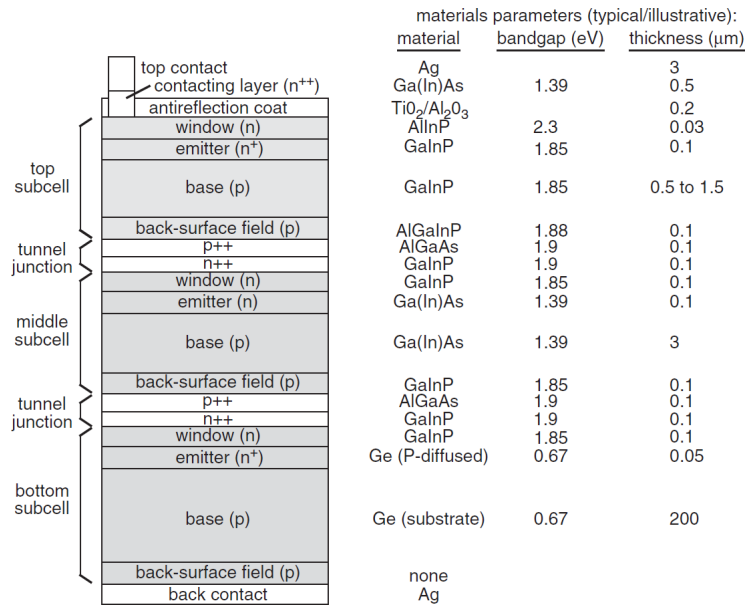


Figure 4.2: Schematic cross-section of a monolithic two-terminal series-connected three-junction solar cell. Typical materials, bandgaps, and layer thicknesses for the realization of this device structure as a GaInP/GaAs/Ge cell are indicated. The figure is not to scale. (Illustration from [31]).
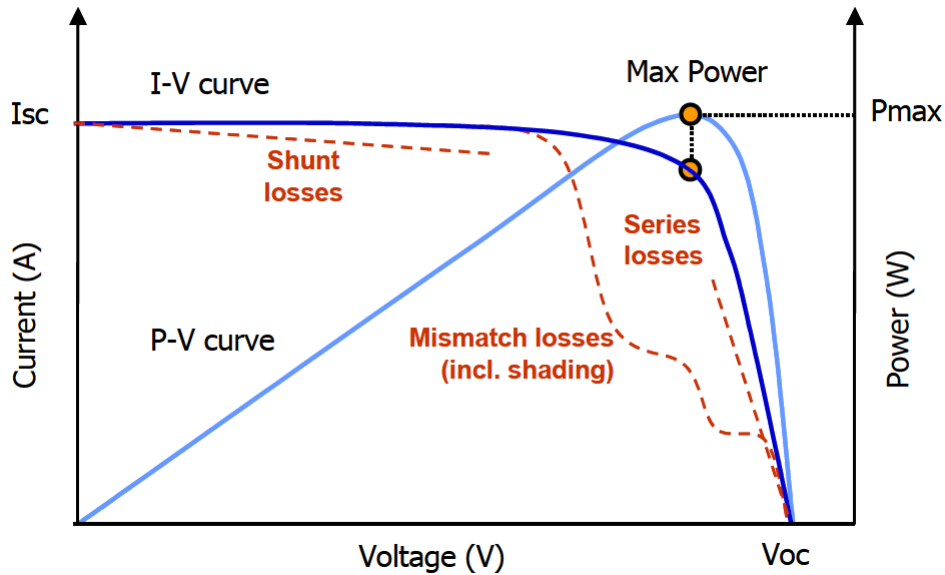
Figure 4.3: Typical I-V and P-V curves for a photovoltaic device, with loss illustration. [66]

## 4.3 Solar Cell Characteristics

### I-V Curves

The I-V (current-voltage) curve describes the energy conversion capability of a photovoltaic element, at a certain irradiance and temperature level. Each point of the curve represents the pair of current and voltage levels for a corresponding external load connected to the circuit, given that the intensity and temperature is kept constant.

### Important Characteristics

As we can see in Figure 4.3, the I-V curve illustrates several parameters which are used to characterize the behavior and efficiency of a solar cell, and when measured under STC they can be defined as follows:

*Open circuit voltage, $V_{oc}$* [V]: This is the voltage which develops over the cell when the terminals of the cell are isolated, by means of infinite load resistance or zero net current. At this point, all the generated electrical charge recombines internally instead of flowing out through the load. Reducing the operating temperature of the solar cell will increase $V_{oc}$ because at lower

temperatures the internally generated dark current is reduced; typically the dark current scales exponentially with temperature [67].

*Short circuit current, $I_{sc}$* [A]: The current which is drawn when the terminals of the cell are connected, making the voltage across the cell equal to zero. This is the largest current that can be drawn from the solar cell under the conditions used to produce the curve. The short circuit current is dependent on several factors, such as the spectrum of the indicent light and the number of photons.

*Maximum power point, $P_{max}$* [W]: This is the power that the cell would deliver to a perfectly matched load, or the point along the I-V characteristics curve which yield the highest electrical power, which is usually located in the knee bend of a normal I-V curve. For practical applications this means that we wish to adjust the input or load of a cell if we wish to produce the maximum amount of DC power output from the cell, as is done by the inverter unit in many PV systems.

$$P_{max} = I_{mp}V_{mp} \tag{4.1}$$

*Voltage at maximum power point, $V_{mp}$* [V]: The voltage along the I-V curve of the cell which along with $I_{mp}$ produce the maximum obtainable power. At lower voltages, the output flow of solar generated electrical charge is quite independent of the voltage. As the voltage approaches $V_{mp}$ and increases further, more and more of the charges recombine still within the solar cell instead of travelling out through the load.

*Current at maximum power point, $I_{mp}$ [A]:* The current along the I-V curve of the cell which along with $V_{mp}$ produce the maximum obtainable power.

*Characteristic resistance, $R_{CH}$* [Ω]: The output resistance at the maximum power point of a solar cell. When the load resistance is equal to $R_{CH}$, the solar cell is operating at the maximum power point. This is defined as [68]:

$$R_{CH} = \frac{V_{mp}}{I_{mp}} \tag{4.2}$$

*Fill factor, FF:* This is a measure of how much the I-V characteristics of an actual solar cell differ from that of an ideal cell, and is thus an important performance indicator. Graphically, it represents "squareness", or "rectangularity" of the I-V curve. The fill factor is defined as

$$FF = \frac{I_{mp}V_{mp}}{I_{sc}V_{oc}} = \frac{P_{max}}{I_{sc}V_{oc}} \tag{4.3}$$

In other words, the fill factor is the ratio between the maximum power and the product of the short circuit current and open circuit voltage. An ideal solar cell would have a fill factor of 1, meaning that the maximum power point is the same as the open circuit voltage and short circuit current. However in reality losses from shunt and series resistance degrades the rectangular shape of the I-V curve, and thus reduce the obtainable power and efficiency.

*Energy conversion efficiency, $\eta$:* This is defined as the ratio between the energy coming *out* and the energy going *in* to the cell, which for the maximum power output is

$$\eta = \frac{P_{max}}{P_{in}} = \frac{P_{max}}{EA} \tag{4.4}$$

where E is the irradiance (W/m$^2$) and A is the area (m$^2$) of the device.

*External collection efficiency, $\eta_C^{\text{ext}}$:* This is the ratio of the actual short circuit current compared to that of which would result if every single photon with energy higher than the band gap created electron-hole pairs that were collected, and is defined [31] as

$$\eta_C^{\text{ext}} = \frac{I_{sc}}{I_{inc}} \tag{4.5}$$

where
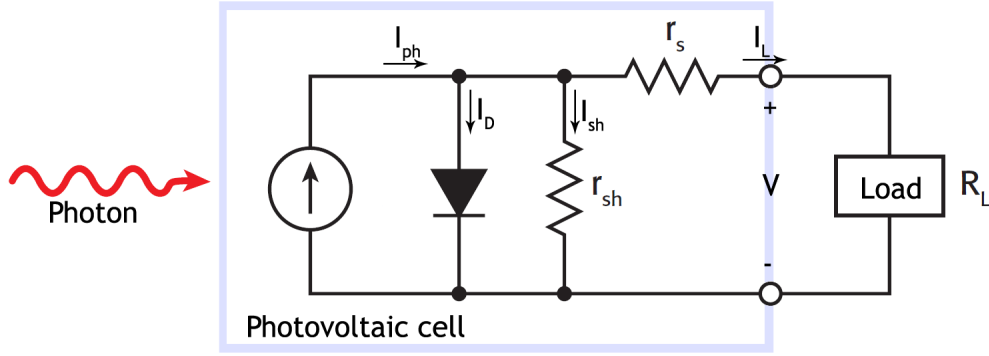
Figure 4.4: Equivalent circuit of a solar cell (adapted from [69]).

$$I_{inc} = qA \int_{\lambda < \lambda_G} f(\lambda) \, d\lambda \tag{4.6}$$

*External spectral response, $SR_{\text{ext}}(\lambda)$:* This shows the short-circuit current $I_{sc}(\lambda)$ resulting from a single wavelength contribution of light, normalized by the maximum current possible. The external spectral response is defined [31] as

$$SR_{\text{ext}} = \frac{I_{sc}}{qAf(\lambda)} \tag{4.7}$$

## 4.4 The Solar Cell Equivalent Circuit

The inner workings of an (idealized) solar cell may be represented by the equivalent circuit model as can be seen in Figure 4.4. The components which make up this model is

- $I_{ph}$, a light induced current source, which produces current due to optical generation. The magnitude of the current is mainly governed by parameters of irradiance, cell temperature, material and area.

- $I_D$, a dark saturation current generated by a pn junction diode; $I_D = I_S(e^{\frac{q(V+R_S I_L)}{nk_B T}} - 1)$. The diode current is determined by voltage across the cell, cell temperature and material.

- $r_s$, a series resistance, which ideally should be 0 $\Omega$, as it is responsible for reducing the cell's maximum power output, $P_{max}$, as well as the cell's behavior close to the short-circuit

current, $I_{sc}$. The series resistance is due to resistance of the metal contacts, ohmic losses in the cell front surface, impurity concentrations, and junction depth.

- $r_{sh}$, a shunt resistance parallel to the diode, which ideally should be of infinite magnitude. The shunt resistance represents loss due to crystal defects or surface leakage along the edge of the cell. A low shunt resistance causes power loss in a solar cell by enabling an alternative path for the photogenerated current, which in turn reduces the current flowing through the solar cell junction and thus reduces the voltage of the cell. Shunt resistance effects are most prominent at (1) low light levels, as the photogenerated current is low, and (2) at low voltages, where the impact of a resistance in parallel is high.

Additionally, an external load resistance, $R_L$, can be connected to the solar cell to close the circuit.

The short-circuit current and dark saturation currents are in reality given by minority-carrier properties and rather complex expressions that depend on the solar cell structure, material properties, and the operating conditions, however much can be illustrated by examining the basic form of the relations. E.g. for simplicity have the dark current due to depletion region (modeled as a second, parallel, diode) been ignored, which is a reasonable and common assumption for a good solar cell [31]. When the solar cell is illuminated, the current over the load becomes

$$
\begin{aligned}
I_L &= I_{ph} - I_D - I_{sh} \\
I_L &= I_{ph} - I_S(e^{\frac{q(V+R_sI_L)}{nk_BT}} - 1) - \frac{V + R_sI_L}{R_{sh}}
\end{aligned}
\tag{4.8}
$$

where $q$ is the electron charge, $k_B$ is Boltzmann's constant, $T$ is the junction temperature and $n$ is the diode ideality factor. For a given load resistance $R_L$, the cell develops a voltage $V$ with magnitude between 0 and $V_{oc}$, as determined by the I-V curve.

### 4.4.1 Effects of Parasitic Resistances

Resistive effects in the solar cell reduce the efficiency and potential power output, by dissipating power internally. These are modeled as series resistance $r_s$ and shunt resistance $r_{sh}$ in Figure 4.4.

## Open Circuit Voltage

As can be seen by Equation 4.8, the shunt resistance $R_{sh}$ reduces the open circuit voltage. For a high quality solar cell with negligible parasitic losses due to series and shunt resistances, $R_s = 0$ and $R_{sh} = \infty$; Equation 4.8 reduces to $V_{oc}(I_L = 0) = \frac{k_B T}{q} \ln(\frac{I_{ph}}{I_s})$, meaning that $V_{oc}$ slowly increases logarithmically with increasing photogenerated current as long as the dark current stays constant during operation at a given temperature. The open circuit voltage of III-V multijunction solar cells decreases with increasing temperature, however to a lesser extent than what is found in silicon devices [70, 71].

## Short Circuit Current

Similarly as for $V_{oc}$, if considering $R_s = 0$ and $R_{sh} = \infty$, we see that Equation 4.8 reduces to $I_{sc} = I_L(V = 0) = I_{ph}$, suggesting that short circuit current increases linearly with photogenerated current in an ideal scenario with no parasitic losses.

Due to the high quality of present III-V multijunction devices, linearity of the short-circuit current with the irradiance level is typically assumed [72]. Combined with the fact that open-circuit voltage increases logarithmically with photocurrent, and hence with light intensity, this in turn means that the efficiency fundamentally grows with irradiance. However, this trend is limited by the rise of series-resistance losses, which grow with the square of the current ($I^2 R$ factor). Fortunately, because the spectral response split into different junctions, the overall current density of multijunction cells is much lower than in single-junction devices, so the ohmic losses are highly reduced [65].

### 4.4.2   Effects of Temperature

When measuring solar cell characteristics, the area exposed to solar simulator illumination will experience a change in temperature from the surroundings.

$V_{oc}$ of a crystalline solar cell can be said to be approximately linearly dependent of the junction temperature of the material, and the same is true for most semiconductor photovoltaic

devices [37], and can be calculated by knowing the material characteristics of the cell. However, a more practical method is to have access to known temperature coefficients for the cell in question, which is thermally coupled to the thermally regulated work plane of the solar simulator. When exposed to a specific irradiance, the temperature of the junction will still increase faster than the temperature of the work plane, but by measuring the $V_{oc}$, the temperature of the cell can be estimated.

# Chapter 5

# Solar Simulators

The main advantages of performing PV power measurements with solar simulators over those of natural sunlight are quite obvious:

- No influence from dynamic weather conditions

- High reproducability of measurements due to controlled testing environment

On the other hand, solar simulation done under artificial conditions suffer due to the imperfections of light sources and the dissimilarity from natural sunlight, leading to a number of sources of error [73]:

- Inaccurate spectral irradiance distribution

- Fluctuation in irradiance

- Distribution of irradiance not uniform

This chapter will discuss the key elements to most solar simulation systems; their functions and characteristics, as well as how to evaluate the performance of solar simulators.

## 5.1   The Components of a Solar Simulator

A solar simulator can in its simplest form be defined to be made up from three major components; a light source with associated power supply, an optical train to modify the output beam

to meet certain performance requirements, and the necessary controls to operate and adjust behavior of the simulator. This section will aim to discuss some of the most frequently encountered components in greater detail.

### 5.1.1 Illumination Sources

When it comes to selecting light sources to be used in solar simulation, there is a number of important factors which can be evaluated for best possible results [74, 75, 76]:

- Lamp power, which is the primary indicator of the relative factor of intensity. Within the same type of source, generally a higher wattage will provide higher levels of intensity. One should however be aware that if the attained irradiance is higher than desired, compensating by reducing the input power below the nominal value can introduce distortions in the light characteristics.

- Power supply / ballast, which is responsible for providing the lamp with required voltage and amps. Depending on the lamp design, the requirements can vary wildly in both price and complexity.

- Source size / arc length, which describes how big the light emitting part of the lamp is. This is of special interest when considering reflectors to focus the output of a lamp, e.g. as a parabolic reflector is based on the concept of a point-sized source in the focal point to provide a parallel output.

- Intensity distribution curve, which illustrates the directional output of the lamp. The shape of this curve is governed by the internal structure and the housing of the lamp. Optical components such as reflectors and refractors should be designed with this graph in mind.

- (Correlated) color temperature, which is the radiation output as compared to that of an ideal black body radiator surface. This value tells us the relative distribution of spectral content, from low temperature (IR-heavy) to high temperature (UV-heavy).

- Color rendering index (CGI), which reveals how well the illumination of the light source compares to a reference source. Together with the color temperature, it gives a numerical estimate of which reference best approximates the light, and what the difference is.

- Spectral distribution, which is the electromagnetic content irradiating from the source. It displays how much of the radiation which is part of specific wavelength intervals, and can reveal characteristic narrow-band emission lines.

- Luminance, which is one of the commonly listed parameters for describing a lamp's characteristics. Unfortunately, these values are of limited use, considering that the parameter in fact only describes the amount of visible light output from the source, whereas for solar simulator applications one needs to take into account the extended spectrum containing UV and IR radiation as well.

Illumination sources based on plasma discharge (arc lamps) or incandescence (tungsten halogen lamps) require a considerable period after ignition to reach thermal equilibrium, a factor that can affect temporal, spatial, and spectral stability. All lamps that produce a significant level of heat, including light-emitting diodes, also exhibit a dependence of emission output on the source temperature [74]. It should also be noted that more irradiance is not necessarily better, lower power lamps have certain advantages [26]. Lower power lamps generally have smaller radiating areas, be it arcs or filaments, which means they perform closer to that of a point source. These are usually just as bright as their larger counterparts. Additionally, smaller lamps both require and emit less power, making them more friendly to handle in both aspects with regard to power supply and protection.

An example of utilizing a combination of several different types of illumination sources for creating a suitable spectrum for the silicon bandgap (300-1100 nm) can be found in the work of Guvench (2004) [77].

**Xenon Arc Lamps**

**Construction:** In contrast to incandescent lamps which are thermal radiators, a xenon arc lamp is a high intensity discharge (HID) lamp, where light is generated by driving electricity through highly pressurized, ionized xenon gas, forming a voltaic arc between two electrodes.

An example of a xenon arc lamp can be seen in Figure 5.1. The thick clear glass part of the lamp is usually a fused quartz envelope which is impermeable to most high temperature/pressured gasses, have a low thermal expansion coefficient, can withstand high pressure, and have optical properties which allows for high efficiency transmission of most light. UV light which passes through the envelope can cause a problem by ionizing oxygen in the air around the lamp, which subsequently may recombine into ozone. This is why certain lamps have their envelope doped or coated with UV blockant, and these lamps are labeled as being "Ozone Free", which is a nice alternative if one does not need output below 260 nm. On the subject of glass, this highly pressurized and relatively fragile environment does render the bulb vulnerable to explode if not treated carefully. This makes the xenon arc lamp a potentially volatile selection for an array setup when higher intensities are needed, as glass fragments may shoot out and start a chain explosion of bulbs. More often than not it is wiser to make use of the fact that the lamps are available in high power single bulb configurations, which can be coupled with a single ellipsoidal mirror, resulting in a tightly controlled spot size suitable for both solar simulation and concentrating solar photovoltaics (CSP) [78]. The anode and cathode are usually made from pure tungsten, and specially treated (thoriated) to withstand the operation of the lamp and enhance the electron emission of the electrode. The arc region between the anode and the cathode is very small; the vast majority of light is generated within a microscopic cloud of plasma (often referred to as "hot spot", or "plasma ball") where the electron stream leaves the cathode, and can for most purposes be considered as a point source. The high power xenon arc lamps and their associated drive electronics are generally expensive products, with nearly 10 times the cost-per-watt of that of commodity light sources [79]. Certain models can cost up in the range of tens of thousands NOK.

**Power supply:** Xenon lamps and HID lamps in general require a DC power supply with variable current and fixed voltage without fluctuations or overlaying AC ripple for best operation, as excessive ripple can lead to an unsteady lamp arc and flickering, which results in poor temporal stability. Additionally, an external ballast/igniter is needed to jump start the flame arc inside the lamp. This is done by overlaying the DC voltage with a high-frequency pulse in the range of 35-60 kV in order to jump the electrode gap and create the light arc. Once the arc is sustained
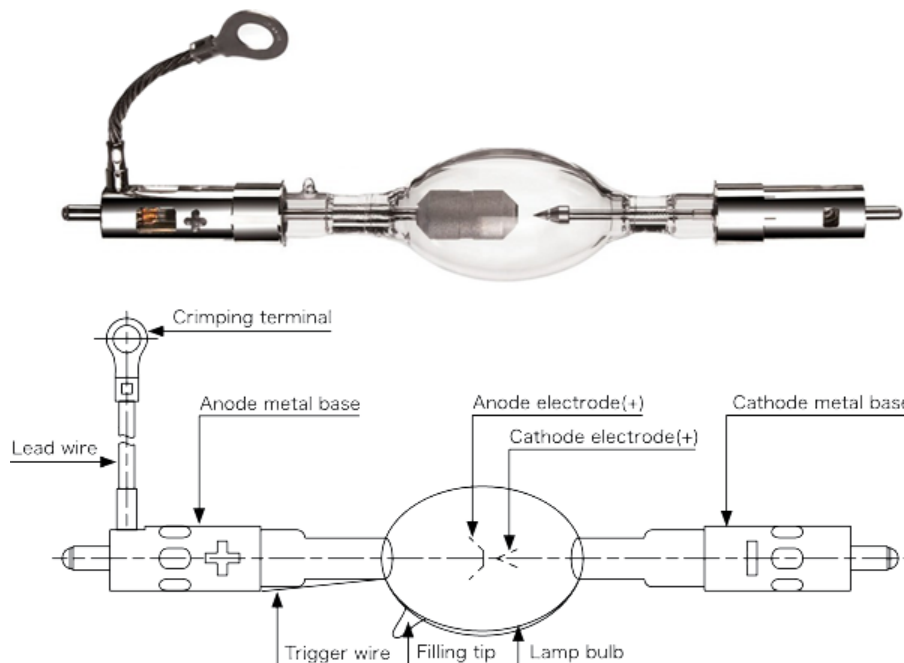
Figure 5.1: Xenon short arc lamp example: Philips XDC-6500B (illustrations from [80, 81]).

and the lamp is active, the ignition voltage is cut and normal lamp operation commences. The xenon lamp output also remains linear as a function of applied current, while the spectral radiance remains unaltered, and it can as such be modulated for specialized applications.

**Stability:** Arc discharge lamps are by comparison not the most stable of illumination sources, due to the inherent volatility of the voltaic arc; where the phenomenons of arc wander/flare due to cathode erosion (changes in emission point) and arc flutter (rapid displacement of arc column) can lead to momentary fluctuations in lamp brightness. The light output can in addition be affected by ambient electromagnetic fields or an insufficiently stable power supply. HID spectral output is also dependent on the gas pressure inside the bulb, which is why it is important to allow the bulb enough time to reach normal operating conditions. Arc lamps used for solar simulation generally have a life span of about 200-400 hours.

**Spectrum:** This is the most commonly found type of lamp used in solar simulators, with filters installed to approximate the desired light spectrum. These lamps generally exhibit an unfiltered emission spectrum that matches the solar spectrum closely, and feature good stability in the color characteristics of the small arc which intensely radiates like a 5500-6000 K blackbody. This

makes them a sound choice as illumination sources for high-quality simulation of sunlight. The xenon lamp spectrum does however diverge from any solar spectra, mainly because of the intense line output in the wavelength region of 800-1100 nm, where the strong Xe emission lines dominate the spectrum. Generally, excess radiation is also present below the region of 500 nm. Whereas filters can be used to reduce the mismatch, no reasonably priced filter have the ability of removing the superimposed Xe emission line output without also significantly altering the remainder of the spectrum.

**Metal Halide Lamps**

**Construction:** Like xenon arc lamps, metal halide (MH) lamps is a form of high intensity discharge lamp and thus also contain gases as significant pressure. The gas content is however different, and can consist of a mixture of a number of different gases which together decide the color temperature of the output emission spectrum. A metal halide lamp is mainly made up from an arc tube along with corresponding electrodes, an outer bulb, and a connection base. An example of a MH lamp can be seen in Figure 5.2. The commonly found outer glass bulb is in place to protect the inner components and reduce the heat dissipation loss, but can also be doped to reduce UV radiation like the ozone free xenon arc lamp envelope variety. This outer jacket also contributes to the MH lamps being considered a safer alternative, as it can help prevent hot pieces of debris from shooting out in the event of an explosive bulb failure [82].

**Power supply:** Whereas xenon arc lamps are started by overlaying the driving current with a pulse of high voltage from the ballast, the arc in MH lamps are usually struck by use of a third, starting electrode. Infrared–reflective coating is often applied on the exterior of the top and bottom parts of the arc tube, in order to reflect heat back onto the electrodes to keep them emitting properly.

**Spectrum:** Metal halide lamps are efficient light sources close to an ideal point source, which are strong in both UV and visible output, but the spectrum is dominated by strong spectral emission lines, much like mercury lamps except it produces a stronger output in the regions between the spectral lines. The spectrum can be varied by the use of different combinations of
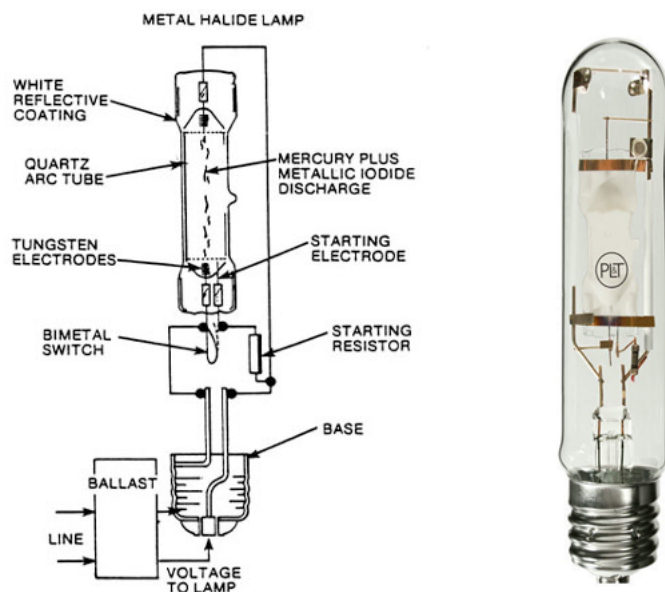
Figure 5.2: Metal halide lamp example: Precision Lighting 991327 (illustrations from [83, 84]).

metals in the arc tube, but the unfiltered emission spectrum does not match the spectrum of sunlight as closely as xenon arc lamps.  The typical lamp color temperature is around 4200 K, and yields less IR energy than what is found in halogen lamps. However there are variants up to 20000 K.

**Quartz Tungsten Halogen Lamps**

**Construction:**   The lamp consists of few components; a tungsten filament connected to external connectors via a foil sealed in place by pinched glass.  As with the arc lamps, the lamp glass envelope containing the fill gas of choice is usually made from fused silica quartz glass for it's thermal and pressure-withstanding properties.  The halogen gas in tungsten halogen lamps helps to re-deposit evaporated tungsten back on the hot filament instead of darkening the envelope, in a cycle known as the halogen regenerative cycle. Tungsten lamps are relatively inexpensive and easy to replace compared to many other light sources. Examples of QTH lightbulbs can be seen in Figure 5.3. The tungsten filament geometry is the main factor governing the photometric properties and light emission characteristics of the lamp. The length and thickness of the filament is decisive when it comes to operating voltage and power level, respectively, where high voltage require long filaments, and high power requires thick filaments. The effective size of the illumination source is determined by the filament field (height and width) when it is at
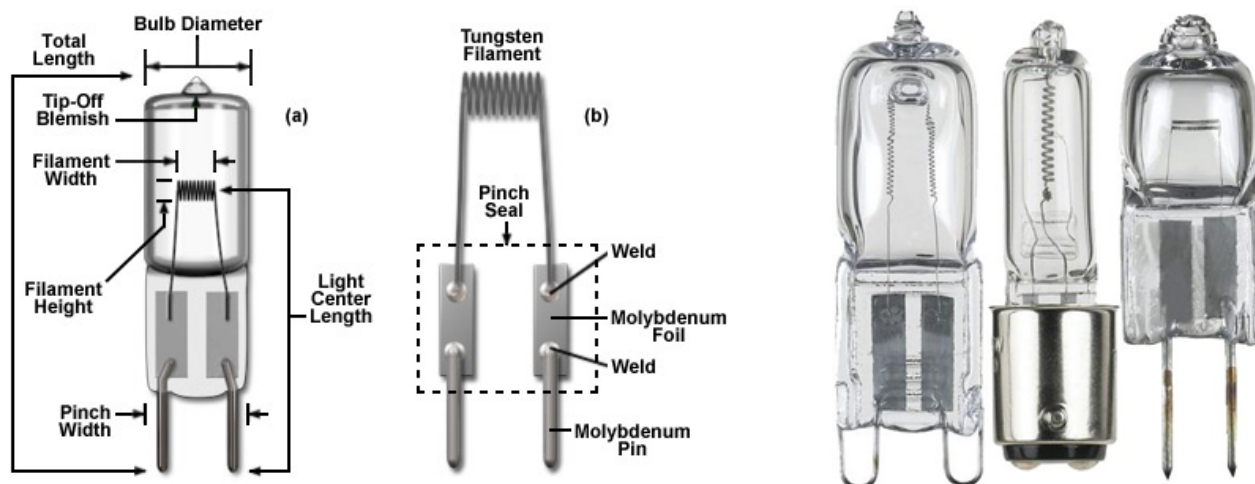
Figure 5.3: Quartz tungsten halogen lamp examples (illustrations from [85, 86]).

operational temperature.

**Power supply:**   The lamps are usually powered by DC a power supply, and it is recommended to utilize specialized circuitry for stabilizing current and suppressing ripple, such as found in what is called a "soft start" circuit.  The power supply converts the line current into an adjustable voltage which can be adjusted with a potentiometer to control the filament temperature, and in turn the spectral properties and intensity of the lamp.

**Stability:**   These lamps are considered popular visible and near-infrared (NIR) sources due to their smooth spectral curve and stable output. They are considered particularly stable, and are under normal operating conditions subject to only minor levels of temporal and spatial output fluctuation.  When a power regulated tungsten halogen lamp has reached operating temperature, it can stay extremely stable over long time periods due to the high thermal inertia of the filament.

**Spectrum:**   Tungsten halogen lamps are incandescent lamps which operate as thermal radiators, meaning that light is generated by the heating of the filament to high operating temperatures, where higher temperatures result in brighter light emitted. Their spectral emission closely resembles that of a blackbody radiator, however the brightest QTH lamps are operating at color temperatures around 3200-3400 K due to the melting point of tungsten, a color temperature

which is significantly less than that of the solar emission spectrum. This results in far less intensity overall, and energy shifted towards bands of longer wavelength than the solar spectrum. However, due to the smooth low-temperature blackbody-like emission output, unlike what the arc lamps exhibit, their spectra does not feature sharp spectral emission peaks, nor do they emit much high frequency UV radiation. On the other hand, they do emit excessively much IR energy due to the color temperature limited by the tungsten melting point, which does not allow the majority of output radiation to shift into the visible spectral region. By utilizing filters, it is possible to modify the QTH spectrum for a decent matching of sections of the solar spectrum. A filtered lamp can make a good match to the IR solar spectrum, and a reasonable yet inefficient match to the VIS, but is unsuitable for the high frequency regions of shortwave VIS and UV due to the low output.

**Light Emitting Diodes**

**Construction:** A light-emitting diode (LED) is an optoelectronic device which generates light via electroluminescence. It contains a p–n junction, through which an electric current is sent. In the heterojunction, the current generates electrons and holes, which release their energy portions as photons when they recombine [87]. The basic structure of a typical LED consists of the semiconductor material (the die or chip), a frame on which the die is mounted, and the encapsulation material surrounding the assembly. In most cases, the LED semiconductor is supported in a reflector cup that is attached to the cathode, while the top face of the chip is connected with a gold bonding wire to the anode [74]. Semiconductor LED chips comes in sizes ranging from about 0.3 mm$^2$ up to several mm$^2$, dimensions similar to the HID arc and tungsten halogen filament, respectively, and are found in a wide variety of physical shapes, radiation pattern and wavelength profiles. Examples of light emitting diodes can be seen in Figure 5.4.

**Power supply:** The optical output of a typical LED is approximately proportional to the drive current of the device. The drive current through an LED must be controlled. High current densities within the junction of the chip cause partial overheating which damages the crystalline structure of the LED die [90]. LEDs photon output occurs over a narrow spectral range so that LEDs operate at much lower temperatures. Thus, LEDs require less electrical power to produce
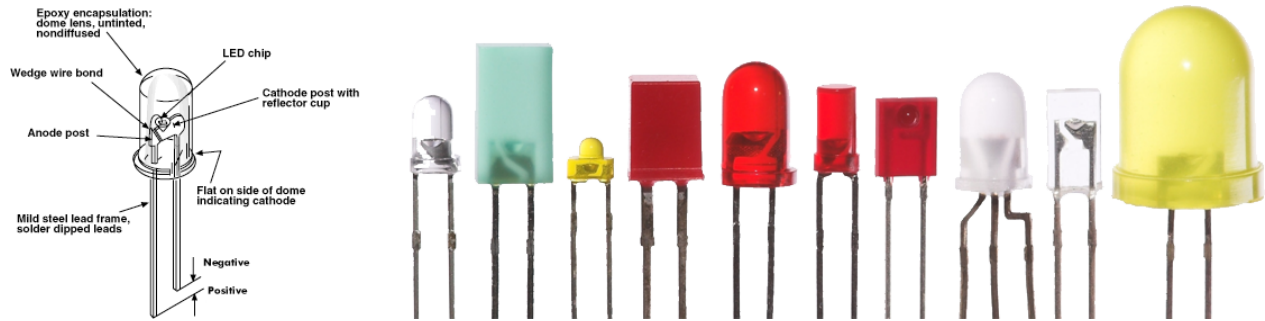
Figure 5.4: Light emitting diode examples (illustrations from [88, 89]).

the same optical output, and they can be more compact and bonded directly to a metal heat sink cooled by a fan. LED-based sources still require an efficient heat sink because operating above room temperature reduces their lifetime and results in a loss of optical output efficiency [74].

**Stability:** Due to their different nature compared to arc lamps and filament lamps, LEDs are among the best in terms of temporal and spatial stability. Provided that they are operated at reasonable conditions, they can expect a significantly longer lifetime than other lamps, where some manufacturers guarantee an individual lifetime of 100000 hours before seeing a loss of 30 percent of the intensity. When operating LEDs, a change in current can produce a shift of the emission peak. This effect often occurs if the LED die is not perfectly homogeneous, and the size of the shift often depends on the characteristics of the device semiconductor crystal. Wavelength stability can be ensured when using LEDs by calibrating the spectral output with operating current prior to initiating experiments [74]. LEDs have other advantages over traditional solar simulator light sources as well, in the fact that they can be modulated, switched on and off rapidly without the need for shutters or extensive periods to stabilize and provide full intensity.

**Spectrum:** Diodes emit light corresponding to the semiconductor used in manufacturing the chip. Silicon results in NIR light, while diodes made from other semiconductors can produce emission in the near-UV or VIS bands. Most commonly used are mixtures of periodic table group III and V elements, each of which mixture emit in a different quasi-monochromatic waveband, with spectral bandwidth typically in the ranges of 12-40 nm, yet can be as high as 140 nm
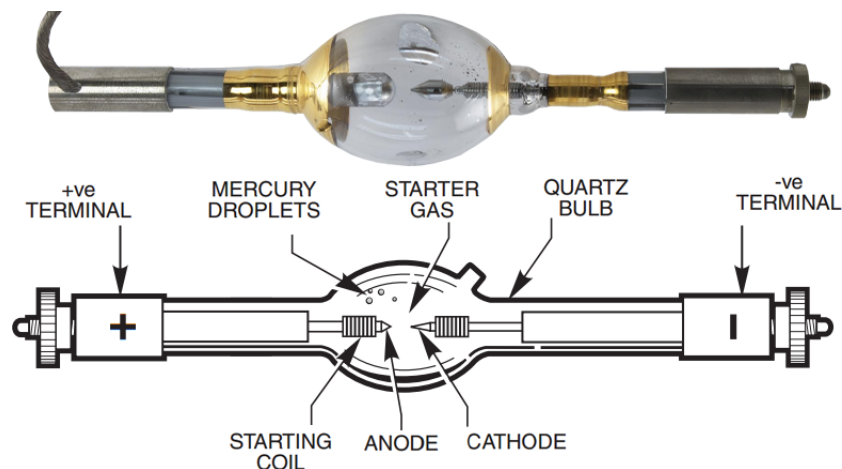
Figure 5.5: Mercury arc lamp example (illustrations from [92, 93]).

in some instances [87]. Combining several chips made from different semiconductors in different proportions with eachother can generate different color temperatures of white light. A uniform distribution is possible to make by having enough LEDs packed closely together, and beam shaping is very flexible due to the individual positioning of directed light sources. However, even if a quasicontinuous spectrum can be assembled, the main challenge lies in generating high enough intensity for the light to be suitable for simulation of sunlight, which traditionally have been unsuccessful due to the limitations of the LED technology. Recent advancements are however promising, and we have started to see the first actual high-rating LED simulators come around [91].

**Mercury Lamps**

**Construction:** Mercury arc lamps contains inert gas like xenon or argon, as well as a very specific amount of metallic mercury. When the bulb is at room temperature, it is possible to see the droplets of mercury on the inside walls of the bulb. When the lamp is ignited, the bulb starts building pressure up towards 75 atm, and the mercury droplets vaporizes. It is important that the bulb is operated in a vertical position with the anode at the bottom for the mercury to properly vaporize. Other than this, it shares a lot of common features with other arc lamps. The mercury lamps does however generally have a slightly larger arc spot than similar sized xenon arc lamps [26]. An example of mercury arc lamps can be seen in Figure 5.5.

**Power supply:**   Much like other arc lamps as discussed, the mercury lamps require a DC supply with current ripple stabilization, as well as an high-voltage starting pulse for ionizing the arc gap and forming the voltaic arc. It's also important to note that operating a mercury lamp at angles greater than 30° from vertical alignment will deflect the voltaic arc against the envelope which will result in uneaven heating and deteriation of the lamp.

**Stability:**   The bright mercury lamps provide very high irradiance levels, and are considered highly reliable despite their toxic content under high pressure. Compared to traditional incandescent lamps, they do have drawbacks in the form of stringent mechanical alignment, as well as what can be expected in terms of HID lamps, with temporal and spatial stability issues related to the violent nature of the arc, power supply requirements, high cost and safety hazards.

**Spectrum:**   Compared to incandescent lamps such as the tungsten halogen lamps, the mercury lamps provide 1000-10000% more brightness. It does however provide a lot of excess energy in the ultraviolet spectrum, as well as a range of prominent superimposed spectral emission lines which can be as much as 100 times brighter than the continuous emission between the lines. Much of the energy in the UV and visible spectrum is actually concentrated in these discrete lines, and the relatively continuous spectral emission region around 600-1000 nm is no brighter in output than that of the xenon arc lamp which feature considerably less emission lines overall. The lamp can however provide intense illumination over parts of the visible region with the use of filters [74].

### 5.1.2   Reflectors

As most illumination sources distribute their radiation outwards over a range of directions, it is useful to utilize reflectors in order to collect the lamp output into a usable, concentrated beam, which either focuses or collimates the radiation emitted by the light source. Designs of collection reflectors vary wildly in form of geometry and features, and range from simple concave mirrors to complex geometries such as parabolic, elliptical or (a)spherical which can organize and direct the radiation more effectively.

Reflectors can be made from a range of materials, where the most usual includes glass and
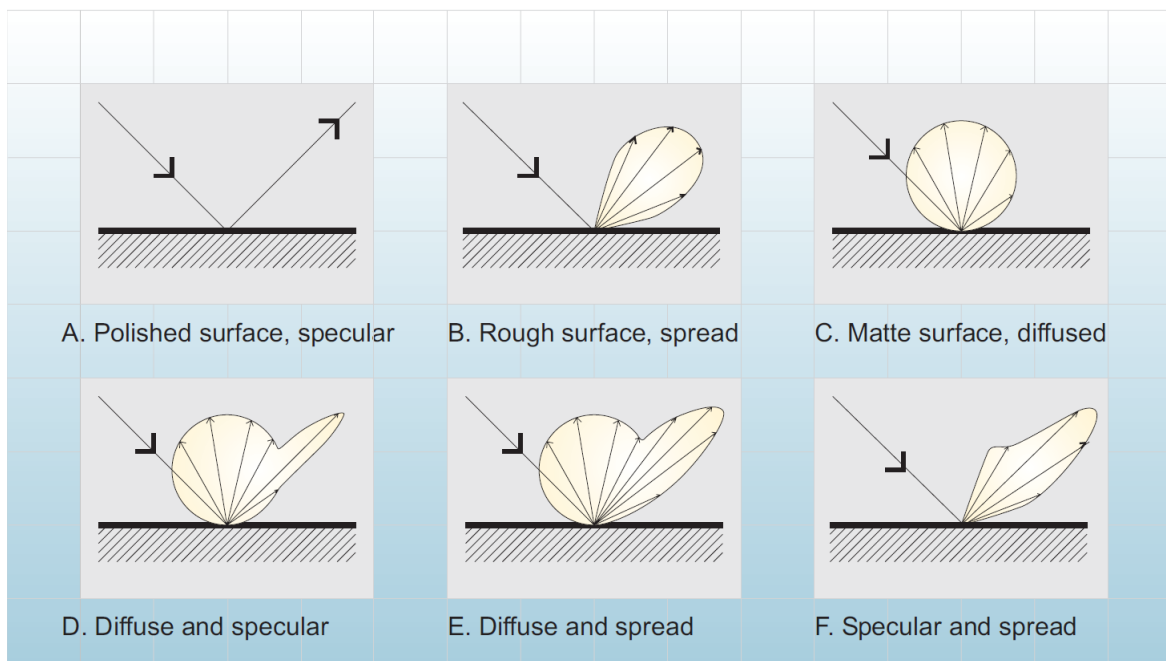
Figure 5.6: General types of reflector surfaces (illustrations from [94]).

aluminum. The inside can be either smooth or comprised of facets ranging from microscopic grains to segmented geometric facets in order to control the irradiance distribution as desired. The structure of the reflector surface determines the optical properties of the reflected light, as illustrated in Figure 5.6. *Specular* surfaces yields the highest direct reflection, but are also the most susceptible to physical defects such as scratching, denting or fluctuations during manufacturing. The reflector properties also depend on the wavelength dependency and quality of any optical coatings, which may change with age.

For reflectors made of glass, the surface is usually coated with specific materials to acquire the desired reflective characteristics, which includes coatings that have the possiblity to change the spectral properties of reflected light, something that traditionally have made the glass reflectors highly versatile. When applying reflective coating to any transparent medium, it's usually done on the side that faces the incoming radiation, to make a *first/front surface mirror* (FSM) if there is a desire to avoid the effects of the refractive properties of the medium the coating is applied onto. Thin glass is by itself an excellent reflector of light due to its refractive index and can achieve reflectivity of about 96%. Precise, thin curved glass reflectors are however hard to make [95], susceptible to mechanical shock and bulky to transport when the size goes up.

Metal reflectors are cheaper and easier to produce, however they are more limited in regards of control of the spectral output and more prone to geometric fluctuations during operation. High quality one-piece "spun" aluminum reflectors can be constructed by a technique known as metal spinning, utilizing a custom made tool to achieve the desired geometric characteristics of the reflector. A thin aluminum sheet is pressed onto the tool to form a crude reflector, and the further processed by polishing to a roughness in the the scale of 100 nm, before a final coat of aluminum is thin film deposited for high reflectance. A final coating of glass ($SiO_2$) can be applied by sputtering to prevent the aluminum from oxidizing. [96]. Anodized, specular aluminum has a total reflectivity of 85-90%. Highly reflective units (>90%) can be produced by depositing *metallic* coatings like aluminum onto the surface by evaporation, and subsequent polishing. Specular silver, vacuum-deposited onto a clear polyester film and adhered to a metal substrate have been shown to reach total reflectivities in the range of 91-95% [97]. Specular gold also have excellent reflective properties at wavelengths higher than about 600 nm, but is not usually a cost efficient choice. When enhanced with multiple thin-film *dielectric* coatings, the total reflectivity can be increased to 88-96%. A detailed review of the characteristics of different metallic and dielectric optical coatings can be found in the CVI Melles Griot Technical Guide [98]. *Dichroic* interference filter layers can be used for light sources which exhibit excess infrared radiation, by enabling much of the infrared radiation to pass through the reflector while the ultraviolet and visible wavelengths are concentrated at the focused spot. These coatings consist of approximately 40-60 very thin layers, each only a quarter wavelength of light thick and composed of alternating materials having a high and low refractive index [99]. Generally, reflectors without coating are cheaper but have higher attenuation than the coated counterparts.

Advances in materials science have resulted in several higher reflectance *diffuse-finish* materials, which include expanded polytetrafluoroethylene (PTFE), with a total reflectivity of 98.5%, and high reflectance white-painted metal reflectors, with a total reflectivity of 90–92%. The diffuse-finish materials allow for combining high efficiency with a uniform brightness appearance [97].

Most reflectors does make use of single-ended lamps, where the base connector is fixed or passing through the apex of the reflector and extends such that the light source is mounted in the center of the optical axis of the reflector. This means that there is a hole in the top of the

reflector, which casts a shadow along the light path which needs to handled at a different point in the optical train to ensure spatial uniformity. The alignment of the filament or arc is generally determined by the desired output beam characteristics. During alignment of arc lamps, attention should be paid to position the virtual image of the arc to one side or the other in order to avoid focus of the lamp's own emission onto the envelope wall, which can heat the bulb to excessive temperatures. The general notion is that as little radiation as possible should be reflected back onto the lamp to avoid jeopardizing the performance and integrity of the lamp, however studies how that it is possible to increase light intensity by recycling light from the arc back into the bulb [100]. For certain incandescent lamps, like tungsten-halogen, one can however design the reflector to direct parts of the infrared radiation back into the filament in order to spend less power to keep the filament at the correct temperature [97]. If the lamp is positioned close to the reflector, e.g. by large eccentricity ellipsoid reflectors, radiative stress due to high thermal loads should be expected on the reflective coating, which can lead to problems such as peeling [101] over extended use.

The optical quality of a reflective surface considers the accuracy of how the desired geometrical figure is reproduced. By grouping the geometrical deviations found in the material by spatial frequency, three major classifications of errors as seen in Figure 5.7 can be described [65, 102]: *Roughness*, which refers to high-frequency irregularities with a typical period lower than 1 mm. *Waviness*, which describes larger-scale deviations in the profile, and is generally in the range of millimeters to single-digit fractions of the entire structure. And *Form errors*, which describe the overall deviations from the desired ideal shape when disregarding the impact of roughness nad waviness. In general, the magnitude of this deviation is allowed to be higher than what is acceptable for roughness or waviness [103]. An in-depth description of causes, effects and solutions to these material errors can be found in the thesis of Dominguez (2012) [65].

Prefabricated reflectors are some times found categorized as by that of the floodlight photometric distribution types they provide, known as NEMA types 1 through 7 [104]. Type 1 is a very narrow beam (10–18 degrees) while type 6 is a very wide flood (100–130 degrees), where the beam angle is measured in degrees between the two opposite directions in which the average intensity is 50% of the center beam intensity [105].
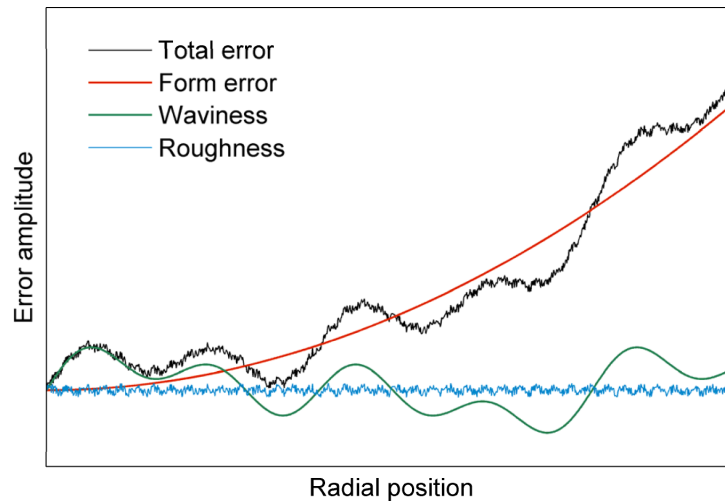
Figure 5.7: Material profile errors (illustration from [65]).

An overview of reflector design steps and prototype testing can be found in The IESNA Lighting Handbook [94], page 325. Software like OptiCAD [106] can be used to visualize and analyze optical models. By utilizing ray tracing techniques to validate the behavior of sources in conjucture with reflector designs, one can inspect processes like reflection, absorption or refraction, and estimate the irradiation distribution of the modeled assembly. It is however very important to properly model the light source geometry and any geometric restrictions imposed by the assembly components in order to get realistic results.

**Focusing Reflector (Elliptic)**

Focusing reflectors are geometrically designed to concentrate the light originating from a light source at the focus point close to the reflector wall on the center axis, into the other focus further away from the reflector. This is most commonly done by having an elliptical curve rotated around its center axis to generate an *ellipsoid* shape. The geometry of a elliptic reflector can be seen in Fig 5.8 a). As a result of the concentrating effect, the reflector generates an intensity characteristic that varies drastically as a function of distance from the focal point. In order to generate a sharp focus, the light source needs to be sufficiently small and placed very precisely inside the innermost focal point. Depending on the geometry of the lamp used, it may also feature a dark spot in the center due to shading from the lamp envelope. Ellipsoidal reflectors are considered an effective way of producing irradiation with controlled divergence, which in turn

can be collected and controlled by a lens or lens system.

A *spherical* reflector can be thought of as a special form of the ellipsoidal reflector where the two foci are coincident. Any light originating at the focus will be reflected and pass through the same point again. This is highly relevant to the thermal stress of light sources as discussed previously. However, the principle is often used in projecting devices to increase the amount of light collected by a lens, and in the design of reflectors for fluorescent lamps [94].

**Collimating Reflector (Parabolic)**

Collimating reflectors are made with a parabolic geometry in order to reflect radiation originating at a point source in the focal point of the parabola, or concentrate parallel incoming rays into the focal point. The geometry of a parabolic reflector can be seen in Fig 5.8 b). When the parabola is rotated around its center axis, the geometrical shape known as a *paraboliod* is swept out. Under the assumption of a perfectly specular reflector surface, a point source will produce a circular beam parallel to the center axis through the focus. Under realistic conditions, the emerging beam angle is mainly determined by the reflector's open aperture and the size of the lamp filament or arc spot where a larger lamp generates a greater deviation from truly parallel light.

The parabola can, like any feasible geometry used for collimation or concentration, also be extended into an elongated 'U' shape to facilitate a light source in the form of a line, creating a rectangular beam, or collecting parallel inbound radiation as is done by parabolic trough solar concentrators [107, 108]. Off-center segments of paraboloidal geometries can also be used to create off-axis focus points for concentration purposes.

### 5.1.3 Attenuators and Apertures

A variable aperture can be used to improve the collimation of a light source output, or to attenuate the magnitude of the simulator output by blocking parts of the irradiation, and is found in a number of commercial solar simulators. When using a variable aperture as part of the optical train to attenuate the intensity without having to adjust the drive current of the light source, it is important that the interference with the guided light does not disturb the spatial uniformity of the beam to an extended degree, and any performance degradation during partial attenuation
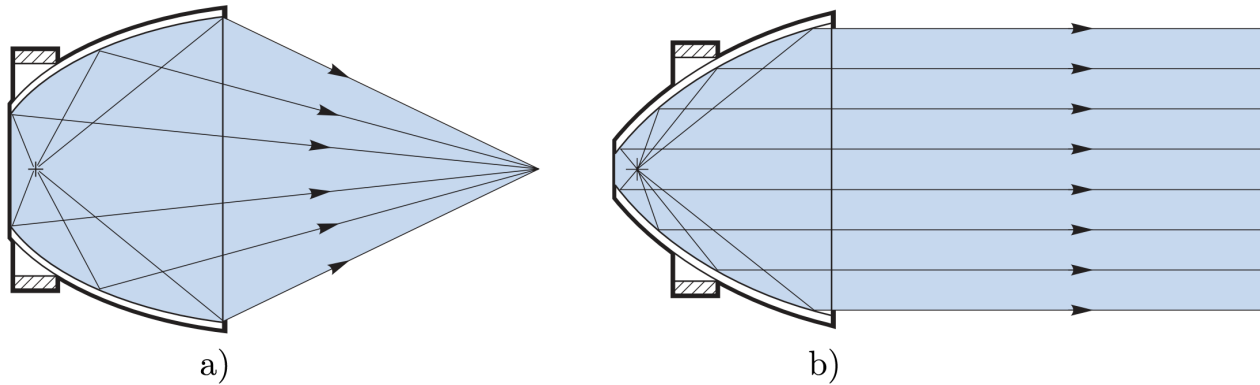
Figure 5.8: General elliptical (a) and paraboloidal (b) reflector geometries (illustrations from [26]).

should be informed by the manufacturer in the form of an accepted attenuation range, e.g. from 0.25-1 sun. Spectral and temporal performance should not be altered by use of an aperture.

Mesh attenuators, which basically is wavelength independent perforated metal, can be utilized to moderate system output without interfering with spatial or spectral uniformity. Very useful when armature current control is not practical due to normal operating ranges, the mesh attenuator can be installed and the current fine-tuned for desired output. These attenuators are usually fixed, however, and need to be manually switched out.

### 5.1.4   Spectrum Shaping Elements

No solar simulators can directly generate the exact identical radiation spectrum as can be found in the solar spectrum, due to the absorption of certain wavelengths by the atmosphere. The light sources used in solar simulation are usually filtered at some point during the optical train, by using a single filter or an array of subsequent filters to match the desired air mass (or other) conditions. Filters can for example be used to absorb selected wavelength bands, adjust color temperature, or add neutral density, all dependant on the light source utilized and the desired output. Note that the filters should be designed towards their application, as exposing certain filters to e.g. excess infrared radiation may degrade and eventually destroy the filter. Dichroic mirrors (interference filters with reflective backside) can be used to selectively remove undesired bands of radiation along the light path, similar to as mentioned in the section discussing reflectors and their coatings.

### 5.1.5 Spatial Uniformity

Spatial uniformity is usually ensured by the use of refractive *homogenizer* optics, or what's some-times referred to as the optical integrator, integrator lens, optical scrambler or "fly's eye". The refractive homogenizer is an array of small lenslets that mixes a large quantity of the light entering them and creates an "flat-top" uniform distribution of light upon exit. These microlenses are commonly used in assemblies of multiple units to ensure good mixing, and is found in applications which require a relatively large illuminated field within a short working distance, such as solar simulation. The integrator lenses are generally made of quartz, which has an average of 95% light transmission, thus use of integrator lens results in minimal loss of light yet contributes significantly to the beam uniformity. Systems that do not use integrator lens usually rely on metallic mirrors to reflect and homogenize the light [109].

The lens array needs to be handled with care due to its fragile nature, as it can disintegrate if subjected to excessive shocks.

### 5.1.6 Shutters

Mechanical shutters can be as simple as an on/off functionality to stop the light from the illumination source from reaching the work plane where the device under test (DUT) is located. As most lamps employed in solar simulation take a while from powering on to reaching stable operating conditions, and seein as neither arc nor incandescent lamps handles rapid or frequent turning on and off very well, having a way to shut off the illumination without having to power off the light source is very practical. The shutter should be located after any spectrum shaping or homogenizing elements in order to allow these components to stay at thermal equilibrium even when the work plane is not illuminated.

Shutters can also function as optical choppers to convert the continuous illumination into a pulsed light source, and is typically controlled by fast response actuators like a solenoid, with the necessary utilities to provide a fixed timing or frequency.

### 5.1.7 Collimator Lens

The last component of an optical train which include concentrating components is often a collimator lens with characteristics determined by the dispersion of the light entering the lens, such that the output is parallel and suited for uniform illumination of the work plane. The lens is often found in a plano-convex shape or equivalent, and can be found referred to as a *condenser* lens.

Prismatic lenses can be made of glass, acrylic or polycarbonate. Glass is a very durable material that remains clear over life, although it can be heavy, fragile, and more expensive than plastic materials. Acrylic remains clear over life, is much lighter than glass, but cracks easily. Acrylic cracks easily, however. Polycarbonate lenses are tougher, but many polycarbonates yellow and become brittle with exposure to UV radiation [97]. In practice, most solar simulators utilize borosilicate lenses, or fused quartz/silica lenses if UV output is needed.

### 5.1.8 Work Plane

The work plane, some times referred to as *test plane area* [110], is the illuminated area which is intended to contain the device under test (DUT), and the irradiance monitor used to classify the solar simulator. Device performance is assessed and characterized at this location. It is usually defined as a bounded region within a certain distance away from the final part of the optical train delivering the irradiance from the light source, most often resulting in a rectangular cubic volume where operation under normal conditions can be expected.

### 5.1.9 Photofeedback

Some solar simulators employ optical sampling heads and control loop electronics in order to improve output stability, by using the signal from a light sensor in a feedback loop to control the power supply output voltage and/or current. A variety of commercial devices are capable of improving the stability of arc and halogen sources from 0.01 to 0.4 percent [74]. However, these figures represent total light output, and the control devices cannot prevent phenomena such as arc flares or flutter which results in localized flickering which may be projected unevenly into the work plane. It can however minimize the fluctuations caused by the lamp power supply, and

even be integrated with software for automated normalization of measurements.

## 5.2 Continuous and Pulsed Simulators

Solar simulators can be divided into three main groups determined by how they are designed to perform measurements; *Continuous/steady-state*, *single-pulse* and *multi-flash* [65].

### 5.2.1 Continuous/Steady-state Simulators

ASTM define a steady-state simulator as a simulator whose irradiance output at the work plane is continuous for periods of a second or greater [110].

Simulations done by steady-state simulators suffer from thermal gradients due to the longer irradiation exposure, meaning that a temperature control loop must usually be incorporated into the work plane to be able to actively reduce the temperature during measurements. While this problem is manageable for normal STC solar simulation, it is a nontrivial challenge for concentrated sunlight simulators due to the massive heat flux on a relatively small surface.

The life expectancy of steady-state simulator lamps depends on the illumination source used, where the commonly found xenon arc lamps generally have an expected lamp life of about 1,000 hours. Some continuous simulators are also equipped with control systems which reduce the operating current of the lamp when the shutter is closed, which contributes to lengthening the life span of the lamp [109].

Steady-state light simulators also generally does not exhibit certain problematic behavior commonly encountered with measurements performed by flash simulators, such as distortion of the I-V curve due to capacitance effects, or the need for curve correction if the scan duration is too slow [111].

### 5.2.2 Pulsed Simulators

According to ASTM, a pulsed simulator is a simulator whose irradiance output at the work plane is in a single short duration pulse of 100 ms or less. Due to the very short irradiation time period which can leave a window of only a few milliseconds with steady conditions during the flash,

the measurements have to be done in a extremely fast manner - typically the I-V data points are taken in about 1.5 ms in intervals of tens of microseconds. It is important that the device under test, be it a cell, module or array, has reached the appropriate electrical output levels before the sampling is started, and that the device possess a rapid enough response to keep up with the DAQ [110]. Pulsed simulators generally have an expected lamp life ranging from 40,000 up to 1 million flashes [112]. Many thin-film photovoltaic technologies cannot be characterized by using pulsed sources, as their electrochemical response time — which can be on the order of 50–2000 ms — is longer than the length of the pulse [113].

**Single-pulse**

Single-pulse simulators require a stable light intensity plateau for the duration of the voltage sweep to ensure that the characteristics of the cell are accurately represented. Depending on the materials of the device being tested, the high-frequency sampling measurements may however be subjected to transient artifacts induced by the rapid voltage sweep. This is especially relevant for high-efficiency silicon devices [114]. Testing during these short intervals is generally not a problem for proper simulators, but it does often mean fewer sample points for the measurement of the I-V curve.

**Multi-flash**

Whereas steady-state and single-pulse simulators perform continuous measurements of the I-V curve in its entirety, multi-flash simulators sample only one point on the I-V curve for each pulse of the flash, meaning that the pulse energy is much lower than for single-pulse testing. Like for steady-state simulators, the DUT can normally be assumed to be in equilibrium during testing [65]. Multi-flash simulators also benefit from the lack of potential temporal instability due to the short exposure.

## 5.3 Performance Classification

Measuring solar cells requires a stable light source that closely matches the conditions of sunlight. Not only the intensity but also the spectrum must be matched to a standard. An obvious

option is to simply use the sun itself, which may be a good solution in locations with few clouds [115], but there are still variations in atmospheric conditions that require correction to compare measurements over time. The spectrum also changes throughout the day and this further limits the time for testing.

The most common solution is to use an artificial light source that simulates the sun. The ideal illumination source would have following features [116]: A spatial non uniformity of less than 1%, a variation in total irradiance with time of less than 1%, be filtered for a given reference spectrum to have a spectral mismatch error of less than 1%, and have an angular distribution similar to the reference solar disk.

There exist three standards for solar simulators employed in photovoltaic appliactions; ASTM E927 [110], IEC 60904-9 [117] and JIS C 8912 [118], where JIS is the Japanese equivalent to the IEC. These standards contain common specifications for indoor testing of terrestrial flat plate (nonconcentrating) photovoltaic devices where solar simulators are used to supply irradiance.

The light produced by a solar simulator should be controlled with respect to the three specific attributes as discussed in the following sections; *spatial uniformity, temporal stability* and *spectral content.*

### 5.3.1 Spatial Uniformity

Also refered to as irradiation nonuniformity or irradiance inhomogeneity. Requires non-uniformity of irradiance over the illumination area of the module to be measured less than $x_{su}$ %, and is calculated as

$$x_{su} = \pm 100 \left( \frac{\text{Maximum Irradiance}(x, y) - \text{Minimum Irradiance}(x, y)}{\text{Maximum Irradiance}(x, y) + \text{Minimum Irradiance(x, y)}} \right) \tag{5.1}$$

where the maximum and minimum irradiances are measured within the confines of the work plane of the simulator, thoughout a matrix of equally spaced positions.

## 5.3.2 Temporal Stability

Irradiance stability over time. Requires temporal instability of irradiance during measurements of less than $x_{ts}$ %.

$$x_{ts} = \pm 100 \left( \frac{\text{Maximum Irradiance}(t) - \text{Minimum Irradiance}(t)}{\text{Maximum Irradiance}(t) + \text{Minimum Irradiance(t)}} \right) \tag{5.2}$$

where the maximum and minimum irradiances are measured at a fixed location in the solar simulator work plane, with the spread generated by the irradiance varying with time over a period equal to the measurement period. The period can be made up from all moments $t$ during I-V curve measurement by steady-state or pulsed simulators, or a single point during multi-flash testing.

## 5.3.3 Spectral Content

Requires spectral match factor of emitted light to the AM1.5 solar reference spectrum (or AM0 for extraterrestrial) as defined in e.g. IEC 60904-3 [38] to deviate less than $x_{sc}$ (per 100 nm range).

The calculation of spectral matching quality is more complicated and is based on spectral irradiance measurements. The appropriate radiation wavelength range of 400 nm to 1100 nm, is divided into six wavelength intervals (400-500-600-700-800-900-1100) as can be seen summarized in Table 5.1 and evaluated as follows:

Step 1: Determine total irradiance within the specified wavelength range.

Step 2: Calculate the percentage contribution of each interval to total irradiance, which are fixed values for the spectral distribution in question.

Step 3: Calculation of light source/solar spectrum ratios from the each of the values in the previous step. A perfect match inside a wavelength interval is represented by a spectral match ratio of unity.

Step 4: The spectral match class of the solar simulator is determined by investigating which of these values have the largest deviation from 1.

Table 5.1: Spectral distribution of irradiance performance requirements.

| Wavelength interval [nm] | Percent of total irradiance | | |
|---|---|---|---|
| | AM0 | AM1.5G | AM1.5D |
| 300-400 | 8.0 | N/A | N/A |
| 400-500 | 16.4 | 18.4 | 16.9 |
| 500-600 | 16.3 | 19.9 | 19.7 |
| 600-700 | 13.9 | 18.4 | 18.5 |
| 700-800 | 11.2 | 14.9 | 15.2 |
| 800-900 | 9.0 | 12.5 | 12.9 |
| 900-1100 | 13.1 | 15.9 | 16.8 |
| 1100-1400 | 12.2 | N/A | N/A |

### 5.3.4 Performance Requirements

It should be kept in mind that for any photovoltaic measurement, the choice of simulator class should be based on the needs of that particular measurement. For example, the spectral distribution requirements need not be stringent if identical cells off an assembly line are measured for the purpose of sorting according to voltage. A given simulator may meet different performance classes depending on the particular test conditions. For example, the uniformity of irradiance may be very good for individual cell testing, but quite poor for modules [110].

According to IEC 60904-9 [117], and seen in Table 5.2 each attribute is classified as one out of three possible grades: 'A', 'B', or 'C', with 'A' being the top rating and 'C' being the lowest. An additional, unofficial grade, 'A+', have also been introduced by TÜV Rheinland to reflect recent progress in solar simulator technology [73]. ASTM [110] and JIS [118] have corresponding standards with minute differences to IEC.

The highest official system classification is given by the rating of AAA, where the first letter indicates spectrum quality, the second letter indicates the uniformity of irradiance on the test area, and the third letter signifies the temporal stability of irradiance.

Table 5.2: Solar simulator classifications.

| Class | Spectral match | Irradiance homogenity | Temporal instability | |
| --- | --- | --- | --- | --- |
| | | | Long term | Short term |
| A+ | 0.875 - 1.125 | < 1% | < 0.5% | < 1% |
| A | 0.75 - 1.25 | < 2% | < 0.5% | < 2% |
| B | 0.6 - 1.4 | < 5% | < 2% | < 5% |
| C | 0.4 - 2.0 | < 10% | < 10% | < 10% |

# Chapter 6

# Experiment

After some investigation of resources available to conduct experiments with the NUTS solar cells, mainly at the NTNU Insitute of Engineering Cybernetics, contact was eventually made with Prof. Turid Renaas, whom is responsible for the Optical Calibration lab at NTNU Department of Physics. An agreement to use said lab for the intents of this thesis was made, and arrangements for training and follow up contact was made with Dr. Xiaodong Yang, also at Department of Physics.

## 6.1   Laboratory Setup

A schematic of the laboratory setup used for the solar cell experiment can be seen in Figure 6.1. The individual components are further discussed in their respective subsections.

### 6.1.1   Solar Simulator

The solar simulator used in these experiments is manufactured by ABET Technologies, and is from the Sun 2000 family, model 11018. It has a downward-pointing output which delivers irradiance of about 1 sun, is fitted with an AM1.5G spectrum filter, and limits UV exposure by utilizing an N-BK7 condenser lens [119]. It can however not properly simulate the AM0 conditions found in space, which is the major limiting factor for using this equipment to test our satellite solar cell.
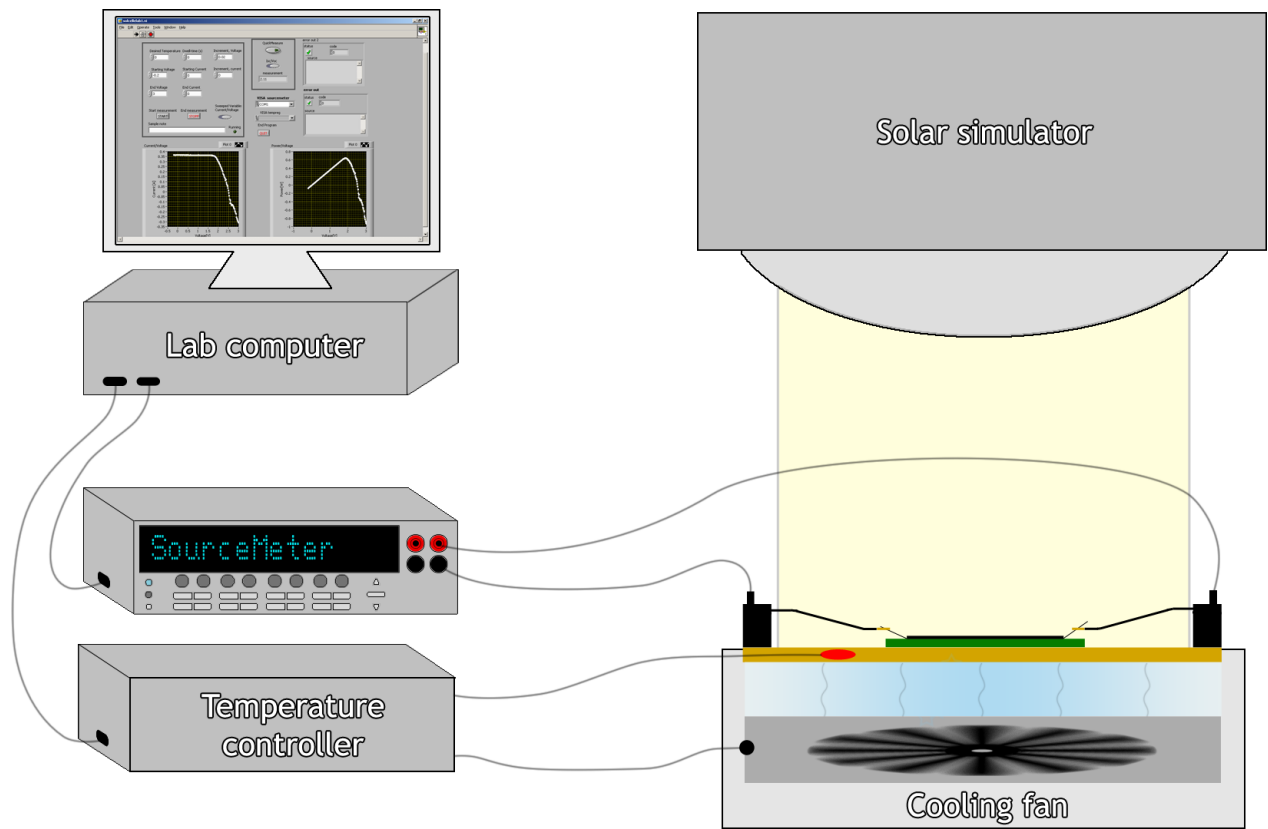
Figure 6.1: Schematic of laboratory setup during experiment.

Table 6.1: ABET Sun 2000 solar simulator specification [119].

| Model # | Field size (mm) | Stability (%) | Uni-formity (%) | Lamp (W) | Ozone free | Lamp life (h) | Working distance (mm typ.) | Irradiance AM1.5G (max typ.) | AM1.5G spectral match |
|---------|------|-----------|-----------|------|-------|--------|-----------|-----------|-------|
| 11018 | 160x160 | 1 | 5 | 550 | Yes | 1500 | $200 \pm 50$ | 1.3 suns | A |

The actual solar simulator found at the lab can be seen in Figure 6.2, with it's administrative settings side panel depicted in Figure 6.3, where it is possible to tune armature current to the illumination source, operate the shutter controller with timer [120], and power on/off the source and its cooling fan. The summarized device data sheet from the manufacturer can be seen in Table 6.1.

**Optical Train**

A schematic of the inner workings of the solar simulator illumination source and optical pathing can be seen in Figure 6.4. The light source is a high radiance DC Xenon short arc lamp, energized by a power armature which draws around 21.5 A during operation at irradiation equivalent of 1 sun (1000 W/m$^2$), and the default 550 W bulb has a stated operating range between 15.5 and 28 A [121]. The illumination source is located near one focus inside an elliptical reflector which directs most of the generated light towards the second focus point and the first of two mirrors The mirror is a 90° reflector which can be full spectrum or dichroic, and also serves to keep the overall device compact due to efficient optical pathing towards the downward-facing output. The mirror directs the light flux through spectrum shaping filters which modifies the spectrum to that of the desired output, in this case the AM1.5G spectrum, and through a set of homogenizing lenslets which ensures that the illumination is uniformly distributed. The adjustable spacing lenslet arrays provide both the homogenization of the beam and allow for a slight adjustment of the size of the illuminated field. A shutter to block the light from proceeding to the work area without having to shut off the illumination source is located *after* the spectral and illumination enhancers, such that these can be exposed continuously and operate in thermal equilibrium. Finally the light propagates towards the second 90° reflector which folds the optical path back to vertical, and passes through a condenser lens which, in conjunction with the elliptical reflector and homogenizer, provide the final collimation to produce an uniform irradiance down to
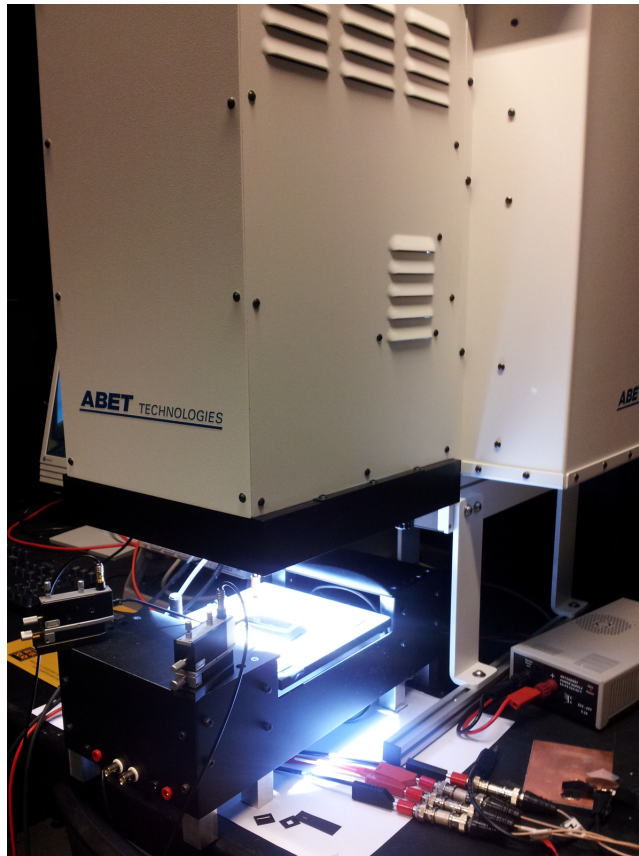
Figure 6.2: Photo of ABET Technologies Sun 2000 Solar Simulator at optical calibration lab.



Figure 6.3: Photo of solar simulator control panel
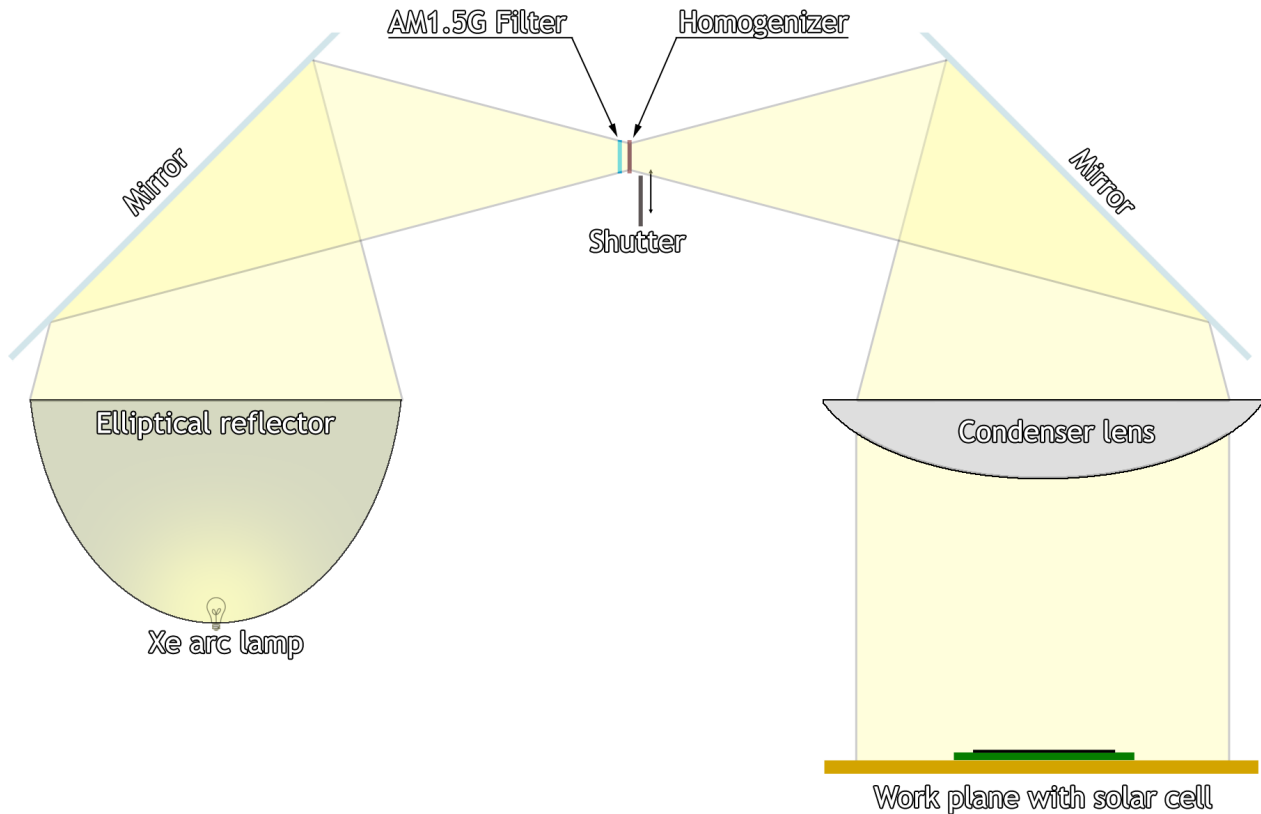
Figure 6.4: Schematic of the solar simulator optical train (inspired by [121]).

the work plane within a specified range of working distance.

### 6.1.2 Temperature Controller

The temperature controller receives input describing the desired temperature behavior from the computer, and then proceeds to monitor the work plane temperature through measurement input, with a sampling frequency of 20 s$^{-1}$, or a sampling period of 0.05 s. As the work plane is exposed to irradiance of about 1000 W/m$^2$, it will naturally increase in temperature during operation of the simulator when the shutter is open. When the registered temperature reaches certain values, the temperature controller outputs a current to drive an electrical fan mounted under the work plane, as seen in the schematic of Figure 6.1. This will then reduce the temperature until measurements are low enough for the controller to shut the fan back off.

The temperature controller is of the make Supercool Regulator Board, based on the PR-59 advanced temperature controller, as depicted in Figure 6.5. The solution was developed by Swedish company Coollab AB (Supercool), which was later acquired by multinational corpora-
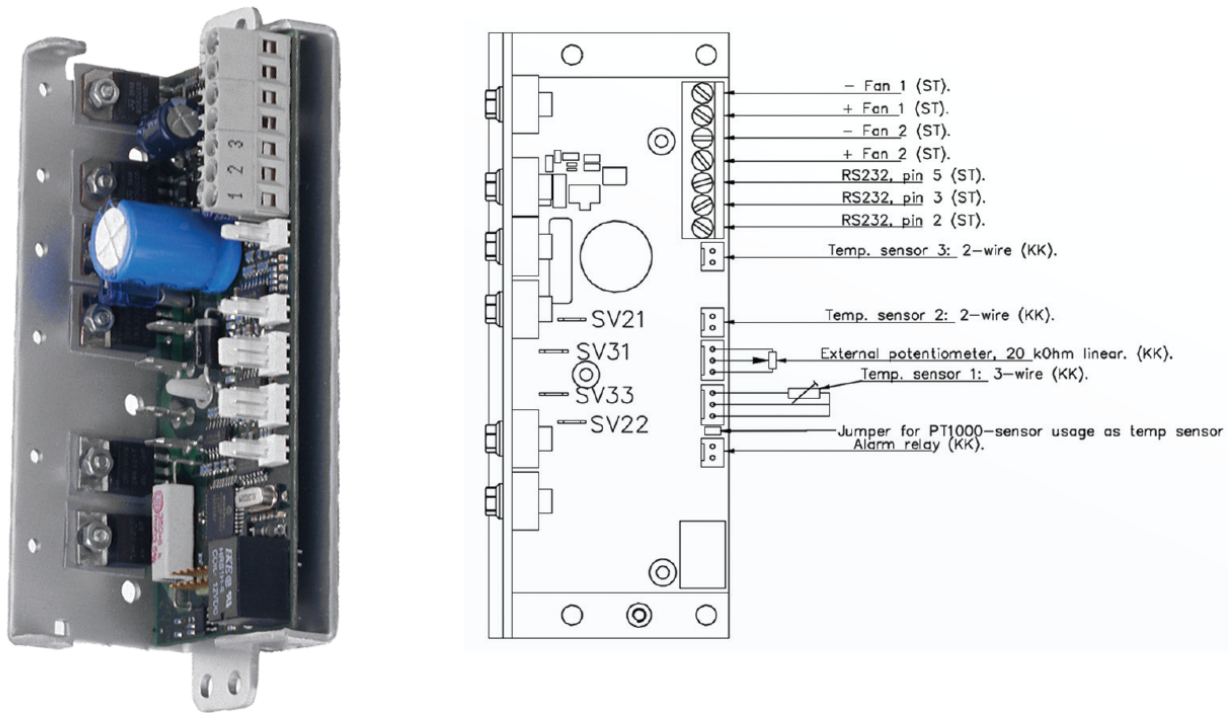
Figure 6.5: PR-59, TC-XX-PR-59 Temperature Controller (adapted from [122]).

tion Laird Technologies with headquarters in USA, in 2006. The physical temperature controller is used in conjunction with its software, which is described in the section about the laboratory computer.

### 6.1.3 Sourcemeter

The Keithley Model 2440 5A sourcemeter as can be seen in Figure 6.6 is both a highly stable, programmable DC power supply source, as well as a true instrument-grade 5½ digit multimeter with high repeatability. It can act as a voltage source, a current source, a voltage meter, a current meter, and an ohmmeter. In the lab it is connected to the computer via a Rs232 link, and controlled remotely for making I-V measurements of photovoltaic devices in correspondance with the solar simulator.

The Keithley SourceMeter is a bipolar power supply, meaning that one is able to measure I-V curves over both positive and negative voltages due to the fact that the load have to be able to sink the current from the photovoltaic device. This is done by means of active electronic loads, and can be seen illustrated in Figure 6.7. Other popular bipolar power supplies are Kepco BOP
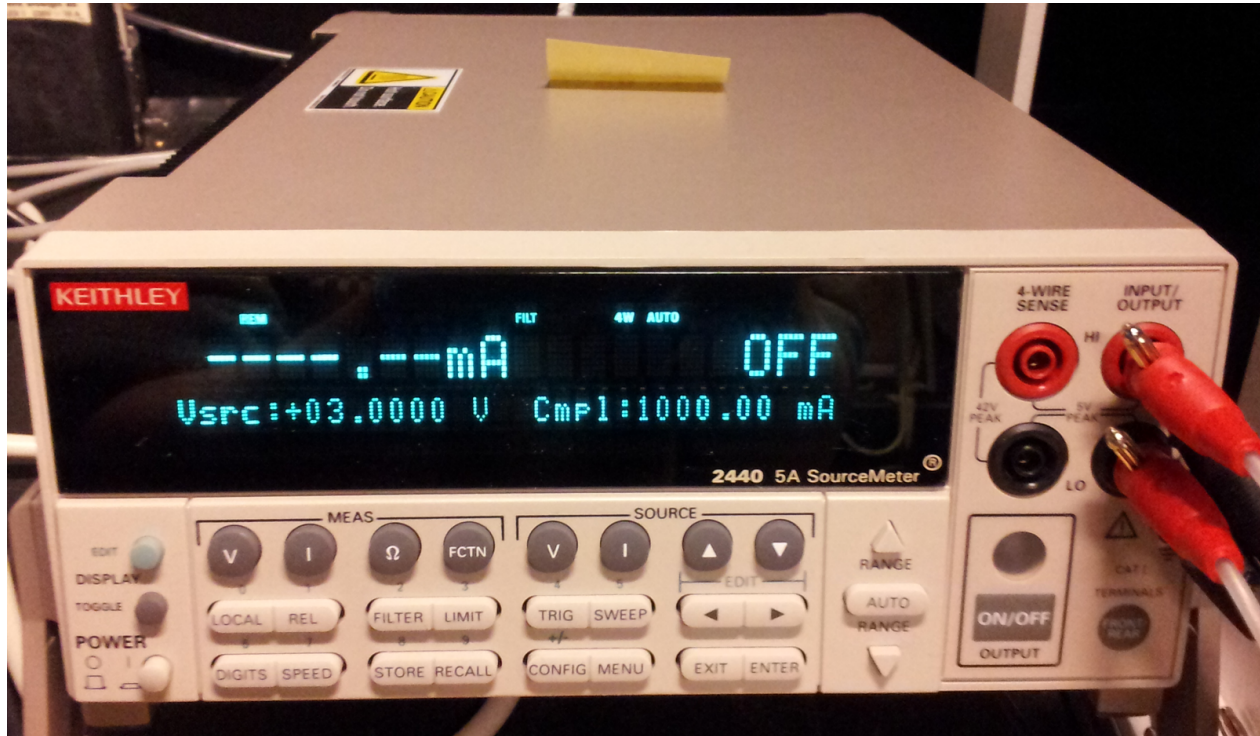
Figure 6.6: Photo of Keithley SourceMeter Model 2440 at optical calibration lab.

bipolar power supplies and Kikusui electronic loads.

☞ **Sink**: The ability of allowing negative currents at positive voltages, using an active load.

### 6.1.4 Reference Cell

The reference cell used for calibrating the solar simulator lamp illumination during preparation to make I-V measurements can be seen in Figure 6.8, with the information from the manufacturer found in Table 6.2. The back of the solar cell is attached to the device in such a way that a good heat transfer to the device housing is guaranteed. A Pt100 RTD temperature sensor is mounted below the cell to allow monitoring of device temperature. The device is not shunted allowing the whole IV-curve to be measured. The solar cell is protected by a high quality fused silica window, assuring spectral sensitivity over a 320 -1100 nm range. It has been calibrated by the Radboud University Nijmegen PV Measurement Facility.
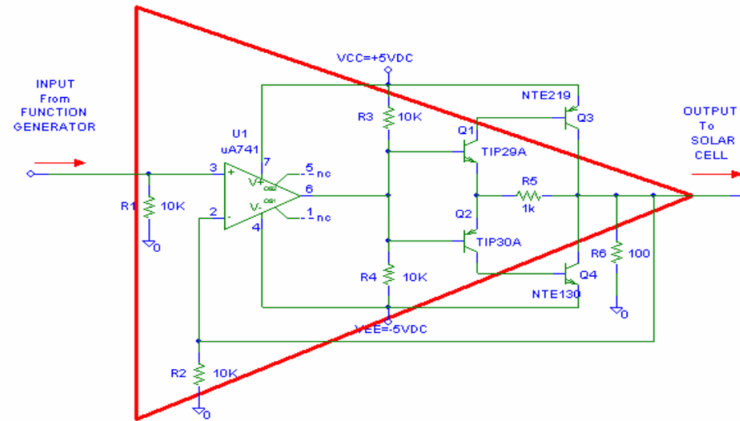
Figure 6.7: Active electronic load operating principle. [77]



Figure 6.8: Photo of Rera Systems photovoltaic reference cell.

Table 6.2: Rera Solutions reference cell product specifications [123].

| Material | Mono crystalline silicon |
|---|---|
| Area | 20 mm x 20 mm |
| Dimensions (l x w x h) | 104 mm x 74 mm x 14 mm |
| Weight | 225 g |
| Operating Temperature | 10°C to 40°C |
| Environment | Indoor usage |
| Encapsulated | High grade solar cell encapsulant |
| Solar Cell Connection | 4 Wire (or if shunted 2 Wire) |
| Protective Window | Quartz |
| Temperature Sensor | Pt100 |
| Socket Solar Cell | LEMO EGG.00.304.CLL |
| Socket Pt100 | LEMO EGG.00.303.CLL |
| Parameters | $I_{sc}$, $V_{oc}$, $I_{mpp}$, $V_{mpp}$, Fill Factor, Efficiency |
| Calibration | AM1.5G, 25°C, 1000 W/m$^2$ |
| Typical $I_{sc}$ | 100 mA |
| Error $I_{sc}$ | ± 3% |

## 6.1.5 Computer with Software

Main task of running the I-V measurement software and SC_Interface, the software counterpart to the Supercool Regulator Board temperature controller, allows the user to set the desired behavior of the temperature measured from the solar simulator's work plane with a hardcoded sampling frequency of 50 ms. This is realized by an online P(I)(D) controller with tuneable parameters which should keep the temperature at a chosen setpoint. Under chosen STC, the temperature setpoint is 25 °C.

## 6.1.6 Solar Cell: Azurspace 3G30C Electrical data

It should be noted that the NUTS satellite project will invest in new solar cell assemblies when building the launch model. The cell(s) used for testing are of a slightly older model, and is not publicly available from the manufacturer anymore.

The electrical data in table Table 6.3 is specified in terms of beginning-of-life (BOL) characteristics, as well as what is stated as 5E14, 1E15 and 3E15, which is the characterization after high energy irradiation of $5 \times 10^{14}$ 1MeV electrons/cm$^2$, and similar for the other two listings of 1E15 and 3E15 respectively.

Table 6.3: Azurspace 3G30C solar cell electrical data (see complete data sheet in Appendix B).

| Electrical data | | | | BOL | 5E14 | 1E15 | 3E15 |
|---|---|---|---|---|---|---|---|
| Average open circuit voltage | $V_{oc}$ | (mV) | | 2669 | 0.94 | 0.92 | 0.89 |
| Average short circuit current | $I_{sc}$ | (mA) | | 525 | 0.99 | 0.96 | 0.87 |
| Voltage at maximum power | $V_{mp}$ | (mV) | | 2379 | 0.93 | 0.91 | 0.88 |
| Current at maximum power | $I_{mp}$ | (mA) | | 505 | 0.98 | 0.95 | 0.86 |
| Average efficiency | $\eta_{bare}$ | (%) | | 29.1 | 0.91 | 0.87 | 0.76 |

| Acceptance values | | |
|---|---|---|
| Voltage | $V_{op}$ | 2300 mV |
| Minimum average current @ $V_{op}$ | $I_{op\,avg}$ | 510 mA |
| Minimum individual current @ $V_{op}$ | $I_{op\,min}$ | 475 mA |

*Standard: CASOLBA 2005 (05-20MV1, etc); Cell Type: 3G-28%;*
*Spectrum: AM0 WRC (1367 W/m$^2$); T = 28° C*

## 6.2  Initial I-V Measurement

See Appendix C for a detailed description of the standard lab protocol for making use of the solar simulator for taking measurements.

After careful setup, five measurements of the solar cell I-V characteristics were taken at AM1.5 STC. A multitude of measurements were done in order to be able to see whether or not the results were consistent between each measurement, and to create an average measurement for increased accuracy. All measurements were taken using the same conditions of irradiance, temperature and instrument settings. The voltage resolution (step size) was set to 0.02 V for the entirety of the measurement session. The LabView measurement output current and voltage data were collected in a datasheet and imported to MATLAB for calculation and graphical illustration.

With the measurement results illustrated in Figure 6.10 (a), one can see that the results are very much identical for most intents and purposes, and displays the shape one would expect of a proper I-V curve with the solar panel's diode-like behaviour. The curve made from the average measurement pairs is shown in Figure 6.10 (b), with a 95% confidence interval generated from the sample population and special focus on the crossings with the axii, where $V_{oc}$ and $I_{sc}$ are
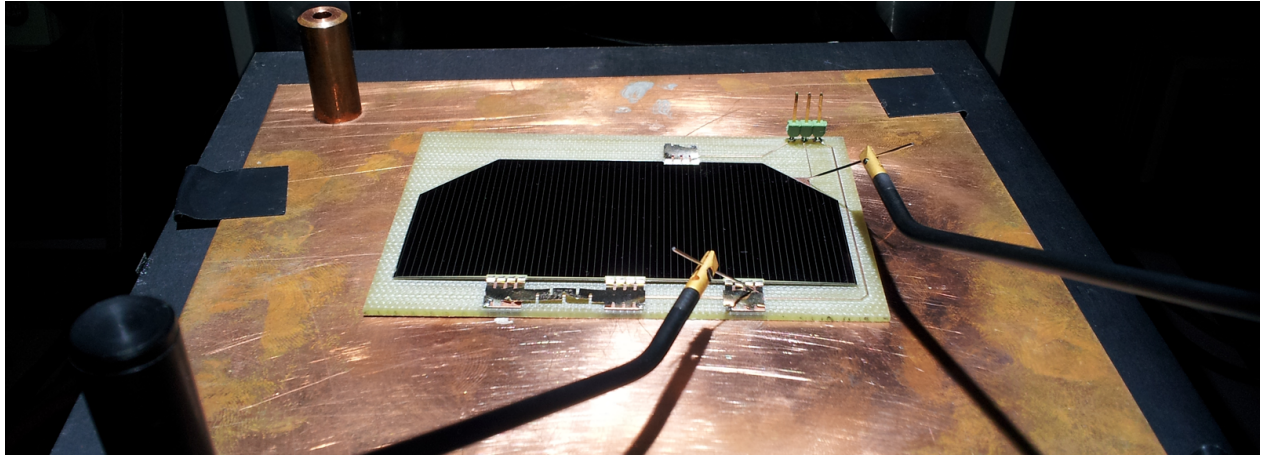
Figure 6.9: Photo of solar simulator I-V measurement of solar cell.
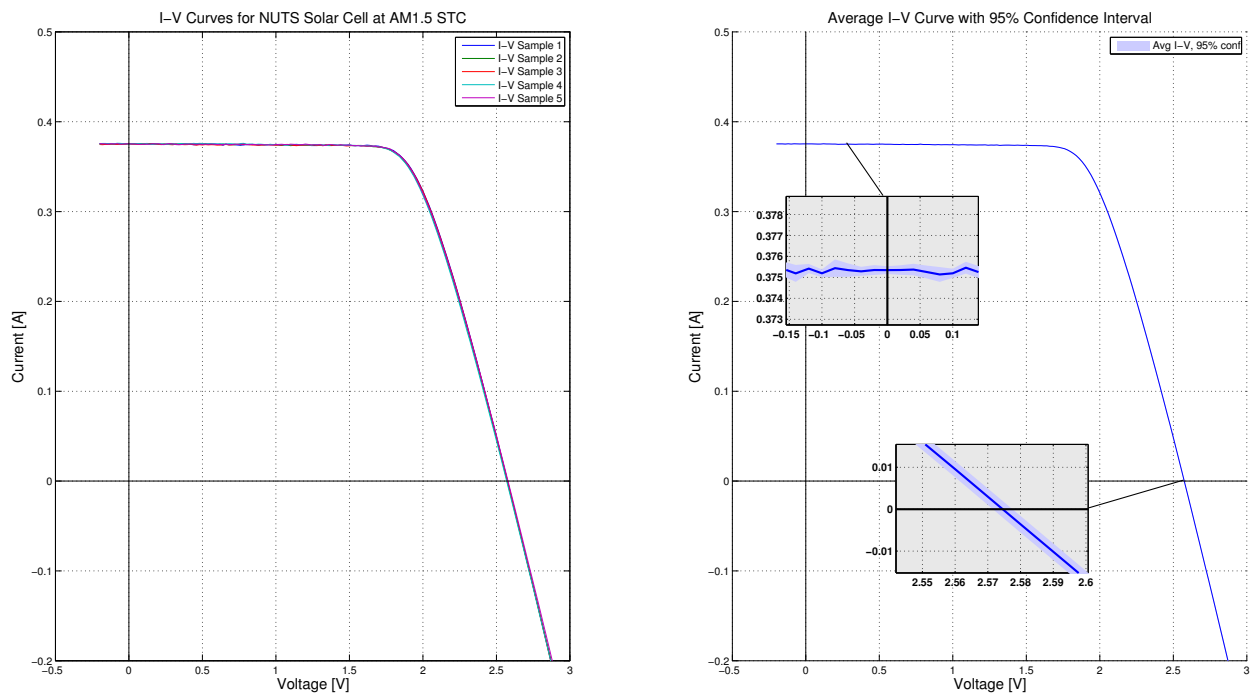


Figure 6.10: (a) I-V measurements of solar cell. (b) Average I-V curve with 95% conf. interval.
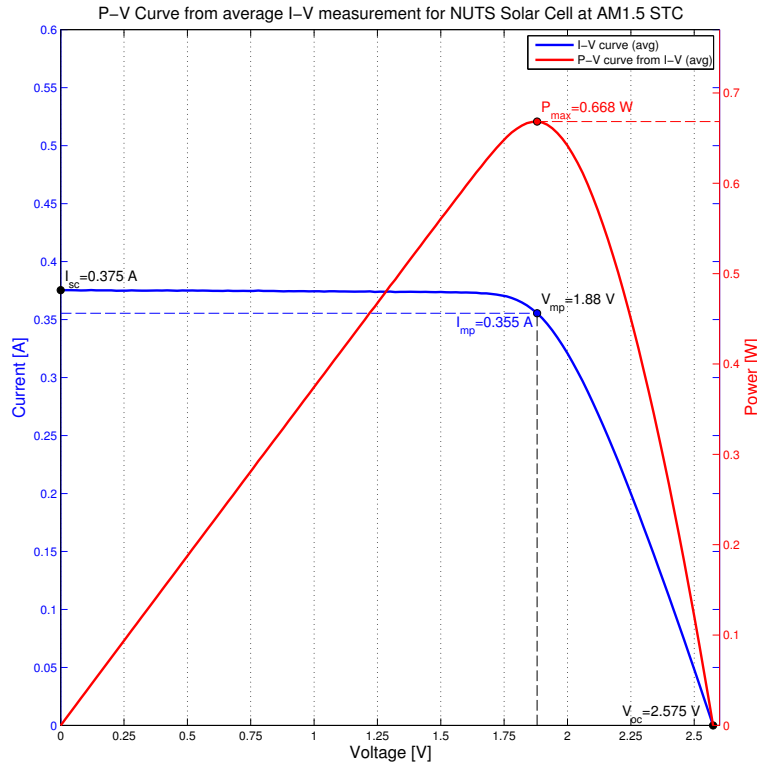
Figure 6.11: P-V curve from average I-V measurement.

located.

In Figure 6.11 we can see the most important characteristics of the solar cell displayed, gathered from the I-V curve constructed by average discrete measurement points.

The curve near the open circuit voltage $V_{oc}$ can be considered linear, and MATLAB was used to create an interpolation with the individual/average I-V curve to find a fitted value between the discrete measurement sample points. This gives a more precise value compared to taking a sample point close to the corresponding intersection of the zero axis.

As with the open circuit voltage, the short circuit current $I_{sc}$ could be found by the use of interpolating the average I-V curve in MATLAB, however our sample population includes the current value for V = 0, which yields the same result.

The values for power were initially created by multiplying the corresponding sample data elements for current and voltage. This means that the maximum power value, $P_{max}$, is located at a single discrete measurement point, and that if the true value of $P_{max}$ is between the sample points, it will not be found.
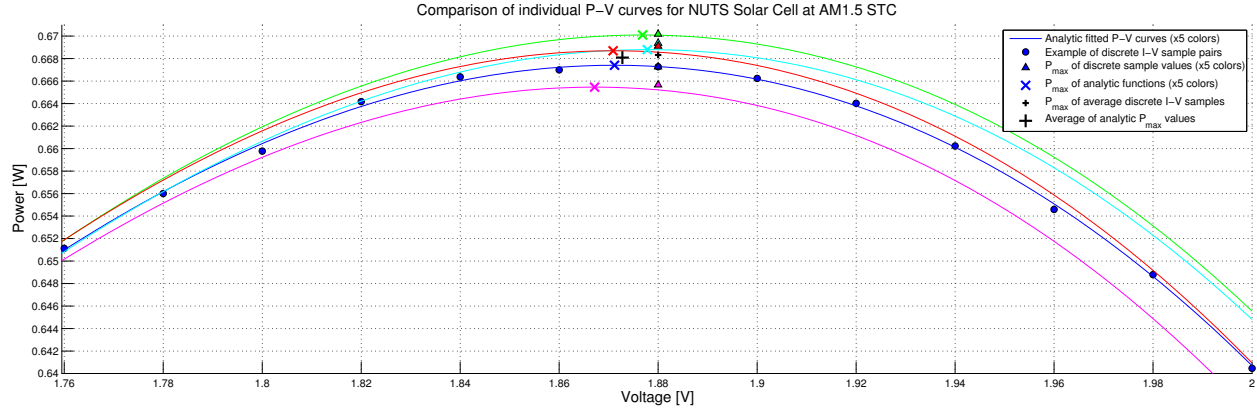
Figure 6.12: Analytical functions fitted to discrete P-V values around $P_{\text{max}}$.

A more precise method for obtaining the values related to the maximum power point is to construct a fitted polynomial in the vicinity of $P_{max}$, which allows us to calculate the values analytically. Using a 10% region span around the maximum power point found for the average I-V curve, we bound our polynomial fit to $(\frac{V_{\text{mp avg}}}{V_{\text{oc}}} - 0.05)V_{\text{oc}} \leq V \leq (\frac{V_{\text{mp avg}}}{V_{\text{oc}}} + 0.05)V_{\text{oc}}$, and used MATLAB to construct a fitted curve, by means of least squares method. This was done for all five I-V measurements in order to get more accurate values for $P_{\text{max}}$, $V_{\text{mp}}$ and $I_{\text{mp}}$, and can be seen in Figure 6.12. For illustration purposes, the process is shown for one of the sets of measurement data, where the 3$^{\text{rd}}$ order polynomial approximation to the power values on the defined interval was found to be

$$P(V) = -1.176V^3 + 5.145V^2 - 6.899V + 3.269 \tag{6.1}$$

which when derivated with respect to voltage, set equal to zero and solved yields

$$\frac{\mathrm{d}P}{\mathrm{d}V} = -3.528V^2 + 10.290V^2 - 6.899 = 0$$
$$\Rightarrow V = 1.8712 \cup V = 1.0448 \tag{6.2}$$

where the second root is clearly outside the interval and can be disregarded, such that $V_{\text{mp}} = 1.8712$ V. From this, a value of $P_{\text{max}}$ and the corresponding $I_{\text{mp}}$ can be found from Equation 6.1 and $P = VI$, respectively.

The parameters extracted from the individual measurement data sets via analytical or numerical means can be found compared to eachother in Table 6.4. As can be seen, the individ-

Table 6.4: I-V parameters from discrete numerical, and analytical power expressions

| I-V # | Analytical | | | | | Numerical | | | | |
|---|---|---|---|---|---|---|---|---|---|---|
| | $I_{sc}$ | $V_{oc}$ | $I_{mp}$ | $V_{mp}$ | $P_{max}$ | $I_{sc}$ | $V_{oc}$ | $I_{mp}$ | $V_{mp}$ | $P_{max}$ |
| 1 | 0.3756 | 2.5759 | 0.3570 | 1.8768 | 0.6701 | 0.3756 | 2.58 | 0.3565 | 1.88 | 0.6702 |
| 2 | 0.3753 | 2.5730 | 0.3567 | 1.8712 | 0.6674 | 0.3753 | 2.58 | 0.3549 | 1.88 | 0.6673 |
| 3 | 0.3753 | 2.5754 | 0.3562 | 1.8778 | 0.6688 | 0.3753 | 2.58 | 0.3560 | 1.88 | 0.6694 |
| 4 | 0.3751 | 2.5696 | 0.3564 | 1.8672 | 0.6655 | 0.3751 | 2.58 | 0.3541 | 1.88 | 0.6657 |
| 5 | 0.3755 | 2.5788 | 0.3574 | 1.8709 | 0.6687 | 0.3755 | 2.58 | 0.3559 | 1.88 | 0.6691 |
| Average | 0.3753 | 2.5745 | 0.3567 | 1.8728 | 0.6681 | 0.3753 | 2.58 | 0.3554 | 1.88 | 0.6683 |

*(Remark: Units measured in [V], [A], or [W], where applicable)*
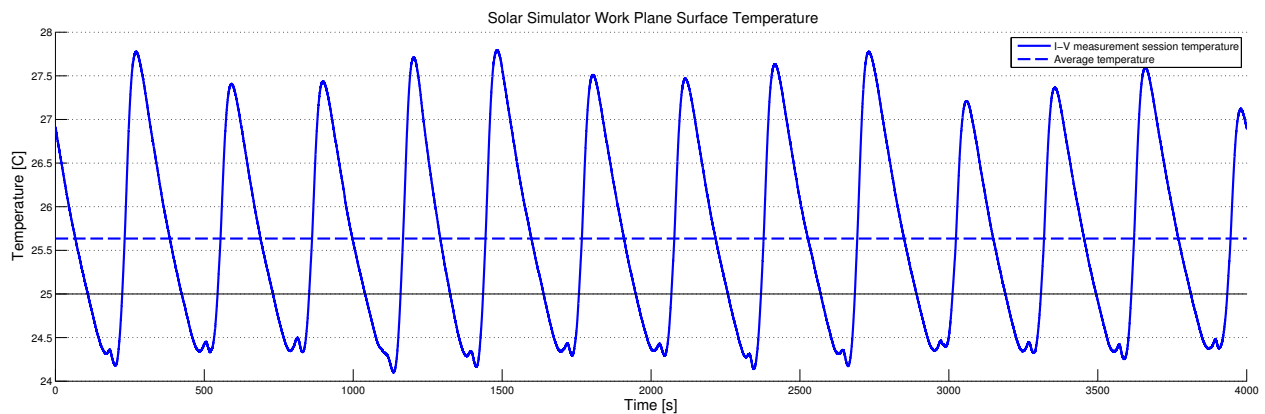


Figure 6.13: Solar simulator surface temperature from extended I-V measurement session.

ual and average results from the curve fitting are not much different from those of the average discrete numerical values. However, they offer values which are not strictly located along the sampling frequency of the sourcemeter, while still matching the numerical sample values to a high degree, and should as such be considered more representative.

## 6.2.1 Temperature Issue

Although one could wish for that the resolution of the I-V measurement simply was higher, the source of error which comes to mind in these measurements is another; the standard testing conditions specifically exclaims that measurements should be taken at a given temperature, here 25 °C.

As can be seen in Figure 6.13, the temperature of the solar simulator work plane during the experiment was not kept constant. Fluctuations in the surface temperature results from heat-

ing by the solar simulator illumination source. The temperature of the work plane surface is being monitored and compensated by the temperature controller which is adjusting the input control current to the cooling fan mounted under the measurement surface. This controller is programmed with a slightly too aggressive PI-controller behaviour, and this, combined with the fact that there is no derivative control enabled, makes the temperature loop produce standing oscillations.

The effect of a too high or too low temperature during I-V measurement is that certain measured characteristics of the solar cell will deviate from the results one would obtain during perfect STC conditions. Most important is the fact that the voltages of interest, $V_{oc}$ and $V_{mp}$ changes quite a bit with temperature.

The temperature fluctuated between 24.1 °C and 27.8 °C during the measurement, with an average temperature of 25.64 °C and frequency of about 3.25 mHz, or one complete wave cycle about every 5 minutes period. In addition, the temperature of the solar cell junction can be assumed to be slightly higher. A complete I-V measurement set with the settings used took approximately 1.5 minutes, and even if the measurement was started when the temperature was correct, the deviation would change throughout the measurement, with an opposite valued error rate depending on the rising or sinking state of the temperature. The main problem lies with the fact that if the measurement was started when the temperature gradient was positive, it could rise as much as 3 °C in less than one minute. Due to the fact that there were no previously recorded temperature logs available, the problem only became apparent after examining the data after the experiment.

When examining the measurement logs, the only timestamps available are $t_{T,start}$ and $t_{T,stop}$, the time of starting and stopping the temperature measurement respectively, and $t_{IV,finished}$ for when the I-V measurement log is created. We do know the supplied sampling frequency of the temperature controller, but for the I-V measurements, we only know the voltage resolution, which forces us to approximate the measurement time or sampling frequency. Knowing that one measurement set of $N_{IV} = 161$ samples took a duration in the vicinity of 1.5 minutes, it is not unreasonable to assume that the sampling frequency is $f_{IV} = 2/\text{sec}$, or a period of 0.5 s, which means that one full measurement range had a duration of 80.5 seconds.

The temperature log gives a start and stop timestamp, and the resulting duration which

Table 6.5: Timestamps collected from I-V measurement session.

| Measurement | Samp. period. | (Est.) $t_{start}$ | $t_{stop}$ | $\Delta t$ | $N_T$ | $n_{T,start}$ | $n_{T,stop}$ |
|---|---|---|---|---|---|---|---|
| Temperature | $f_T = 0.050\ s$ | 15:37:36 | 17:05:55 | 1:28:19 | 105694 | 0 | 105694 |
| I-V #1 | $f_{IV} = 0.5$ s | (16:32:03) | 16:33:23 | 0:01:20 | 1610 | 65340 | 66950 |
| I-V #2 | $f_{IV} = 0.5$ s | (16:35:27) | 16:36:47 | 0:01:20 | 1610 | 69420 | 71030 |
| I-V #3 | $f_{IV} = 0.5$ s | (16:37:15) | 16:38:35 | 0:01:20 | 1610 | 71580 | 73190 |
| I-V #4 | $f_{IV} = 0.5$ s | (16:39:58) | 16:41:18 | 0:01:20 | 1610 | 74840 | 76450 |
| I-V #5 | $f_{IV} = 0.5$ s | (16:41:50) | 16:43:10 | 0:01:20 | 1610 | 77080 | 78690 |

when combined with the stated sampling period of 0.05 s gives us the range of the total sample space

$$N_T = \frac{t_{T,stop} - t_{T,start}}{1/f_T} = \frac{5299 \pm 1}{0.05} = 105980 \pm 20 \tag{6.3}$$

where the fact that the sample resolution is higher than that of the timestamp in the log gives an inaccuracy of $\pm$ 20 samples. However, upon inspection of the log entries it is revealed that the actual total number of samples is $N_T = 105694$, a difference of of 286 samples of that expected by Equation 6.3. This can be interpreted as either a time difference of $(286 \pm 20) * 0.05 = 14.3 \pm 1$ seconds, or an average sampling period range of $f_T \in [50.126\ \text{ms} \leq \frac{(5299 \pm [0,1])}{105694} \leq 50.145\ \text{ms}]$. This inaccuracy adds to the already uncertain basis which the I-V temperature connection is built.

With the assumption of I-V measurement time and the gathered temporal information from the logs, we can attempt to reconstruct the timeline of the measurement session, and the relevant information can be seen in Table 6.5.

Using this data, we can attempt to investigate what kind of temperature the junction was exposed to during the measurement of the parts of the I-V curve which are used to extract the important characteristics. Figure 6.14 shows the extrapolated measurement durations on top of the temperature curve from the solar simulator work plane. It should be noted that due to the potential inaccuracy in synchronizing the log contents, the overlaying graph showing the work plane temperature during I-V acquisition should only be considered demonstrative towards the rapid change of temperature during measurement. The accompanying extrapolated temperature data for the characteristics are shown in Table 6.6, for completeness.

It can easily be seen upon inspection of the estimated temperature that the match between
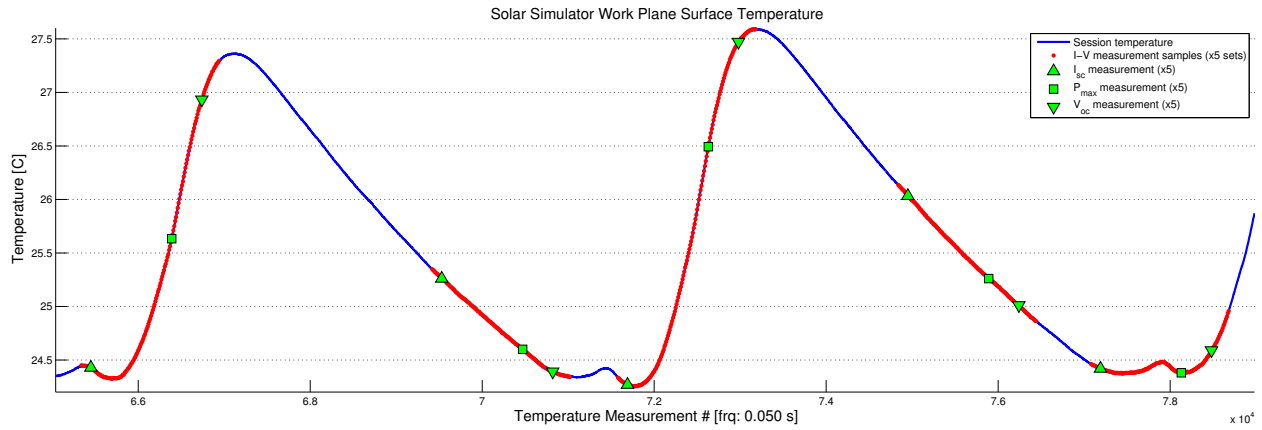
Figure 6.14: Solar simulator surface temperature during I-V measurement sets.

Table 6.6: Extrapolated temperature offset due to fluctuation during measurement.

| I-V Measurement # | Temperature offset (°C) | | |
| --- | --- | --- | --- |
| | $\Delta T_{Isc}$ | $\Delta T_{Voc}$ | $\Delta T_{Pmax}$ |
| 1 | -0.57 | +1.93 | +0.63 |
| 2 | +0.26 | -0.61 | -0.40 |
| 3 | -0.73 | +2.47 | +1.49 |
| 4 | +1.03 | -0.01 | +0.26 |
| 5 | -0.58 | -0.41 | -0.62 |

Table 6.7: Azurspace 3G30C solar cell temperature data (see complete data sheet in Appendix B).

| Temperature gradients | | | | | |
| --- | --- | --- | --- | --- | --- |
| | | | BOL | 5E14 | 1E15 |
| Open circuit voltage | $dV_{oc}/dT$ | (mV/°C) | -6.0 | -6.2 | -6.3 |
| Short circuit current | $dI_{sc}/dT$ | (mA/°C) | 0.32 | 0.31 | 0.39 |
| Voltage at maximum power | $dV_{mp}/dT$ | (mV/°C) | -6.1 | -6.3 | -6.4 |
| Current at maximum power | $dI_{mp}/dT$ | (mA/°C) | 0.28 | 0.20 | 0.29 |

expected values from temperature gradient compensation by Table 6.7, and the actual measured values is poor in our case. Although some might be attributed to error in the estimated duration of the I-V measurement, the overall misalignment in results are too big for this to be the main cause. This can however be due to the unknown mismatch between the temperature at the temperature sensor and the solar cell junction, or due to the attempted alignment of timestamps from the undocumented logging systems, which becomes a sensitive parameter when the temperature can vary greatly throughout a single measurement set. Or the difference in readings can come from a different source of error, such as the temporal stability of the illumination source. It can nevertheless not be recommended to use these values to compensate for a shift in temperature, and the average analytical values gathered from polynomial curve fitting of the discrete measured I-V pairs will be kept.

Although we have no direct credible causal connection between recorded temperature and measurements, it can be noted that the errors due to temperature fluctuation fits reasonably well within the span of our measurements. If the spread in results from the measured I-V sets is to be attributed to temperature, the comparison between minimum and maximum measured values for e.g. $V_{oc}$ in Table 6.4 suggests a fluctuation of about 1.5 °C at the five discrete sample points recorded for open circuit voltage, which is well within our overall temperature curve amplitude.

In hindsight, the temperature controller could have been investigated for possible optimization prior to the experiment. Eventually, the temperature and I-V measurement could have been actively synchronized, to allow for dynamical scaling of the measurements in accordance with the solar simulator temperature data.

The load behavior as well as the characteristic resistance can be seen in Figure 6.15.

## 6.3 Exploring the Simulator Behavior

### 6.3.1 Temperature Control

After learning that the temperature controller was configured with less than desireable parameters, it was decided to prioritize the tuning before initiating the next measurement. Rather than
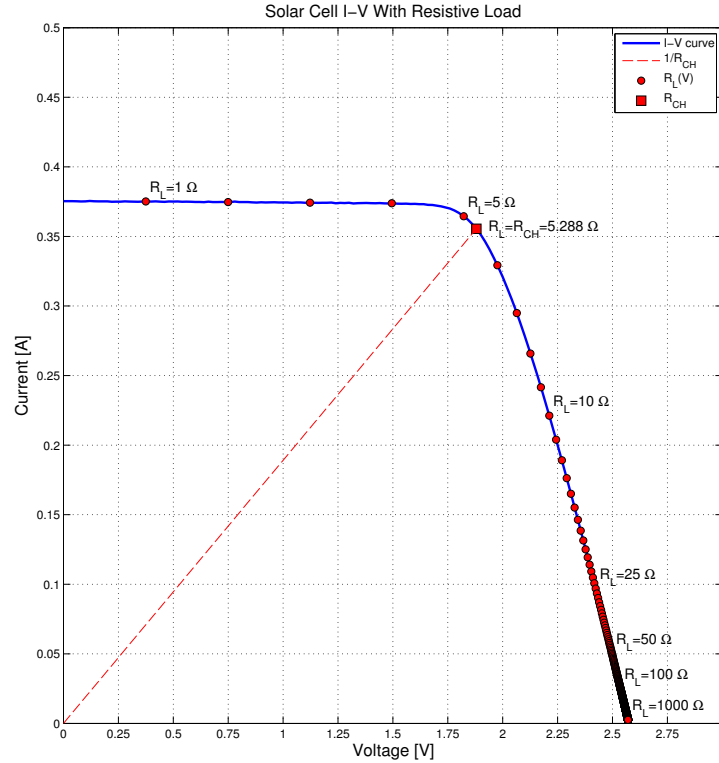
Figure 6.15: I-V curve with external load dependency and characteristic resistance.

leaving it running for the duration of the laboratory session, the log file from the temperature controller was explicitly split into segments where it felt natural, and the start and stop times of all measurements were recorded offhand. It was found that temperature controller parameters based on Ziegler-Nichols-inspired manual tuning for a PI-regultor yielded good behavior when bounding the integral gain. The effect of tuning the controller can be seen in Figure 6.16, showing the end of the temperature log with the old settings spliced in with the start of the log with the new parameters.

## 6.3.2 Spatial Uniformity

By use of the reference cell which is used to calibrate the arc lamp current to provide an irradiation of 1000 W/m$^2$, it was discovered that the spatial uniformity at the work plane features a hot-spot in the center, and slightly lower intensity in the surrounding areas. To counteract this, the arc lamp current was adjusted such that the average readout from the reference cell over the area spanned by the DUT in the work plane was close to the calibration voltage for 1 sun,
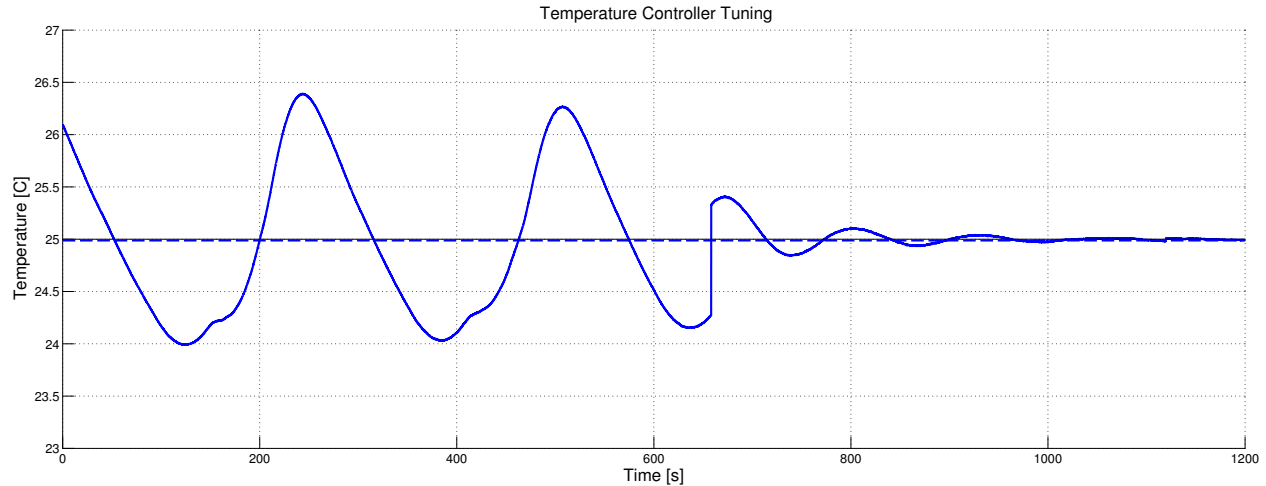
Figure 6.16: Temperature of work plane during 1 sun irradiation, before and after tuning. The skip in continuity at around t = 650 is due to stopping and restarting the temperature log when changing parameters.

87.3 mV, as stated on the reference cell and in the lab procedure document in Appendix C. The measurements can be seen illustrated in Figure 6.17, where the center horizontal row averages at 87.4 mV, while the average over all 9 squares is slightly lower, at 86.5 mV. However, the lowest contribution is from the upper corner measurements which span the least area of the DUT, making the effective average higher.

### 6.3.3 Irradiation and Armature Current

According to Equation 4.8, short circuit current should increase linearly with photogenerated current, given negligible parasitic resistances. Photogenerated current of high quality multi-junction cells should increase linearly with irradiation levels [72], and irradiation levels should increase linearly with armature current for xenon arc lamps in normal operating conditions. As a small test, the solar simulator armature current was adjusted in step-size intervals of 0.1-0.2 A, with single digit precision on the readout from the control panel. The values were decided to be kept reasonably close to default operation mode at 1 sun, despite the stated operating range of the bulb between 15.5 and 28 A [121], to not push too far outside normal operating conditions at a lab we've generously been granted access to. The results of adjusting the armature current, with respect to reference cell voltage and short circuit current measurements can be seen in Figure 6.18 and Figure 6.19, respectively. The is assumed that the change in spectral distribu-
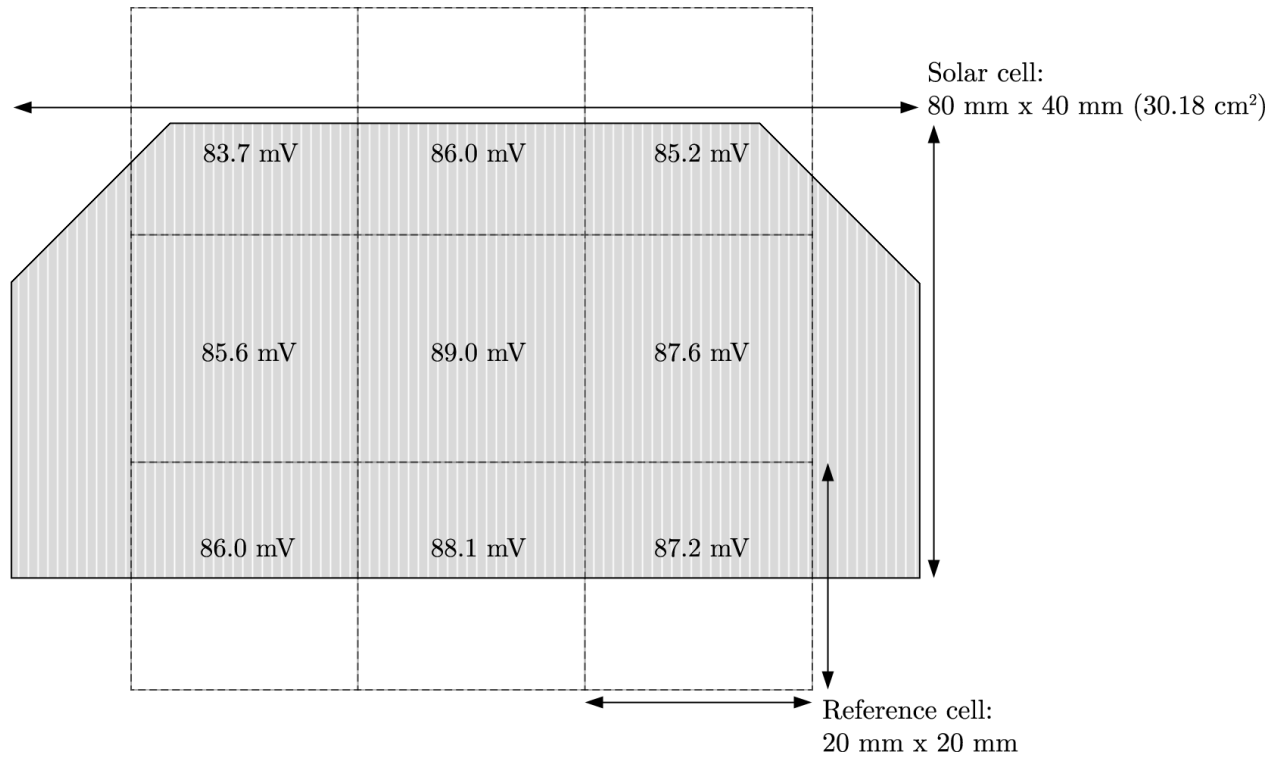
Figure 6.17: Work plane spatial uniformity levels at 2 cm × 2 cm resolution demonstrated by reference cell voltages. Solar simulator armature current at 21.8 A.

tion characteristics of the light source is negligible, and that the measurement values are due to change in intensity.

By utilizing the external spectral response to express the short circuit current for the cell, as defined in Equation 4.7, we can see that

$$I_{sc} = \int_\lambda SR_{\text{ext}}(\lambda) f(\lambda) \, \text{d}\lambda \tag{6.4}$$

Seeking the ratio between the short circuit current at AM0 and AM1.5 conditions, we can take inspiration in the methods employed by Japanese NASDA for AM0 solar cell calbrations [124], and formularize this as following
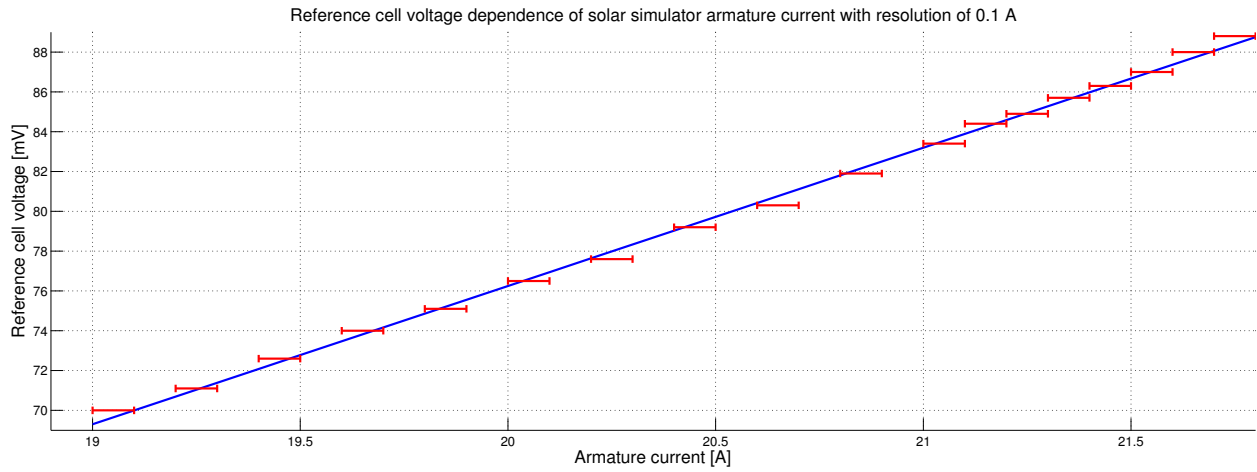
Figure 6.18: Reference cell voltage dependency on solar simulator armature current.
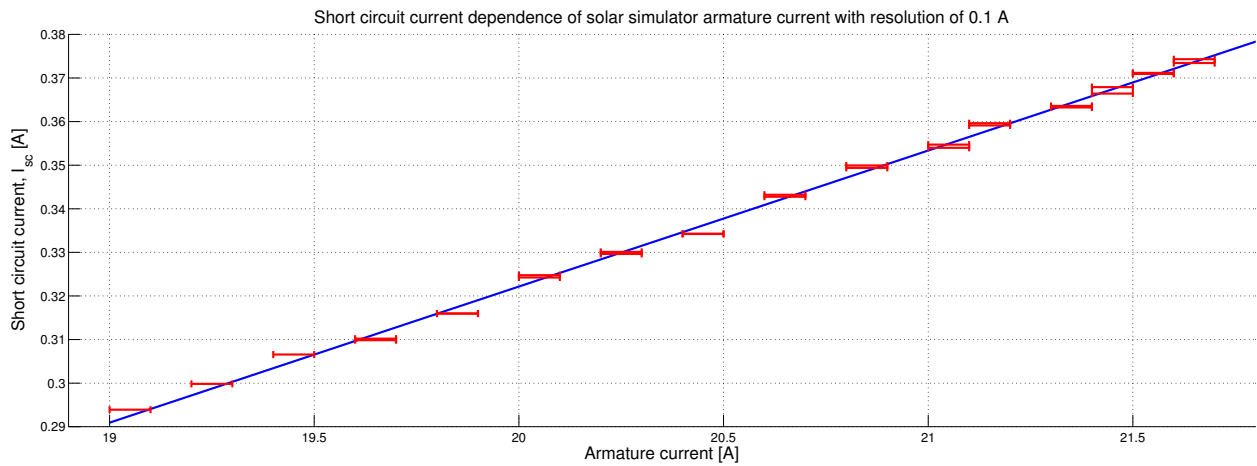


Figure 6.19: Short circuit current dependency on solar simulator armature current.

$$\frac{I_{sc}(\text{AM0})}{I_{sc}(\text{AM1.5G})} = \frac{\int_\lambda SR_{\text{ext}}(\lambda)\frac{E_{\text{AM0}}(\lambda)}{E_\lambda}\,\mathrm{d}\lambda}{\int_\lambda SR_{\text{ext}}(\lambda)\frac{E_{\text{AM1.5G}}(\lambda)}{E_\lambda}\,\mathrm{d}\lambda}$$

$$= \frac{SR_{\text{ext}}(x_{\lambda 1})\int_\lambda E_{\text{AM0}}(\lambda)\,\mathrm{d}\lambda}{SR_{\text{ext}}(x_{\lambda 2})\int_\lambda E_{\text{AM1.5G}}(\lambda)\,\mathrm{d}\lambda}$$

$$= \alpha\frac{1366.1\ \text{W/m}^2}{1000.4\ \text{W/m}^2} \tag{6.5}$$

where $\alpha = x_{\lambda 1}/x_{\lambda 2}$, and $x_\lambda$ is a result of applying the first mean value theorem for integration as we do not know the external (relative) spectral response for the cell. Measuring spectral response of multijunction cells is a nontrivial task which requires additional equipment, such as monochromators or narrow band filters and precise irradiance measurements [52]. However, if we make the bold assumption that the ratio is close to unity, we can approximate the short circuit current at AM0 irradiation conditions as

$$I_{sc}(\text{AM0}) = 1.366 I_{sc}(\text{AM1.5G}) \tag{6.6}$$

meaning that a measured short circuit current of 380 mA at AM1.5G conditions corresponds to an estimated value of 519 mA in AM0 conditions, which is not that far off the solar cell data sheet value of 525 mA. Note that this is *not* the same as doing measurements under AM0 STC, due to the different solar radiation spectra attributed to atmospheric effects. It can best be illustrated by comparing the spectra graphically, which can be seen in 6.20. Although the total spectral irradiance is the same magnitude, the irradiance within the bandgaps of the multijunction solar cell is not, and the solar cell will be operating at different efficiencies. It can, however, be considered as a guidance towards what can be expected in terms of short circuit current during AM0 operation. Provided that the linearity shown in Figure 6.19 extends, one would expect to produce an irradiance of 1367 W/m$^2$ at an armature current in excess of 26 A, which is outside the operational range of the light source.
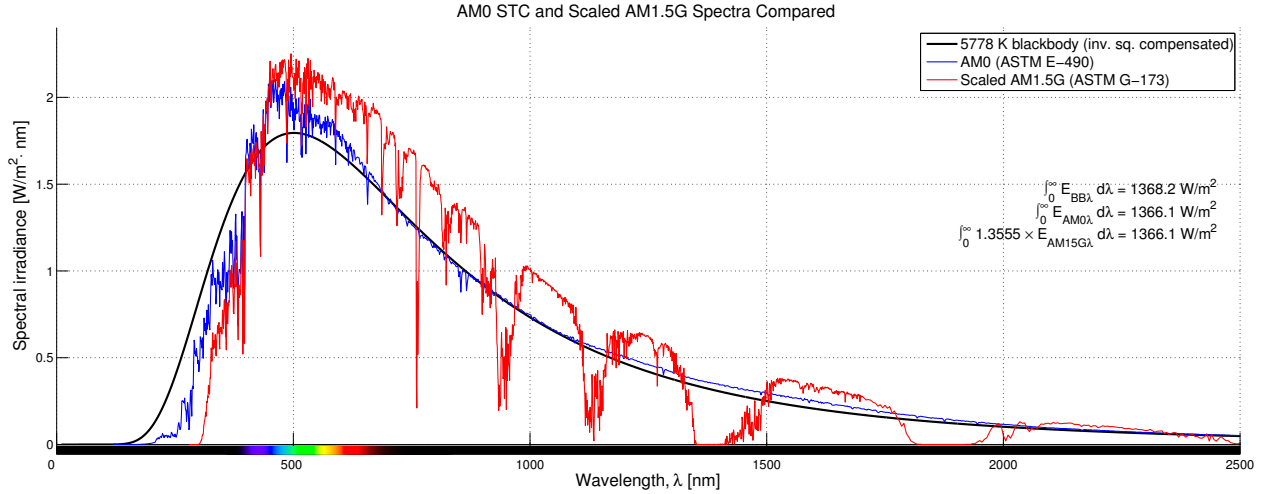
Figure 6.20: Comparison between AM0 STC spectrum and AM1.5G scaled spectrum.

## 6.4 Irradiation at Non-Normal Angle of Incidence

### 6.4.1 First Iteration

Prior to the measurements done in this session, a whole set of measurements done at refined temperature control and spatial uniformity compensation were discarded due to fluctuations in the transient phase of the I-V curve. It is believed to be the result of poor connection between the solar cell terminal and probe(s). The probes were switched out for a suitable cable with ends soldered to proper connectors, which eliminated the problem.

Given the fact that the short circuit current scales linearly with the irradiance of the solar cell, one would expect the output to be cosine related with respect to the angle of incidence similar to to as stated in Equation 3.17;

$$I_{sc}(\theta) = I_{max}\cos(\theta) \tag{6.7}$$

where $I_{max} = I_{sc}(\theta = 0)$. However we also know that surfaces do not transmit light from all angles indiscriminately, and Snell's law

$$\frac{\sin\theta_i}{\sin\theta_t} = \frac{n_2}{n_1} \tag{6.8}$$

combined with the Fresnel equations describing the reflectance for s-polarized and p-polarized

light

$$R_s = \left| \frac{n_1 \cos\theta_i - n_2 \cos\theta_t}{n_1 \cos\theta_i + n_2 \cos\theta_t} \right|^2 \qquad (6.9)$$

$$R_p = \left| \frac{n_1 \cos\theta_t - n_2 \cos\theta_i}{n_1 \cos\theta_t + n_2 \cos\theta_i} \right|^2 \qquad (6.10)$$

becomes

$$R_s = \left| \frac{n_1 \cos\theta_i - n_2 \sqrt{1 - (\frac{n1}{n2} \sin\theta_i)^2}}{n_1 \cos\theta_i + n_2 \sqrt{1 - (\frac{n1}{n2} \sin\theta_i)^2}} \right|^2 \qquad (6.11)$$

$$R_p = \left| \frac{n_1 \sqrt{1 - (\frac{n1}{n2} \sin\theta_i)^2} - n_2 \cos\theta_i}{n_1 \sqrt{1 - (\frac{n1}{n2} \sin\theta_i)^2} + n_2 \cos\theta_i} \right|^2 \qquad (6.12)$$

where $\theta_i$ and $\theta_t$ are the angles of incidence and transmittance, and $n_1$ and $n_2$ are the refractive indices of the first and second medium which the light travels through, respectively. Under the assumption that the irradiation from the end of the solar simulator optical train contains equal parts of s-polarized and p-polarized light, i.e. is unpolarized, like true unfiltered sunlight, the reflection coefficient becomes

$$R = \frac{R_s + R_p}{2} \qquad (6.13)$$

The dependency of reflectance as a function of angle of incidence can be seen depicted in Figure 6.21, which illustrates the s-polarized and p-polarized components of unpolarized light going from an air-like medium with refractive index $n_1 = 1$ into a medium of refractive index $n_2 = 1.5$. Similarly, reflectance of unpolarized light for different values of $n_2$ can be seen in 6.22.

For measuring the solar cell output at different angles of incidence with the light from the solar simulator, the optimal scenario would allow for the use of something which can create precisely adjustable angles. Whether by meticulous adjustment by hand, or by automated means like closed-loop servos or an appropriate stepper motor, it should still be able to keep the DUT temperature close to the temperature reference set in the temperature controller. This is diffi-
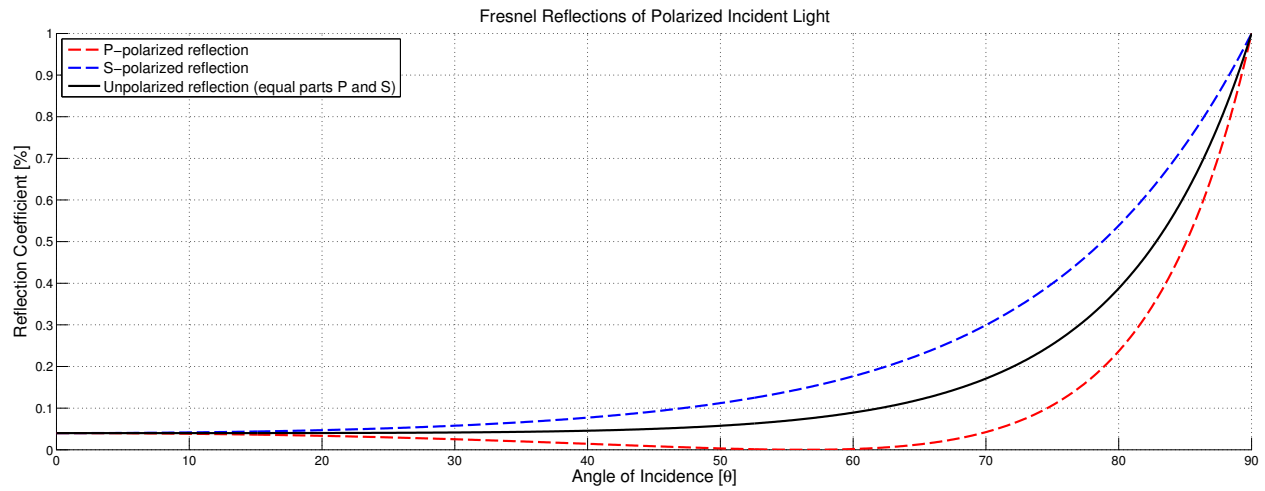
Figure 6.21:  Polarized Fresnel reflectivity as a function of angle of incidence $\theta$, for refractive indices $n_1 = 1$ and $n_2 = 1.5$.
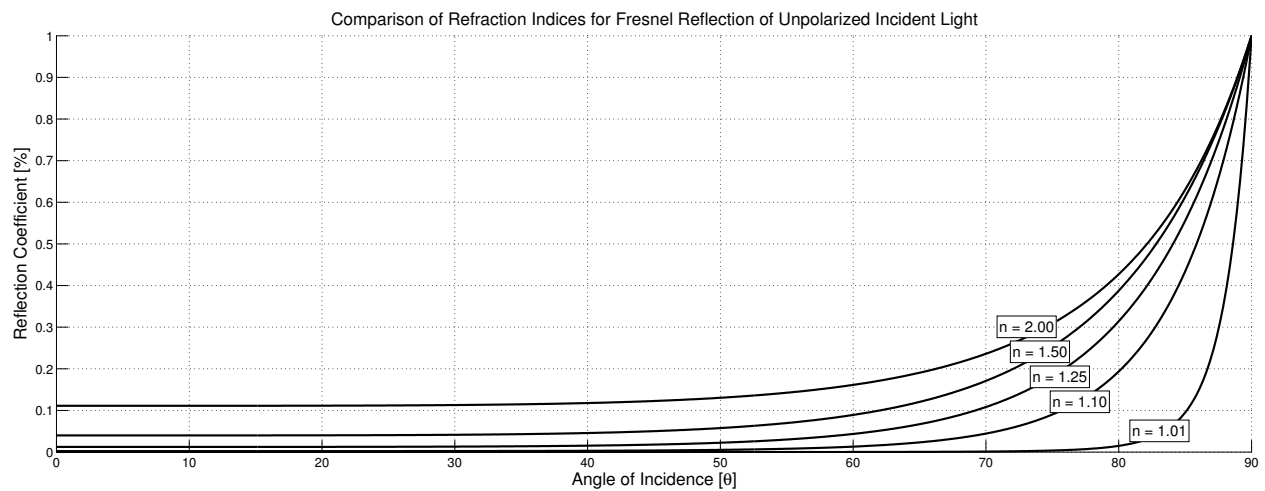


Figure 6.22: Unpolarized Fresnel reflectivity as a function of angle of incidence $\theta$, for $n_1 = 1$ and different values of $n_2$.
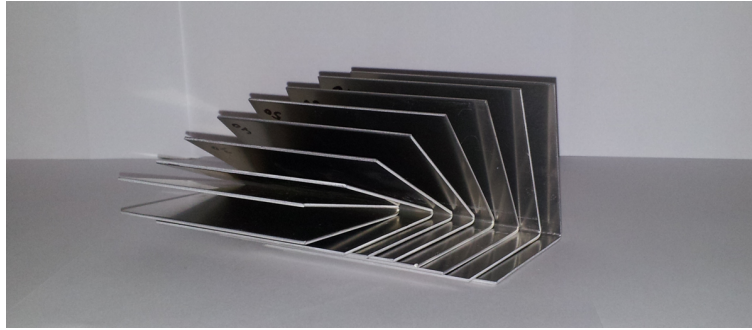
Figure 6.23: Photo of the mounting angles used for measuring at non-normal angles inside the solar simulator.

cult in our case because of the solar simulators design to irradiate a short distance away from the collimator lens, normal to the relatively small work plane which contains the temperature control loop that applies cooling of the DUT by mechanical contact with the work plane. Rotating the entire work plane at anything but miniscule angles is not an option, due to its awkward size and position under the simulator. It was deemed that mechanical contact should be kept with the work plane, as design of exterior temperature sensing and cooling seemed a bit excessive. Thus a range of different angles for mounting the solar cell on the work plane was created at the mechanical workshop at the Insitute of Engineering Cybernetics, and can be seen in Figure 6.23. They are crafted from aluminum sheets of thickness 1mm, with dimensions measuring about $100 \times 140$ mm, and is precisely bent in the middle in increments of $10°$, from $10°$ to $80°$ respectively, such that it leaves an two areas of about $100 \times 70$ mm; one for resting flat on the work plane to keep thermal contact and one for mounting the solar cell board. Aluminum was chosen in the absence of copper, due to its good thermal conductivity and immediate availability. An additional wegde was created to increase the angles available for sampling, by the possiblity of adding $6°$ to every mounting angle. With careful mounting, it is assumed that the cumulative angular errors resulting from (1) solar cell onto of circuit board, (2) circuit board onto aluminum angle, (3) aluminum angle onto wedge, and (4) wedge and mounting angle onto work plane should be within $\pm1°$, depending on the direction that the solar cell is mounted due to some slightly protruding terminal pins on the backside of the circuit board. The solar cell during measurement can be seen in Fig 6.24

A few full I-V measurement sets were taken for all the mounting angles, and the average result per angle can be seen in Fig 6.25. This figure also illustrates that the thermal transfer of the
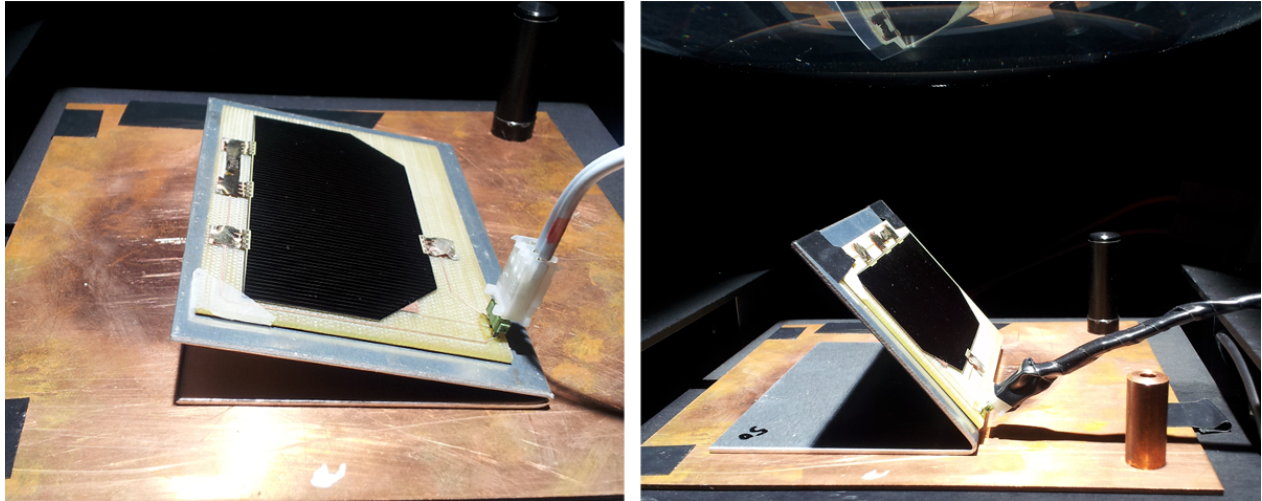
Figure 6.24: Photos of the mounted solar cell during measurement.

aluminum mounting angles is less than ideal, by warping the I-V curves along the voltage axis such that some of the curves overlap in the transient phase near the "knee" of the curve, and display a lower open circuit voltage than expected. This can be explained by the temperature gradient found in Table 6.7 or Appendix B. By inspection of the $V_{oc}$ values, it is apparent that the temperature of the DUT during most of the measurements was about 5°C higher than that recorded in the work plane. This can be attributed to the fact that due to the angle with the work plane, the solar cell is a good bit closer to the illumination source/condenser lens, as well as the obvious limited heat transfer from the raised limb of the mounting angle to that which is in contact with the work plane.

With higher mounting angles, it also became a challenge to keep good contact with the back-side connector of the solar cell, as the cell is kept in place only by the Ag contact with minimal solder. A small piece of transparent tape had to be put over one of the corners of the cell to keep it secured in place and ensure contact. Especially at the measurement at 86° angle, where some samples dropped due to connectivity problems, as is visible in the figure even after averages have been taken. Additionally, the stiffness and size of the cable connected to the cell's 3-pin connector made it challenging to position perfectly on the work plane.

The results in relation to short circuit current can be seen in Figure 6.26, and summarized in Tables 6.8 and 6.9, which shows the comparison between measured values and expected values from a purely cosine relation, and a reflectivity compensated cosine relation, respectively. The
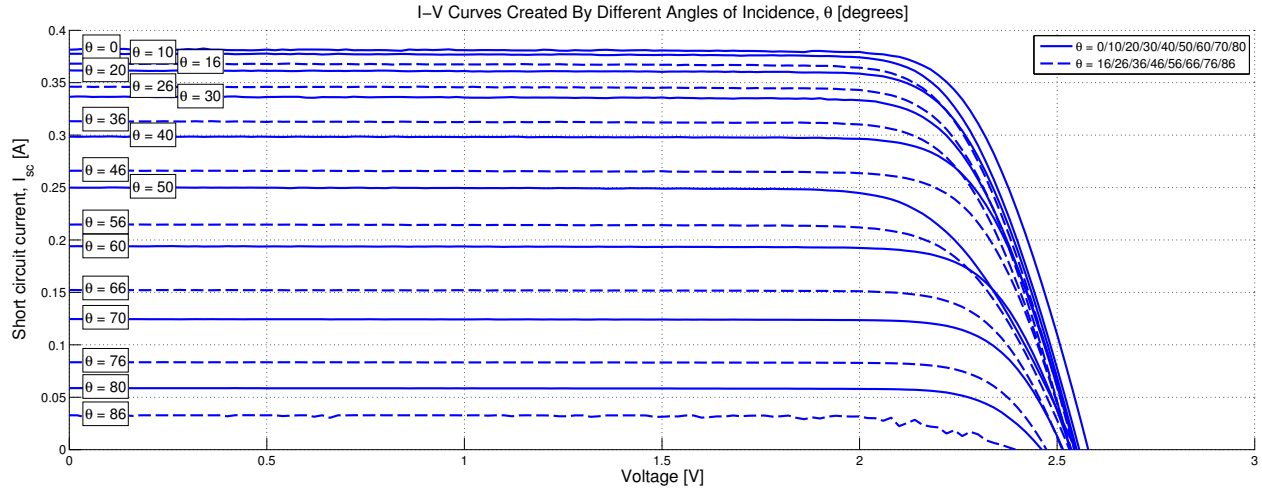
Figure 6.25: I-V measurements at different angles of incidence $\theta$.

solar cell reflectivity was modeled after typical values of 0.10 mm CMX/CMG coverglass [125], with an estimated refractive index of 1.52, with no further transmission loss related to the angle of incidence after the initial reflection.

It can be seen that the short circuit current follows the curve reasonably well, more so the pure cosine relation than when taking reflectivity into account, in fact. There are however some error sources that needs to be pointed out.

(1) According to the temperature gradient for the solar cell, the mentioned increased measurement temperature generally accounts for a few mA extra in the short circuit current measurements, depending on how much excess temperature the DUT experienced at the time of measurement. (2) In addition, as the mounting angles becomes bigger, the projected area of the solar cell into the work plane also becomes correspondingly smaller. This is a problem because of the spatial uniformity of the light distribution, which is not perfect. Close to the center axii of the work plane where the solar cell is centered, the irradiation is higher, meaning that the average intensity of the light falling normal to the projected area of the cell is increasing with the measurement angles. (3) Yet another problem is the error source of the reflective copper work plane, which also becomes ever more present at increasing angles. This could, however, be remedied by fitting the work plane with a less reflective material, but in doing so one would also interfer with the temperature control of the work plane unless the material have similar thermal conduction properties. It can indeed be questioned whether or not one should have
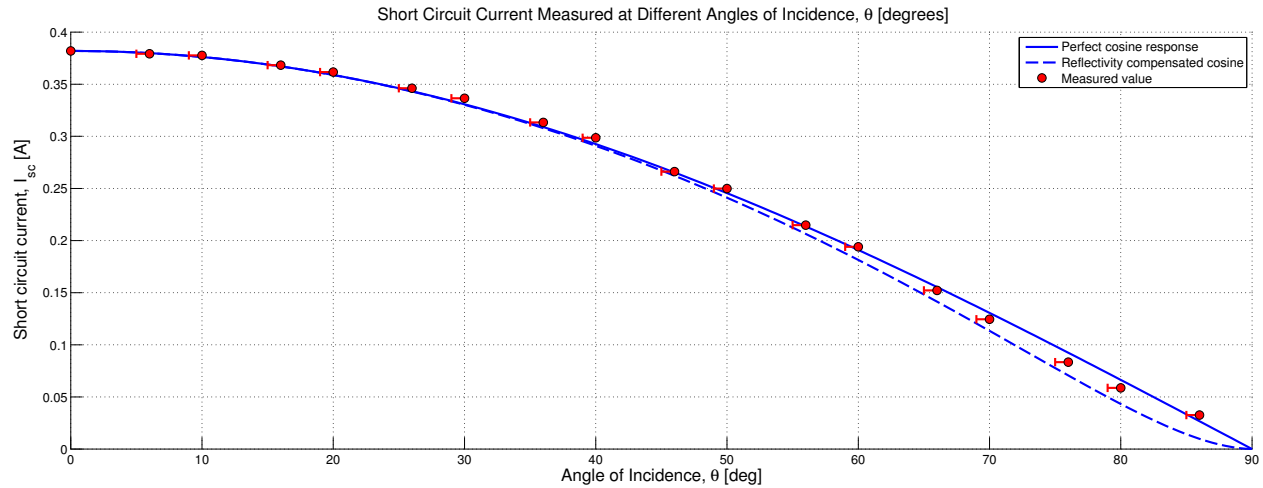
Figure 6.26: Short circuit current $I_{sc}$ measured at different angles of incidence $\theta$. Error bars of $1°$ represents initial uncertainty associated with solar cell mounting on angle.

forfeited the temperature control altogether in favor of a more flexible environment.

All in all, it should be assumed that the measured values are biased towards a too high value, with the magnitude of error generally increasing with an increasing measurement angle.

## 6.4.2   Second Iteration

With some lessons learned in hand, another set of measurements were performed under slightly different conditions;

- The copper surface which is responsible for keeping a flat, temperature controlled work plane was assumed to contribute increasing disturbance to the measurements at increasing angles. This surface was replaced with a low reflectivity surface created from a matte black cardboard piece dressed in matte black fabric, and the comparison between the two can be seen in Figure 6.27.

- Temperature control was forfeited due to the practically eliminated thermal coupling between the temperature sensor and the DUT from the replacement work plane surface. In order to keep track of the conditions, off-hand temperature measurements of the DUT were done prior to, and after every I-V measurement. Measuring the device temperature under testing is of limited use with the available equipment, as the temperature probe

Table 6.8: Comparison between measured and expected pure cosine $I_{sc}$ values for different angles of incidence $\theta$.

| $\theta$ [deg] | Expected $I_{sc}$ [mA] | Measured $I_{sc}$ [mA] | $I_{sc}$ error [mA] | Calculated $\theta$ [deg] | $\theta$ error [deg] |
|---|---|---|---|---|---|
| 0 | - | 381.9 | - | - | - |
| 6 | 379.8 | 379.2 | -0.6 | 6.82 | 0.82 |
| 10 | 376.1 | 377.6 | 1.6 | 8.56 | -1.44 |
| 16 | 367.1 | 368.2 | 1.1 | 15.37 | -0.63 |
| 20 | 358.9 | 361.6 | 2.7 | 18.76 | -1.24 |
| 26 | 343.2 | 346.1 | 2.9 | 24.99 | -1.01 |
| 30 | 330.7 | 336.5 | 5.8 | 28.22 | -1.78 |
| 36 | 309.0 | 313.3 | 4.3 | 34.88 | -1.12 |
| 40 | 292.6 | 298.6 | 6.1 | 38.56 | -1.44 |
| 46 | 265.3 | 266.1 | 0.8 | 45.83 | -0.17 |
| 50 | 245.5 | 249.9 | 4.4 | 49.13 | -0.87 |
| 56 | 213.6 | 214.8 | 1.2 | 55.78 | -0.22 |
| 60 | 191.0 | 194.0 | 3.1 | 59.47 | -0.53 |
| 66 | 155.3 | 152.2 | -3.1 | 66.51 | 0.51 |
| 70 | 130.6 | 124.5 | -6.1 | 70.97 | 0.97 |
| 76 | 92.4 | 83.4 | -9.0 | 77.39 | 1.39 |
| 80 | 66.3 | 58.7 | -7.6 | 81.16 | 1.16 |
| 86 | 26.6 | 32.6 | 5.9 | 85.11 | -0.89 |

can not be installed directly on the cell surface. Measurements were done on the backside connector, and one should be aware that there is a temperature gradient between the cell and the probe [126].

- Instead of creating entire I-V curves which takes considerable time, measurements were kept very short by only sampling around zero volts, to retrieve the short circuit current values. By only taking 21 samples ($\Delta V = 0.01$, $V \, \epsilon \, \pm 0.1$ V) in order to create a reasonable window for taking averages, the measurements are kept short, and the temperature increase is limited by reducing exposure to the solar simulator illumination. Items left on the thermally unregulated work plane would quickly develop temperatures in excess of 40 °C.

- Rather than keeping every aluminum mounting angle exposed to the solar simulator output for the entirety of measurements done with the angle, measurements were done in the sense of round-robin scheduling to allow the materials to return to a state near room temperature between utilizations.

Table 6.9: Comparison between measured and expected reflectivity compensated cosine $I_{sc}$ values for different angles of incidence $\theta$.

| $\theta$ [deg] | Expected $I_{sc}$ [mA] | Measured $I_{sc}$ [mA] | $I_{sc}$ error [mA] | Calculated $\theta$ [deg] | $\theta$ error [deg] |
|---|---|---|---|---|---|
| 0 | - | 381.9 | - | - | - |
| 6 | 379.8 | 379.2 | -0.6 | 6.82 | 0.82 |
| 10 | 376.1 | 377.6 | 1.6 | 8.55 | -1.45 |
| 16 | 367.1 | 368.2 | 1.2 | 15.35 | -0.65 |
| 20 | 358.8 | 361.6 | 2.8 | 18.37 | -1.63 |
| 26 | 343.0 | 346.1 | 3.2 | 24.91 | -1.09 |
| 30 | 330.2 | 336.5 | 6.3 | 28.06 | -1.94 |
| 36 | 307.9 | 313.3 | 5.4 | 34.63 | -1.37 |
| 40 | 290.8 | 298.6 | 7.8 | 38.22 | -1.78 |
| 46 | 262.2 | 266.1 | 3.9 | 45.22 | -0.78 |
| 50 | 241.1 | 249.9 | 8.8 | 48.36 | -1.64 |
| 56 | 206.4 | 214.8 | 8.4 | 54.61 | -1.39 |
| 60 | 181.4 | 194.0 | 12.6 | 58.01 | -1.99 |
| 66 | 141.4 | 152.2 | 10.8 | 64.42 | -1.58 |
| 70 | 113.4 | 124.5 | 11.1 | 68.42 | -1.58 |
| 76 | 70.6 | 83.4 | 12.8 | 74.2 | -1.8 |
| 80 | 43.2 | 58.7 | 15.5 | 77.71 | -2.29 |
| 86 | 9.8 | 32.6 | 22.8 | 81.68 | -4.32 |

As can be seen from Figure 6.28 and the results summarized in Table 6.10, the measurements for high-angle incidence matches much more closely to that expected by a Fresnel reflection-compensated cosine response. The general measurement curve is otherwise largely unchanged, with results consistenly slightly higher than expected yet with smaller deviance than previously recorded. The temperature prior to, and after these short measurements were consistenly slightly higher than STC, at generally 26-27 °C before solar simulator exposure, and about 32 °C after measurements when keeping the exposure duration short and approximately the same for all measurements. It is assumed that the average temperature over the course of three short consecutive at every angle should render the temperature difference between each measurement negligible and about 30 °C. Without in situ temperature measurements, any temperature gradient correction between the measurements will have an element of guessing.

Comparisons of the deviances between measured $I_{sc}$ and $\theta$ can be seen in Figures 6.29 and 6.30, which show the error expressed in short circuit current and calculated angle of incidence, respectively. It can be noted that the general form of the curve for the first measurement session

Figure 6.27: Photos showing the replacement work plane surface with lower reflectivity.
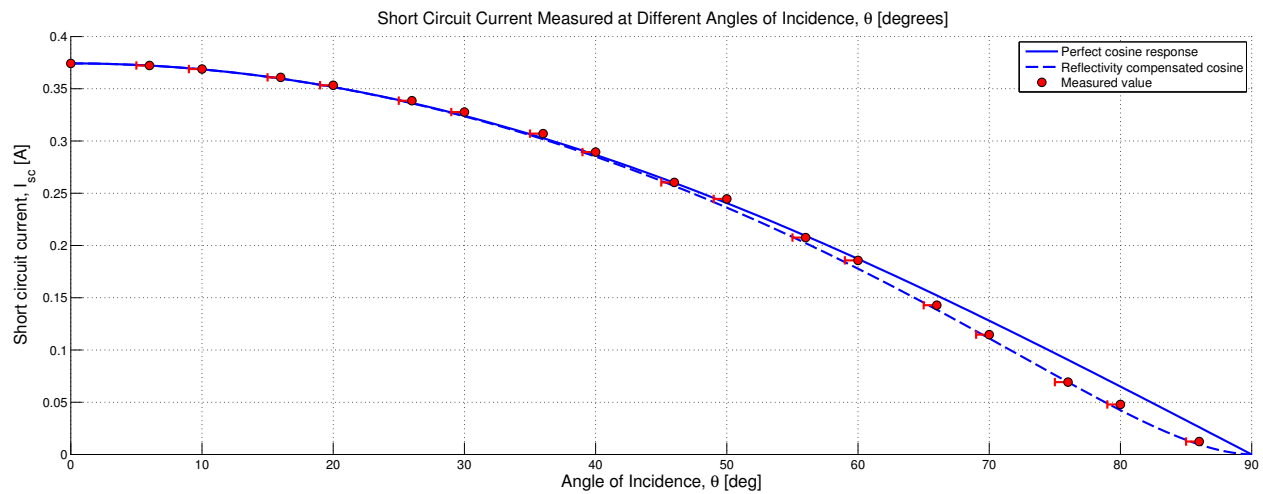


Figure 6.28: Short circuit current $I_{sc}$ measured at different angles of incidence $\theta$, after high-angle disturbances have been reduced. Error bars of $1°$ represents initial uncertainty associated with solar cell mounting on angle.

Table 6.10: Comparison between measured and expected reflectivity compensated cosine $I_{sc}$ values for different angles of incidence $\theta$, after high-angle disturbances have been reduced.

| $\theta$ [deg] | Expected $I_{sc}$ [mA] | Measured $I_{sc}$ [mA] | $I_{sc}$ error [mA] | Calculated $\theta$ [deg] | $\theta$ error [deg] |
|---|---|---|---|---|---|
| 0 | - | 374.2 | - | - | - |
| 6 | 372.2 | 372.3 | 0.1 | 5.87 | -0.13 |
| 10 | 368.6 | 368.9 | 0.4 | 9.68 | -0.32 |
| 16 | 359.7 | 360.9 | 1.2 | 15.33 | -0.67 |
| 20 | 351.6 | 353.4 | 1.8 | 19.18 | -0.82 |
| 26 | 336.1 | 338.6 | 2.5 | 25.12 | -0.88 |
| 30 | 323.6 | 327.7 | 4.1 | 28.74 | -1.26 |
| 36 | 301.7 | 307.0 | 5.4 | 34.62 | -1.38 |
| 40 | 285.0 | 289.4 | 4.4 | 38.98 | -1.02 |
| 46 | 256.9 | 260.4 | 3.4 | 45.31 | -0.69 |
| 50 | 236.2 | 244.6 | 8.4 | 48.42 | -1.58 |
| 56 | 202.3 | 207.6 | 5.3 | 55.10 | -0.90 |
| 60 | 177.8 | 185.7 | 7.9 | 58.73 | -1.27 |
| 66 | 138.6 | 142.8 | 4.3 | 65.36 | -0.64 |
| 70 | 111.1 | 114.7 | 3.6 | 69.48 | -0.52 |
| 76 | 69.2 | 69.3 | 0.1 | 75.99 | -0.01 |
| 80 | 42.3 | 47.8 | 5.5 | 79.15 | -0.85 |
| 86 | 9.6 | 12.4 | 2.8 | 85.35 | -0.65 |

corresponds to the expected effect of the error sources mentioned, with a generally increasing error with increasing angle of incidence.

It is also worth mentioning that replacement of the reflective copper surface work plane reduced the overall work plane intensity in the form of about 5 mA worth of photogenerated current at normal incidence, believed to be credited by the reflections from the work plane to the collimating lens and back down again. This has no influence on the validity of the angular dependency however, as the conditions were kept constant throughout the entire session.

At this point, the immediate possibilities of improving the current testing conditions seem to be exhausted without initiating steps toward providing alternate means of DUT temperature control and stepless angular positioning.
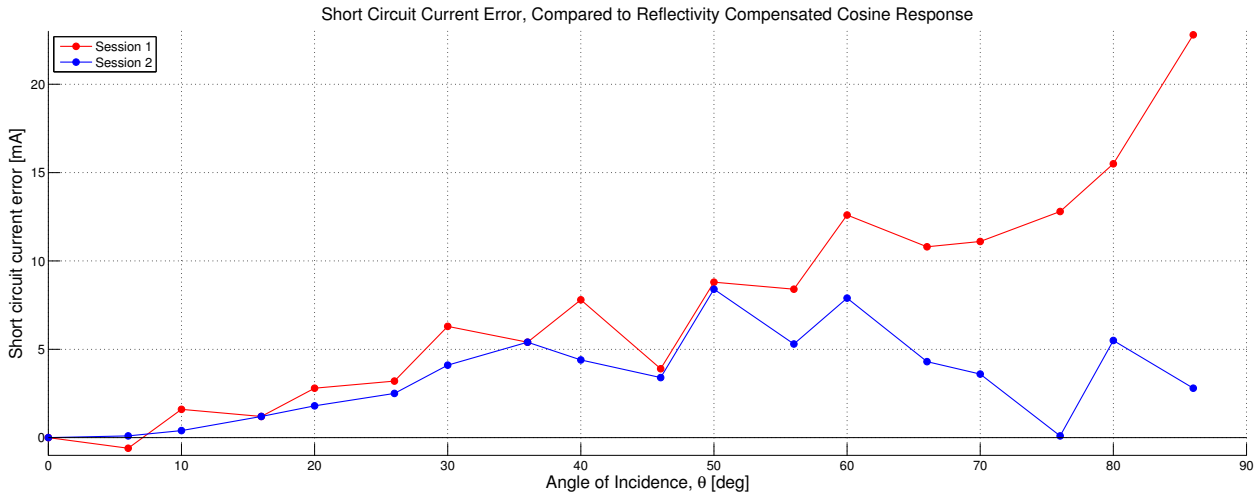
Figure 6.29: Deviance between expected and measured short circuit current values during first and second session of measurements, when compared to a reflectivity compensated cosine response.
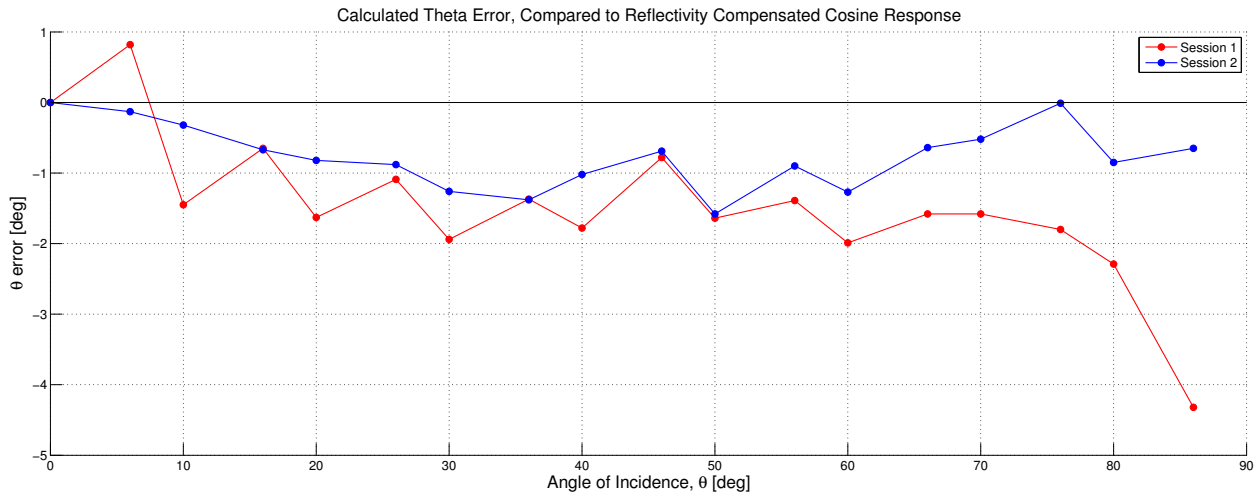


Figure 6.30: Deviance between known and calculated angle of incidence values during first and second session of measurements, when compared to a reflectivity compensated cosine response.

# Chapter 7

# Summary and Recommendations for Further Work

## 7.1 Summary and Conclusions

The relevant energy theory behind intensity and spectral irradiance from the sun have been discussed with regard to how it changes due to factors like Earth-Sun distance, solid angle of the sun disk and circumsolar region, angle of incidence and atmospheric mass. This translates to how the experienced conditions for solar cells vary, how and why solar simulation is done the way it is with such stringent requirements, as well as what can be expected in terms of difference between controlled, fixed conditions and operation in environments where we are not free to modify the variables as easily.

The depth and breadth of the underlying physics of the solar cell is however a challenging topic to cover and could never be done proper justice, as stacks of books and research papers are needed to properly cover the ever expanding field of photovoltaics. The most essential theory of solar cell structure and performance have however been reviewed, with emphasis on the theory needed to understand the design principles, characteristics and behavior of the high-efficiency multijunction solar cells available for the NUTS project.

The most commonly encountered components of a solar simulator have been discussed to

Table 7.1: Summarized I-V parameters measured at AM1.5G STC (from Table 6.4)

|  | $I_{sc}$ [A] | $V_{oc}$ [V] | $I_{mp}$ [A] | $V_{mp}$ [V] | $P_{max}$ [W] |
|---|---|---|---|---|---|
| Average | 0.3753 | 2.5745 | 0.3567 | 1.8728 | 0.6681 |

the point where the information provided should allow for a well-informed evaluation and selection of design for most applications, and be of guidance if one were to wish to attempt to create a device able to simulate aspects of the solar irradiation. It should be pointed out that a directed light source is by definition *not* the same as a solar simulator due to the strict classifications and requirements as discussed. However depending on the application, a less refined contraption than a full-blown solar simulator at STC might provide adequate, yet likely less detailed, results. The solar simulation test setup at the optical calibration lab was also properly documented, to give insight to the quality of the environment that the measurements were carried out in.

By being fortunate enough to gain access to the optical calibration lab at the Department of Physics means that the NUTS project have been able to perform solar cell measurements under standardized testing conditions. I-V characteristics was developed for the solar cell by probe measurements as well as by circuit board connectors, and the influence of concepts like temperature dependency was experienced in practice. The experiments that were performed also underlines the importance of ensuring proper knowledge about simulator behavior, e.g. with regards to xenon lamp intensity control by armature current and spatial uniformity in the work plane.

The initial I-V characteristic measurements were performed with solar simulator armature current such that the reference cell showed irradiance of precisely 1 sun (1000 W/m$^2$) in the middle of the work plane, and a set of 5 measurements with curve fitting in the $P_{max}$ region yielded the average results seen in Table 7.1.

Upon proceeding with further measurements, probes were switched for cables with appropriate connectors soldered to the ends, work plane temperature control was further stabilized and armature current was increased by 0.1-0.2 A to compensate for a hotspot in the center of the

work plane which resulted in the overall illumination of the solar cell being slightly too low. The resulting short circuit current at normal incidence showed an increase of about 8 mA, or 1.8%.

Measurements were then taken of the solar cell mounted at 18 different discrete aluminum angles ranging from 0° to 86°, in two separate sessions. The first session yielded results which were acceptable, but showed signs of disturbances which seemed possible to reduce. The second measurement session was performed after processing the data from the first session and a slight tweaking of the work plane environment and measurement settings; in few words: less disturbing specular reflectance, shorter sampling intervals, and general lack of active temperature control. The resulting short circuit current measurement values can be seen in 6.10, compared with an estimated cover glass reflectivity compensated cosine relation. As can be seen in Figure 6.30, the incidence angles calculated from the measured short circuit currents showed a deviance generally smaller than 1°, which is promising results.

## 7.2   Discussion

We were lucky enough to be able to perform measurements with qualified hardware at standard testing conditions, albeit air mass 1.5 at 1 sun intensity, or 1000 W/m$^2$, when the optimal circumstances would allow us to perform tests at AM0 conditions. As can be expected due to the difference in standard testing conditions, the values measured at the optical calibration lab are not directly comparable with the data sheet provided by the solar cell manufacturer. The values seem to scale reasonably though, when we consider that the open circuit voltage of the cell does not change much with intensity conditions (logarithmically), and the fact that the short circuit current is linearly related to the irradiation of the solar cell lets us *estimate* the short circuit current at AM0 conditions to be 509-520 mA, depending on which measurement is used. The data sheet states a short circuit current of 525 mA, which is not that far off, and might actually be in the correct range if the data sheet is indeed values measured without coverglass, as the cells were at some point sent to Astrium for mounting and coating.

The measurements done in the lab, are exactly what they seem - *lab results.* The expected scaling of the short circuit current with angle of incidence follows the curve nicely, but these

expected values are based upon a known, normal incidence irradiation result. In order to avoid a bias to the curve when measuring a source, the maximum value needs to be known firmly beforehand. In practice this means that for AM0 conditions, the cell needs to be AM0 characterized - which the NUTS solar cells are, in form of the data characteristics provided by the manufacturer, Azurspace. Alternatively, the spectral response of the cell need to be carefully measured, such that the cell's behavior can be appropriately scaled. Nevertheless, as mentioned in the section about the energy of sunlight, even the irradiation conditions just outside the atmosphere are not constant, and are expected to vary roughly 7% from the Earth orbit alone. Depending on the method chosen to generate a sun vector, this will have a form of impact; if geometrical relations are used to cancel out maximum current value dependency by assuming identical cells, this impact will be smaller than if every cell is evaluated individually. The discussion regarding this borderlines with the ambition of this thesis, and interested readers should refer to the author's previous project work [1, 2] instead.

The temperature fluctuations during the first batch of I-V measurements are, even though not ideal, not very detrimental to the variable of interest, the short circuit current. A temperature change of 3°C is responsible for only a change of 1 mA in the current. This is also the reason why active temperature control was discarded throughout measurements of irradiance at non-normal incidence with the aluminum mounting angles. Part of the reasoning behind making one-piece angles was to keep good thermal contact, but as the voltage values in the first I-V measurements at non-normal incidence reveal, the effect on temperature of the DUT by the temperature control loop was rather limited. At high mounting angles, the cumulative error sources from high temperature, higher light intensity along the center axis of the work plane spread over a smaller projected solar cell area, and the reflective copper work plane surface - all of which contribute to an increased short circuit current - are believed to initially have biased the first set of angled measurements higher than they should be.

Finally, literature references state that steady-state solar simulation I-V acquisition usually does not take as long as what was experienced in the lab. The long sampling duration of the measurements can possibly be attributed to the author being an inexperienced operator show-

ing too much respect for the equipment to step outside his training, the software design for acquiring the measurements, or both. It should however be pointed out that it is desireable to keep the exposure time limited, with work plane temperature, stability of the simulator output and light source lamp life in mind.

## 7.3   Recommendations for Further Work

Any algorithm chosen to produce the sun vector by utilizing measurements from the behavior of individual solar cells needs to be adjusted for temperature, as temperature in low Earth orbit will vary considerably depending on factors like which side is facing the Sun, day/night side of the orbit and material properties of the satellite.

Earth albedo effect compensation also needs to be further investigated, the concept is discussed partly in the author's previous work [1].

The physical configuration of the acquisition of the signal from the solar cells needs to be determined. The current from the solar cells is very much dependent on resistive load, a concept which directly collides with the notion of e.g. peak power tracking. Besides scaling the signal with respect to load, a switching circuit for relieving the cells of any load is an option, but also carries risk in form of malfunction which can leave the cell in a state where it does not generate power for the satellite.

# Appendix A

# List of Symbols, Acronyms and Nomenclature

| | |
|---|---|
| **ADCS** | Attitude determination and control |
| **AM** | Air mass |
| **ARR** | Andøya Rocket Range |
| **ASTM** | American Society for Testing and Materials |
| **BOL** | Beginning-of-life |
| **COTS** | Commercial-off-the-shelf (components) |
| **CPV** | Concentrating photovoltaic |
| **CSP** | Concentrating solar photovoltaic/power |
| **CSR** | Circumsolar ratio |
| **DAQ** | Data aquisition |
| **DC** | Direct current |
| **DOF** | Degrees of freedom |
| **DNI** | Direct normal irradiance |
| **DSSC** | Dye-sensitized solar cells |
| **DUT** | Device under test |
| **EKF** | Extended Kalman filter |
| **EOL** | End-of-life |
| **EQUEST** | Extended quaternion estimator |
| **FF** | Fill factor |
| **FSM** | First/front surface mirror |
| **HID** | High intensity discharge (gas lamp) |
| **IEC** | International Engineering Consortium |
| **IR** | Infrared (electromagnetic radiation/spectrum) |
| **JIS** | Japanese Industrial Standards |
| **MH** | Metal halide |
| **MJ** | Multijunction |
| **MPP** | Maximum power point |
| **NAROM** | Norwegian Centre for Space-related Education |
| **NASDA** | National Space Development Agency of Japan |
| **NEMA** | National Electrical Manufacturers Associasion |
| **NIR** | Near-infrared (electromagnetic radiation/spectrum) |

| | |
|---|---|
| **NTNU** | Norwegian University of Science and Technology |
| **NUTS** | NTNU Test Satellite |
| **PID** | Proportional-integral-derivative (controller) |
| **PSC** | Photoelectrochemical solar cell |
| **PV** | Photovoltaic |
| **QUEST** | Quaternion estimator |
| **RDB** | Reduced data base |
| **SC** | SuperCool (temperature controller) |
| **SG** | Semiconductor grade (silicon) |
| **Si** | Silicon |
| **SMARTS** | Simple Model for the Atmospheric Radiative Transfer of Sunshine |
| **SRC** | Standard reporting conditions |
| **STC** | Standard testing conditions |
| **TFSC** | Thin film solar cell |
| **TSI** | Total solar irradiance |
| **UV** | Ultraviolet (electromagnetic radiation/spectrum) |
| **VIS** | Visible (electromagnetic radiation/spectrum) |
| **Xe** | Xenon |

| | |
|---|---|
| $\mathbf{A}$ | Area |
| $\eta$ | Efficiency |
| $\mathbf{E}$ | Irradiance |
| $\mathbf{I_{ph}}$ | Photogenerated current |
| $\mathbf{I_D}$ | Diode current |
| $\mathbf{I_L}$ | Load current, output from cell |
| $\mathbf{I_{mp}}$ | Current at maximum power point |
| $\mathbf{I_S}$ | Saturation current |
| $\mathbf{I_{sh}}$ | Shunt current |
| $\mathbf{I_{sc}}$ | Short circuit current |
| $\lambda$ | Wavelength |
| $\nu$ | Frequency |
| $\mathbf{n}$ | Idealizing factor |
| $\mathbf{P_{in}}$ | Power incident on solar cell |
| $\mathbf{P_{max}}$ | Maximum power |
| $\mathbf{R_{CH}}$ | Characteristic resistance |
| $\mathbf{R_L}$ | Load resistance |
| $\mathbf{R_s}$ | Series resistance |
| $\mathbf{R_{sh}}$ | Shunt resistance |
| $\theta$ | Sun incidence angle |
| $\mathbf{T}$ | Temperature of solar cell |
| $\mathbf{V}$ | Cell voltage |
| $\mathbf{V_{mp}}$ | Voltage at maximum power point |
| $\mathbf{V_{oc}}$ | Open circuit voltage |

| | |
|---|---|
| $\mathbf{c}$ | Speed of light (in vacuum), $c = 2.9979 \times 10^8$ m·s$^{-1}$ |
| $\mathbf{e}$ | Earth orbit eccentricity, $e = 0.01671123$ |
| $\mathbf{h}$ | Planck's constant, $h = 6.62606957 \times 10^{-34}$ J·s |
| $\mathbf{k_B}$ | Boltzmann's constant, $k_B = 1.3806488 \times 10^{-23}$ J·K$^{-1}$ |
| $\mathbf{q}$ | Elementary electric charge, $q = 1.602176565 \times 10^{-19}$ C |
| $\mathbf{r_{sun}}$ | Sun radius, $r_{sun} = 6.963 \times 10^8$ m |
| $\sigma$ | Stefan-Boltzmann's constant, $\sigma = 5.670373 \times 10^{-8}$ W·m$^{-2}$·K$^{-4}$ |
| $\mathbf{T_{sun}}$ | Sun surface temperature, $T_{sun} = 5778$ K |

# Appendix B

## Azurspace 3G30C Solar Cell Data Table

Table B.1: Azurspace 3G30C solar cell data sheet. [127]

| Design and mechanical data | |
| --- | --- |
| Base material | GaInP/GaAs/Ge on Ge substrate |
| AR-coating | $TiO_x/Al_2O_3$ |
| Dimensions | 40 x 80 mm $\pm$ 0.1 mm |
| Cell area | 30.18 cm$^2$ |
| Average weight | $\leq$ 86 mg/cm$^2$ |
| Thickness | 150 $\pm$ 20 $\mu$m |
| Contact metallization thickness (Ag/Au) | 4 - 10 $\mu$m |
| Grid design | Grid system with 3 contact pads |
| Integrated protection diode | $V_{forward}$(605 mA) $\leq$ 2.5 V |
| | $I_{reverse}$(2.8 V) $\leq$ 100 $\mu$A @ T = 25 $^\circ$C |

| Electrical data | | | BOL | 5E14 | 1E15 | 3E15 |
| --- | --- | --- | --- | --- | --- | --- |
| Average open circuit voltage | $V_{oc}$ | (mV) | 2669 | 0.94 | 0.92 | 0.89 |
| Average short circuit current | $I_{sc}$ | (mA) | 525 | 0.99 | 0.96 | 0.87 |
| Voltage at maximum power | $V_{mp}$ | (mV) | 2379 | 0.93 | 0.91 | 0.88 |
| Current at maximum power | $I_{mp}$ | (mA) | 505 | 0.98 | 0.95 | 0.86 |
| Average efficiency | $\eta_{bare}$ | (%) | 29.1 | 0.91 | 0.87 | 0.76 |

| Acceptance values | | |
| --- | --- | --- |
| Voltage | $V_{op}$ | 2300 mV |
| Minimum average current @ $V_{op}$ | $I_{op\ avg}$ | 510 mA |
| Minimum individual current @ $V_{op}$ | $I_{op\ min}$ | 475 mA |

*Standard: CASOLBA 2005 (05-20MV1, etc); Cell Type: 3G-28%;*
*Spectrum: AM0 WRC (1367 W/$m^2$); T = 28$^\circ$C*

| Temperature gradients | | | BOL | 5E14 | 1E15 |
| --- | --- | --- | --- | --- | --- |
| Open circuit voltage | $dV_{oc}/dT$ | (mV/$^\circ$C) | -6.0 | -6.2 | -6.3 |
| Short circuit current | $dI_{sc}/dT$ | (mA/$^\circ$C) | 0.32 | 0.31 | 0.39 |
| Voltage at maximum power | $dV_{mp}/dT$ | (mV/$^\circ$C) | -6.1 | -6.3 | -6.4 |
| Current at maximum power | $dI_{mp}/dT$ | (mA/$^\circ$C) | 0.28 | 0.20 | 0.29 |

| Threshold values | |
| --- | --- |
| Absorptivity | $\leq$ 0.91 (with CMX 100 AR) |
| Pull test | > 1.6 N at 45$^\circ$ welding test (with 12.5 $\mu$m Ag stripes) |
| Development status | Qualified |

# Appendix C

# Optical Calibration Lab: IV Measurement Procedure

**Preparation**

- Turn on the solar simulator cooling fan power, switch on the back, right side of the solar simulator.

- Turn on the solar simulator lamp, switch on the left side of simulator to ON position. Wait for about 15 minutes for lamp to be stable.

- Turn on the computer.

- Turn on the source meter.

- Turn on the power of the temperature controller.

**Lamp Calibration**

- Place the calibration reference cell onto the work plane under the lamp, and connect the wires to a voltmeter.

- Open the lamp shutter on the left side of the simulator.

- Measure the reference cell voltage, it should read 87.3 mV which corresponds to a light intensity of 100 mW/cm$^2$, or 1 Sun.

- If the measured voltage is not close to 87.3 mV, use the dial on the left side of the simulator to tune the lamp current accordingly.

## Measurement

- Make sure that the probe cables are connected to the meter.

- Place the device on the copper plate and carefully move the two probes to the cell (p-side to +, n-side to -).

- Open the program for temperature controller; "Shortcut to IC_Interface.exe".

  - Load the file "PVlab.sc", which gives 25 °C setpoint.

  - Click on the "Connect Rs232" button and then on the "send" button to initiate the temperature control.

  - Open the lamp shutter on the left side of the simulator, and wait for the temperature to stabilize at 25 °C.

- Open the program for the measurement: "Solarlab.exe".

- You can do a quick $I_{sc}$ and $V_{oc}$ measurement by clicking "quick measurement".

- Set the starting V, end V, increasement and dwell-time for the I-V measurement.

- When the temperature is stable at 25 °C, you can start the measurement.

- The data will be saved as .lvm files which can be opened in Excel.

## After measurement

- Turn off the lamp power, and wait at least 15 minutes before turning off the fan.

- Close the programs of measurement and temperature controller.

- Turn off the computer.

- Turn off the source meter.

- Turn off the power of the temperature controller.

- Fill in the log sheet.

## Warnings

- Never turn off the fan before turning off the lamp power and waiting for 15 minutes.

- Be careful with the tips of the probes when placing the probes on the samples, so as to not damage the tips of the probes.

# Bibliography

[1] M. Nygren, R. Birkeland, and J.T. Gravdahl. Using solar panels as sun sensors on ntnu test satellite. Specialization project, Norwegian University of Science and Technology, 2013.

[2] M. Nygren, R. Birkeland, and J.T. Gravdahl. Using independent combinations of cubesat solar panels as sun sensors for separating inbound sunlight information. In *Proceedings of the 2nd IAA Conference On University Satellite Missions And Cubesat Workshop*, pages 661–675, 2013.

[3] Marianne Bakken. Signal processing for communicating gravity wave images from the ntnu test satellite. Master's thesis, Norwegian University of Science and Technology, 2012.

[4] Cubesat design specification, 2009.

[5] K.I.M. Rokstad. Utvikling av komposittramme for satellitt. Master's thesis, Norwegian University for Science and Technology, 2012.

[6] F. Alvenes. Attitude controller-observer design for the ntnu test satellite. Master's thesis, NTNU, 2013.

[7] G. Brathen. Design of attitude control system of a double cubesat. Master's thesis, NTNU, 2013.

[8] P.K. Soglo. 3-aksestyring av gravitasjonsstabilisert satellitt ved bruk av magnetspoler. Master's thesis, NTH, 1994.

[9] R. Wisniewski. *Satellite Attitude Control Using Only Electromagnetic Actuation.* PhD thesis, Aalborg University, 1996.

[10] E.J. Overby. Attitude control for the norwegian student satellite nCube. Master's thesis, NTNU, 2004.

[11] E.J. Overby, J.T. Gravdahl, S.S. Ose, and K.M. Fauske. nCube - norwegian student satellite: Attitude determination and control system. In *Space Technology Education Conference*, 2004.

[12] K. Svartveit. Attitude determination of the ncube satellite. Master's thesis, NTNU, 2003.

[13] J.T. Gravdahl, E. Eide, A. Skavhaug, K. Svartveit, K.M. Fauske, and F.M. Indergaard. Three axis attitude determination and control system for a picosatellite: Design and implementation. In *Proceedings of the 54th International Astronautical Congress*, 2003.

[14] S.S. Ose. Attitude determination for the norwegian student satellite ncube. Master's thesis, NTNU, 2004.

[15] J. Rohde. Kalman filter for attitude determination of student satellite. Master's thesis, NTNU, 2007.

[16] Z. Tudor. Design and implementation of attitude control for 3-axes magnetic coil stabilization of a spacecraft. Master's thesis, NTNU, 2011.

[17] M.D. Shuster and S.D. Oh. Three-axis attitude determination from vector observations. *Journal of Guidance and Control*, 4(1):70–77, 1981.

[18] K.L. Jenssen and K.H. Yabar. Development, implementation and testing of two attitude estimation methods for cube satellites. Master's thesis, NTNU, 2011.

[19] K.L. Jenssen, K.H. Yabar, and J.T. Gravdahl. A comparison of attitude determination methods: theory and experiments. In *Proceedings of the 62nd International Astronautical Congress*, 2011.

[20] M.L. Psiaki. Attitude-determination filtering via extended quaternion estimation. *Journal of Guidance, Control, and Dynamics*, 23(2):206–214, Mar.-Apr 2000.

[21] F.L. Markley and D. Mortari. Quaternion attitude estimation using vector observations. *The Journal of the Astronautical Sciences*, 48(2-3):359–380, Apr.-Sep. 2000.

[22] T.B. Rinnan. Development and comparison of estimation methods for attitude determination. Master's thesis, NTNU, 2012.

[23] T.B. Rinnan, R. Birkeland, and J.T. Gravdahl. Development on the equest method for attitude determination. In *Fourth European CubeSat Symposium*, 2012.

[24] Fredrik Sola Holberg. Design of attitude estimation and control system for a cube satellite. Master's thesis, NTNU, 2012.

[25] F.S. Holberg, R. Birkeland, and J.T. Gravdahl. Implementation of three axis attitude determination and control system for a double cubesat. In *Fourth European CubeSat Symposium*, 2012.

[26] *Newport, Oriel Product Training - Spectral Irradiance*, .

[27] *ISO 21348 Definitions of Solar Irradiance Spectral Categories.*

[28] J.E. Parrott. Choice of an equivalent black body solar temperature. *Solar Energy*, 51(3): 195, 1993.

[29] Sun fact sheet. NASA. Accessed Feb 17 2014. <http://nssdc.gsfc.nasa.gov/planetary/factsheet/sunfact.html>.

[30] M. Emilio, J.R. Kuhn, R.I. Bush, and I.F. Scholl. Measuring the solar radius from space during the 2003 and 2006 mercury transits. *The Astrophysical Journal*, 750(2):135, 2012.

[31] A. Luque and S. Hegedus, editors. *Handbook of Photovoltaic Science and Engineering.* John Wiley and Sons, 2nd edition, 2011.

[32] *ASTM E 490 Solar Constant and Zero Air Mass Solar Spectral Irradiance*, .

[33] *ASTM G 173 Reference Spectral Solar Irradiance*, .

[34] G. Kopp and J.L. Lean. A new, lower value of total solar irradiance: Evidenc and climate significance. *Geophysical Research Letters*, 38, 2011.

[35] G.D. Rai. *Solar Energy Utilization.* Khanna Publishers, 1980.

[36] E. Standish, E. Myles, and J.C. Williams. Orbital ephemerides of the sun, moon and planets. *International Astronomical Union Commission 4: (Ephemerides)*.

[37] M.A. Green. *Solar Cells: Operating Principles, Technology and System Applications.* Prentice-Hall, 1982.

[38] *IEC 60904-3 Photovoltaic devices - Part 3 Measurement principles for terrestrial photovoltaic (PV) solar devices with reference spectral irradiance data,* .

[39] C.A. Gueymard, D. Myers, and K. Emery. Proposed reference irradiance spectra for solar energy systems testing. *Solar Energy*, 73(6):443–467, 2002.

[40] SMARTS: The Simple Model of the Atmospheric Radiative Transfer of Sunshine. NREL (National Renewable Energy Laboratory). Accessed 19 Feb 2014. <http://www.nrel.gov/rredc/smarts/>.

[41] Q. Fu. *Radiation (Solar).* Elsevier, 2003.

[42] L.G.M. Oliveira, D.G. Faria, V.E.B.M. Pereira, S.F. Domingos, F.S. de Oliveira, G.L.P. Rabelo, E.G. Arreguy, L. de Vilhena Brandao, R. Schirm, and E.M.D. Pereira. Automation of a cartesian positioner for tracking a pyranometer during evaluation test of the emitted irradiance uniformity by a continuous solar simulator. *ABCM Symposium Series in Mechatronics*, 3: 813–820, 2008.

[43] Spectral Calculator. Online data/graph tool, Gats Inc. Accessed 19 Feb 2014. <http://www.spectralcalc.com/spectral_browser/>.

[44] L.L. Gordley, B.T Marshall, and A.D. Chu. LINEPAK: Algorithms for modeling spectral transmittance and radiance. *Journal of Quantitative Spectroscopy & Radiative Transfer*, 52 (5):563–580, 1994.

[45] L.S. Rothman. The HITRAN 2008 molecular spectroscopic database. *Journal of Quantitative Spectroscopy & Radiative Transfer*, 110:533–572, 2009.

[46] A. Neumann, A. Witzke, J.A. Scott, and S. Gregor. Representative terrestrial solar brightness profiles. *Journal of Solar Energy Engineering*, 124:198–204, 2002.

[47] D.C. Buie. *Optical considerations in solar concentrating systems*. PhD thesis, University of Sydney, 2004.

[48] The Lawrence Berkeley Laboratory Reduced Data Base (RDB). Lawrence Berkeley Laboratory. Accessed 19 Feb 2014. <http://rredc.nrel.gov/solar/old_data/circumsolar/>.

[49] R. Kalapatapu. Measurement and analysis of solar radiation angular distribution with sunshape profiling irradiometer. Master's thesis, Masdar Institute of Science and Technology, 2012.

[50] S. Wilbert, R. Pitz-Paal, and J. Jaus. Circumsolar radiation and beam irradiance measurements for focusing collectors. In *ES1002: Cost Wire Workshop May 22nd-23rd*, 2012.

[51] D. Chiras. *Power From the Sun: A Practical Guide to Solar Electricity*. New Society Publishers, 2009.

[52] A. McEvoy, T. Markvart, and L. Castaner, editors. *Practical Handbook of Photovoltaics - Fundamentals and Applications*. Elsevier, 2nd edition, 2012.

[53] M. Green. *Third Generation Photovoltaics*. Springer, 2003.

[54] P. Rahmanpour, J.A. Bones, M. Hovd, and J.T. Gravdahl. Linear and nonlinear state estimation in the czochralski process. In *10th IFAC International Symposium on Dynamics and Control of Process Systems*, 2013.

[55] W. Shockley and H. Queisser. Detailed balance limit of efficiency of p-n junction solar cells. *Journal of Applied Physics*, 32:510–519, 1961.

[56] A. De Vos. Detailed balance limit of the efficiency of tandem solar cells. *Journal of Physics D - Applied Physics*, 13(5):839–846, 1980.

[57] A. Marti and Luque A., editors. *Next Generation Photovoltaics - High Efficiency Through Full Spectrum Utilization*. Institute of Physics Publishing, 2004.

[58] A. Luque and A. Marti. Increasing the efficiency of ideal solar cells by photon induced transitions at intermediate levels. *Physical Review Letters*, 78:5014–5017, 1997.

[59] S. Kolodinski, J.H. Werner, T. Wittchen, and H.J. Queisser. Quantum efficiencies exceeding unity due to impact ionization in silicon solar cells. *Applied Physics Letters*, 63:2405–2407, 1993.

[60] R.T. Ross and A.J. Nozik. Efficiency of hot-carrier solar energy converters. *Journal of Applied Physics*, 53:3813–3818, 1982.

[61] M. Gratzel. Conversion of sunlight to electric power by nanocrystalline dye-sensitized solar cells. *Journal of Photochemistry and Photobiology A - Chemistry*, 164:3–14, 2004.

[62] S. Sun. *Organic and Polymeric Solar Cells*, volume 3. American Scientific Publishers, 2008.

[63] C.H. Henry. Limiting efficiencies of ideal single and multiple energy gap terrestrial solar cells. *Journal of Applied Physics*, 51:4494–4500, 1980.

[64] A. Marti and G.L. Araujo. Limiting efficiencies for photovoltaic energy conversion in multigap systems. *Solar Energy Materials and Solar Cells*, 43(2):203–222, 1996.

[65] C.D. Dominguez. *Caracterizacion Optica y Electrica de Sistemas Fotovoltaicos de Alta Concentracion.* PhD thesis, Universidad Politecnica de Madrid, 2012.

[66] *Application Note PVA-600-1 Guide to Interpreting I-V Curve Measurements of PV Arrays.* Solmetric, March 2011.

[67] H. Cotal, C. Fetzer, J. Boisvert, G. Kinsey, R. King, P. Hebert, H. Yoon, and N. Karam. Iii-v multijunction solar cells for concentrating photovoltaics. *Energy & Environmental Science*, 2:174–192, 2009.

[68] M.A. Green. Accuracy of analytical expressions for solar cell fill factors. *Solar Cells*, 7: 337–340, 1982.

[69] *Electrical Characterization of Photovoltaic Materials and Solar Cells with the Model 4200-SCS Semiconductor Characterization System.* Keithley.

[70] D.L. King, J.A. Kratochil, and W.E. Boyson. Temperature coefficients for pv modules and arrays: measurement methods, difficulties, and results. In *26th IEEE Photovoltaics Specialists Conference*, 1997.

[71] H. Cotal and R. Sherif. Temperature dependence of the iv parameters from triple junction gainp/ingaas/ge concentrator solar cells. In *Conference Record of the 2006 IEEE 4th World Conference on Photovoltaic Energy Conversion*, volume 1, pages 845–848, 2006.

[72] K. Emery, M. Meusel, R. Beckert, F. Dimroth, A. Bett, and W. Warta. Procedures for evaluating multijunction concentrators. In *Proceedings of the 28th IEEE Photovoltaic Specialists Conference*, 2000.

[73] W. Herrmann and L. Rimmelspacher. Uncertainty of solar simulator spectral irradiance data and problems with spectral match classification. In *27th European Photovoltaic Solar Energy Conference and Exhibition*, pages 3015–3021, 2012.

[74] Carl Zeiss Microscopy and Digital Imaging Online Campus website. Digital education campus, Carl Zeiss. Accessed 05 Feb 2014. <http://zeiss-campus.magnet.fsu.edu/>.

[75] *Lighting Fundamentals, Lighting Upgrade Manual, US EPA Green Lights Program.*

[76] *Illuminating Engineering Society, Lighting Measurements - A basic approach to understanding the principals of Lighting Science.*

[77] M.G. Guvench, C. Gurcan, K. Durgin, and D. MacDonald. Solar simulator and i-v measurement system for large area solar cell testing. In *Proceedings of the 2004 American Society for Engineering Education Annual Conference & Exposition*, 2004.

[78] J. Petrasch, P. Coray, A. Meier, M. Brack, P. Haberling, D. Wuillemin, and A. Steinfeld. A novel 50 kw 11,000 suns high-flux solar simulator based on an array of xenon arc lamps. *Journal of Solar Energy Engineering*, 129:405, 2007.

[79] D.S. Codd, A. Carlson, J. Rees, and A.H. Slocum. A low cost high flux solar simulator. *Solar Energy*, 84(12):2202–2212, 2010.

[80] Philips XDC-6500B Xenon Projector Lamp. Digital image, Theatrical Bulb Supply. Accessed 05 Feb 2014. <http://www.theatricalbulbsupply.com/xenon-short-arc-lamps/barco/barco-r9856380-xenon-projector-lamp/>.

[81] *Xenon Lamp Listing - High performance short arc xenon lamp solutions.* Christie Digital Systems Inc., 2008.

[82] X. Dong, P.J. Ashman, and G.J. Nathan. A high-flux solar simulator system for investigating the influence of concentrated solar radiation on turbulent reacting flows. In *Proceedings of the 50th Annual Conference, Australian Solar Energy Society*, 2012.

[83] Precision Lighting 991327 MH Lamp. Digital image, 1000Bulbs. Accessed 05 Feb 2014. <http://www.1000bulbs.com/product/60052/PLT-991327.html>.

[84] Metal halide lamp components. Digital image, New Power Tech. Accessed 05 Feb 2014. <http://www.indiamart.com/newpowertech/lamp-fittings.html>.

[85] Halogen Lightbulbs. Digital image, Lamps Plus Inc. Accessed 05 Feb 2014. <http://www.lampsplus.com/info-center/b/advice-and-tips/archive/2010/02/08/how-a-halogen-light-bulb-works.aspx>.

[86] Tungsten-Halogen Lamp Anatomy. Digital image, Carl Zeiss. Accessed 05 Feb 2014. <http://zeiss-campus.magnet.fsu.edu/articles/lightsources/tungstenhalogen.html>.

[87] R. Paschotta. *Encyclopedia of Laser Physics and Technology*. Wiley-VCH, 2008.

[88] Light Emitting Diodes Illustration. Digital image, LED Today. Accessed 05 Feb 2014. <http://ledtoday.com/tenfacts.htm>.

[89] Light Emitting Diode Schematic. Digital image, Bright Hub Inc. <http://www.brighthubengineering.com/robotics/60933-how-to-test-led-lamps/>.

[90] *The Radiometry of Light Emitting Diodes, Labsphere.*

[91] Ecosun 10L - AAA LED Solar Simulator. Ecoprogetti. Accessed 05 Feb 2014. <http://www.ecoprogetti.com/en/products/module-testing/ecosun-10l.html>.

[92] Mercury Short Arc Lamp (8000W). Digital image, copyleft. Accessed 05 Feb 2014. <http://lampes-et-tubes.info/alhg/al061.php>.

[93] *DC Short Arc Lamps Catalog.* Oriel Instruments, .

[94] Illuminating Engineering Society of North America (IES). *The IESNA Lighting Handbook.* Illuminating Engineering, 2000.

[95] P. Baillon, A. Braem, G. Gendre, G. Muratori, and C. Nichols. An improved method for manufacturing accurate and cheap glass parabolic mirrors. *Nuclear Instruments and Methods in Physics Research Section A - Accelerators, Spectrometers, Detectors and Associated Equipment*, 276:492–495, 1989.

[96] D. Dimitrakis, C. Lekkos, I. Dolios, and A.G. Konstandopoulos. Design and construction of a 66 kw solar simulator facility. In *9th Panhellenic Scientific Chemical Engineering Congress*, 2003.

[97] J. Benya. *Advanced Lighting Guidelines.* New Buildings Insititute, 2003.

[98] *CVI Melles Griot Technical Guide - Optical Coatings.*

[99] H.A. Macleod. *Thin-Film Optical Filters.* CRC Press, 2010.

[100] A. Malul, D. Nakar, D. Feuermann, and J.M. Gordon. Effectiveness of recycling light in ultra-bright short-arc discharge lamps. *Optics Express*, 15(21), 2007.

[101] I. Alxneit and G. Dibowski. Project SFERA r12.5 solar simulator evaluation report. Technical report, Solar Facilities for the European Research Area, 2011.

[102] F. Clarysse and M. Vermeulen. Characterizing the surface waviness of steel sheet: reducing the assessment length by robust filtering. *Wear*, 257(12):1219–1225, 2004.

[103] P.S. Carlin. Lightweight mirror systems for spacecraft - an overview of materials and manufacturing needs. In *2000 IEEE Aerospace Conference Proceedings*, volume 4, 2000.

[104] *NEMA Standards FA 1-1973 - Outdoor Floodlighting Equipment.*

[105] *ANSI C78.379-2006 - Classification of the Beam Patterns of Reflector Lamps.*

[106] OptiCAD Optical Analysis Software. Software, OptiCAD Corp. Accessed 19 Feb 2014. <http://www.opticad.com/>.

[107] H. Price, E. Lupfert, D. Kearney, E. Zarza, G. Cohen, R. Mahoney, and R. Gee. Advances in parabolic trough solar power technology. *Journal of Solar Energy Engineering*, 124(2): 109–125, 2002.

[108] A. Fernandez-Garcia, E. Zarza, L. Valenzuela, and M. Perez. Parabolic-trough solar collectors and their applications. *Renewable and Sustainable Energy Reviews*, 14(7):1695–1721, 2010.

[109] M.K. Chawla. A step by step guide to selecting the right solar simulator for your solar cell testing application. Technical report, Photo Emission Tech Inc, 2011.

[110] *ASTM E 927 Standard Specification for Solar Simulation for Terrestrial Photovoltaic Testing*, .

[111] P. Grantek and T. Zdanowicz. Advanced system for calibration and characterization of solar cells. *Opto-Electronics Review*, 12(1):57–67, 2004.

[112] Photon International. Market survey on cell testers and sorters. *The Photovoltaic Magazine*, 10:48–57, 2002.

[113] G. Overton. Photonics applied: Photovoltaics: Not all solar simulators are created equal. *Laser Focus World*, 2011.

[114] D.L. King. Measurement precautions for high-resistivity silicon solar cells. In *Conference Record of the Twentieth IEEE Photovoltaic Specialists Conference*, volume 1, pages 555–559, 1988.

[115] W. Keogh and A. Blakers. Natural sunlight calibration of silicon solar cells. In *17th European Photovoltaic Solar Energy Conference*, 2001.

[116] K. Emery, D. Myers, and S. Rummel. Solar simulation - problems and solutions. In *20th IEEE PV Specialists Conference*, page 1087, 1988.

[117] *IEC 60904-9 Photovoltaic devices - Part 9  Solar simulator performance requirements*, .

[118] *JIS C 8912 Solar simulators for crystalline solar cells and modules.*

[119] *ABET Sun 2000 Solar Simulators Family Product Specification.* ABET Technologies, 2007.

[120] *Omron Model H5CX-ASD-AC24/DC12-24 Digital Timer Product Manual.* OMRON Industral Automation, 2008.

[121] *ABET Manual - Solar Simulators and Uniform Exposure Systems.* ABET Technologies, 2008.

[122] *PR-59, TC-XX-PR-59 Temperature Controller Documentation.* Laird Tecnologies.

[123] Rera Solutions silicon refererence cell. Electronic document, Rera Solutions. Accessed 05 Feb 2014. <http://www.rera.nl/index.php/specifications-silicon-reference-cell/>.

[124] O. Kawasaki, S. Matsuda, Y. Yamamoto, Y. Kiyota, and Y. Uchida. Study of solar simulator calibration method and round robin calibration plan of primary standard solar cell for space use. In *Proceedings of the 1st World Conference on Photovoltaic Energy Conversion*, volume 2, 1994.

[125] *Qioptiq Solar Cell Coverglasses Product Manual*, 2010.

[126] R.K. Mathur, D.R. Mehrotra, S. Mittal, and S.R. Dhariwal. Thermal non-uniformities in concentrator solar cells. *Solar Cells*, 11(2):175–188, 1984.

[127] *3G30C, 30% Triple Junction GaAs Solar Cell data sheet.* Azurspace, 2009.